DESIGN AND SIMULATIONS OF A BERYLLIUM BASED NEUTRON PRODUCTION BEAMLINE AT METU DBL

A THESIS SUBMITTED TO
THE GRADUATE SCHOOL OF NATURAL AND APPLIED SCIENCES
OF
MIDDLE EAST TECHNICAL UNIVERSITY

BY

EGEMEN GÖVER

IN PARTIAL FULFILLMENT OF THE REQUIREMENTS
FOR
THE DEGREE OF MASTER OF SCIENCE
IN
PHYSICS

JULY 2025

Approval of the thesis:

DESIGN AND SIMULATIONS OF A BERYLLIUM BASED NEUTRON PRODUCTION BEAMLINE AT METU DBL

submitted by **EGEMEN GÖVER** in partial fulfillment of the requirements for the degree of **Master of Science in Physics Department, Middle East Technical University** by,

Prof. Dr. Naci Emre ALTUN
Dean, Graduate School of **Natural and Applied Sciences** _____

Prof. Dr. Seçkin Kürkçüoğlu
Head of Department, **Physics** _____

Prof. Dr. Melahat Bilge Demirköz
Supervisor, **Physics, Middle East Technical University** _____

Dr. Doğa Veske
Co-supervisor, **Physics, Middle East Technical University** _____

Examining Committee Members:

Prof. Dr. Osman Yılmaz
Physics, Middle East Technical University _____

Prof. Dr. Melahat Bilge Demirköz
Physics, Middle East Technical University _____

Prof. Dr. Haluk Yücel
Medical Physics, Ankara University Institute of Nuclear Sciences _____

Date: 31.07.2025

I hereby declare that all information in this document has been obtained and presented in accordance with academic rules and ethical conduct. I also declare that, as required by these rules and conduct, I have fully cited and referenced all material and results that are not original to this work.

Name, Surname: Egemen Göver

Signature :

ABSTRACT

DESIGN AND SIMULATIONS OF A BERYLLIUM BASED NEUTRON PRODUCTION BEAMLINE AT METU DBL

Göver, Egemen
M.S., Department of Physics
Supervisor: Prof. Dr. Melahat Bilge Demirköz
Co-Supervisor: Dr. Doğa Veske

July 2025, 106 pages

There are various sources of neutron irradiation for different neutron beam applications, each with their own limitations. Limited access to nuclear reactors, the need to adjust the flux and energy of neutrons, shielding requirements and high costs of laboratory neutron source $^{252}\mathrm{Cf}$, which has an average neutron kinetic energy of 2.1 MeV that limits its applicability for high energy neutron applications, have led researches to study and adapt accelerator based neutron sources. An ideal source should have an adjustable flux and energy spectrum. One key channel is the $^{9}\mathrm{Be}(p,n)^{9}\mathrm{B}$. By utilizing the METU Defocusing Beam-Line which uses proton cyclotron at TENMAK-NUKEN Proton Accelerator Facility, a beryllium based neutron irradiation station is proposed. This study focuses on design and simulations of a solid target system with optimal parameters such that highest neutron yield with lowest production rate of residual impurity and lowest activity can be achieved during its operation. Using Monte Carlo simulation toolkits such as FLUKA, Geant4, SRIM/TRIM and deterministic nuclear reaction modelling code TALYS, anticipated outcome of the proposed experiment has been extensively studied and are reported here. This thesis

reports that by utilizing a 30 MeV, 150 μA proton beam, a beryllium based target setup stationed on METU-DBL can supply neutrons with energy spectrum starting from the epithermal (which can be further decreased to thermal using a moderator), extending to fast and ultra-fast range with a total integrated neutron flux of up to 3×10^{10} n/cm^2/s at a point on the outer surface of the target station.

Keywords: beryllium target, neutron source, accelerator based neutron source, Monte Carlo simulations, neutron irradiation

ÖZ

METU DBL ÜZERİNDE BERİLYUM TEMELLİ NÖTRON ÜRETİM IŞIN HATTININ TASARIMI VE SİMÜLASYONLARI

Göver, Egemen
Yüksek Lisans, Fizik Bölümü
Tez Yöneticisi: Prof. Dr. Melahat Bilge Demirköz
Ortak Tez Yöneticisi: Dr. Doğa Veske

Temmuz 2025 , 106 sayfa

Farklı nötron ışınlama alanları için birçok nötron kaynağı çözümü bulunmaktadır fakat bu çözümlerin her biri belirli sınırlamaları beraberinde getirir. Nükleer reaktöre ulaşımın sınırlı olduğu, değiştirilebilir nötron akısı ve enerjisi gerekliliği, 2.1 MeV ortalama nötron enerjisine sahip olan ve yüksek enerjili nötron uygulamaları için uygun olmayan $^{252}\mathrm{Cf}$ laboratuvar kaynağının yüksek maliyeti ve zırhlama gereklilikleri araştırmacıları, hızlandırıcı temelli nötron kaynaklarını araştırıp kullanmaya teşvik etmiştir. İdeal bir nötron kaynağı ayarlanabilir akı ve enerji spektrumuna sahip olmalıdır. Bu temel kanallardan $^{9}\mathrm{Be}(p,n)^{9}\mathrm{B}$ öne çıkmaktadır. TENMAK-NÜKEN'de bulunan Proton Hızlandırcı Tesisinde yer alan hızlandırıcıyı kullanan ODTÜ Saçılmalı Demet Hattı kullanılarak berilyum temelli bir nötron ışınlama istasyonu önerilmektedir. Bu çalışma, böyle bir katı hedef sisteminin operasyonel haldeyken, optimal parametreler kullanularak en yüksek nötron veriminin elde edilmesine, safsızlık ve ortamda radyoaktiviteye yol açan kalıntı çekirdeklerin en düşük miktarda üretimine odaklanmaktadır. Monte Carlo temelli FLUKA, Geant4, SRIM/TRIM ve determinis-

tik nükleer reaksiyon modelleme kodları TALYS gibi simülasyon kodları kullanılarak önerilen deneyin beklenen çıktıları kapsamlı bir şekilde çalışılmış ve bildirilmiştir. Bu tez, 30 MeV enerjiye sahip 150 μA proton akımı kullanarak METU-DBL'e kurulacak bir berilyum hedef istasyonunun ürettiği nötronların epitermal enerjilerden, hızlı ve ultra-hızlı enerji seviyelerine uzandığını, ve nötron akısının ışınlama istasyonunun yüzeyinde bir noktada 3×10^{10} n/cm^2/s seviyesine varabileceğini bildirmektedir. Bu tez aynı zamanda nötronların polietilen moderatörden geçirilerek termal enerji seviyelerine indirgenebileceğini öngörmektedir.

Anahtar Kelimeler: berilyum hedef, nötron kaynağı, hızlandırıcı temelli nötron kaynağı, Monte Carlo simülasyonları, nötron ışınlama

To my mother...

ACKNOWLEDGMENTS

I would like to express my deepest graditutes to my supervisor, Prof. Dr. Melahat Bilge Demirköz and my co-supervisor Dr. Doğa Veske for their unwavering support throughout this work. Without their patience and guidance this would not be possible.

I am thankful to my workplace Turkish Energy, Nuclear and Mining Research Institute (TENMAK) Proton Accelerator Facility (PAF) for their support.

I would also like to thank my IVMER technicians Uğur Kılıç and Bahadır Demircan for their help in the design of target station suitable for METU-DBL.

I would also like to thank my friends Atabay Mahmudov, Ben Forsyth and my cat El Gato for their sincere support.

Lastly, I would like to thank my mother for being the light in my life. She has been a constant source of strength and love.

TABLE OF CONTENTS

ABSTRACT v

ÖZ vii

ACKNOWLEDGMENTS x

TABLE OF CONTENTS xi

LIST OF TABLES xiv

LIST OF FIGURES xvi

LIST OF ABBREVIATIONS xxi

CHAPTERS

1 PREFACE 1

1.1 Research Questions and Approach 1

1.2 Structure of the Thesis 1

2 INTRODUCTION 3

2.1 Discovery of Neutrons and the Role of Beryllium 3

2.2 General Properties of Neutron 5

2.2.1 Nuclear Cross-Section 6

2.2.2 Neutron Decay 9

2.3 Neutron Applications 10

2.4 Neutron Production Methods 14

2.5 Cyclotron Based Neutron Source Solutions 15

2.6 Neutron Producing Nuclear Channels 17

3 BERYLLIUM IN NUCLEAR PHYSICS FOR NEUTRON PRODUCTION: MONTE CARLO APPROACHES AND EXPERIMENTAL BACKGROUND 21

3.1 The Beryllium Channel and The Previous Beryllium Studies for Neutron Production 21

3.2 Hydrogen Blistering Inside Target 27

3.2.1 Bragg Peak and Bethe-Bloch Formula 27

3.3 Methods of Solving Particle Transport Equations 29

3.3.1 Introduction to Monte Carlo 29

3.3.2 Random Sampling 30

3.3.3 The Rejection Technique 32

3.3.4 Phase Space and Flux Estimation 34

3.3.5 Calculation of Particle Yield Inside Target Volume 37

4 EXPERIMENTAL STATION DESIGN OF METU-NIDA AND DESCRIPTION OF COMPUTATIONAL TOOLS 41

4.1 METU Defocusing Beam-Line 41

4.2 The Beam Screen 43

4.3 GEANT4 Configuration and Code Description. 47

4.3.1 Physics 49

4.3.2 Fluence Estimation Principle of Geant4 50

4.4 FLUKA Configuration and Code Description. 51

4.4.1 Physics 52

4.4.2 Fluence Estimation Principle of FLUKA 53

4.5 TALYS Configuration and Code Description 54

5 SIMULATION RESULTS AND MECHANICAL FEASIBILITY 55

5.1 Monte-Carlo Simulations of the Setup 55

5.2 FLUKA Results 59

5.3 Geant4 Results 65

5.4 Neutron Beam Distribution Profile 72

5.5 TALYS Results 74

5.6 Residual Nuclei Production and $^{7}\mathrm{Be}$ 75

5.7 Gamma Shielding Calculations for $^{7}\mathrm{Be}$ 78

5.7.1 Half-Value and Tenth-Value Layers 80

5.8 Dose Rate Inside the Room 81

5.9 Thermal Analysis 82

5.9.1 Beryllium Material Properties 84

5.9.2 Thermal Loads and Cooling 84

5.10 Ionization and Target Damage Caused by Lattice Displacement-SRIM/TRIM Results 88

6 CONCLUSION 91

REFERENCES 93

APPENDICES 100

A APPENDIX 101

A.1 30 MeV Energy, 100μA Proton Current. 101

A.2 30 MeV Energy, 50μA Proton Current. 103

A.3 30 MeV Energy, 1μA Proton Current. 105

LIST OF TABLES

TABLES

Table 2.1 Neutron categories according to its kinetic energy 6

Table 2.2 Different types of reaction cross-sections and their notations. 8

Table 2.3 Neutron yield from radioactive α source irradiation of various targets. 15

Table 2.4 Example hydrogen accelerator based neutron–producing reactions . 17

Table 2.5 Comparison of lithium and beryllium for neutron production. 19

Table 3.1 Mandatory values for epithermal neutron beam required for BNCT, based on IAEA TECDOC (Technical Documents). 22

Table 3.2 Neutron emission characteristics for the $^{9}\mathrm{Be}(d,n)$ and $^{9}\mathrm{Be}(p,n)$ . . 26

Table 5.1 Total fluence response (particles per area per primary) due to different target tilts at a point $P(x,0,0)$ on the x-axis. 59

Table 5.2 Total neutron counts for different beryllium thicknesses (30 MeV proton, 45° target angle). 59

Table 5.3 Geant4 list of produced residual nuclei. 70

Table 5.4 Maximum isotope production rates, decay rates, activities, and yields for 30 MeV 100 μA proton beam. 75

Table 5.5 Residual nuclei activity at the end of the irradiation. 78

Table 5.6 Residual nuclei activity at the end of the cooling period of 1 hour. . . 80

Table 5.8 Mechanical properties of pure beryllium. 84

Table 5.9 Result Summary of Temperature, Heat Flux, and Thermal Gradient $150\mu A$. 86

Table A.1 Result Summary of Temperature, Heat Flux, and Thermal Gradient. $100\mu A$. 101

Table A.2 Result Summary of Temperature, Heat Flux, and Thermal Gradient. $50\mu A$. 103

Table A.3 Result Summary of Temperature, Heat Flux, and Thermal Gradient $1\mu A$. 105

LIST OF FIGURES

FIGURES

Figure 2.1 A photograph of Sir James Chadwick circa 1935. 5

Figure 2.2 Simplified diagram of both proton and neutron internal structure 6

Figure 2.3 An example diagram showing the interaction between an alpha particle and a nucleus. 7

Figure 2.4 Gadolinium-tagged turbine blade under X-Ray and Neutron radiography 12

Figure 2.5 Example diagram depicting the diffraction of neutrons. 13

Figure 2.6 Simplified diagram of ionization caused by high energy neutrons inside a semiconductor 13

Figure 2.7 Calculated flux of various induced particles resulting from the cosmic rays with respect to altitude in atmosphere. 14

Figure 2.8 Example neutron counts resulting from different masses of uranium samples, with respect to time in die-away analysis. 16

Figure 2.9 Comparison of neutron yields of (Li, Be, T, D) target materials that are irradiated with either D or ^{1}H 18

Figure 2.10 Beryllium and lithium neutron production cross-section using protons comparison 19

Figure 3.1 Low proton energy $^{9}\mathrm{Be}(p, n_0)$ reaction neutron spectrum and yield for ground state Be. 23

Figure 3.2 Neutron yield with respect to different proton energies and respective mean neutron energies. 24

Figure 3.3 Spectral flux and mean energy of neutrons resulting from p(30)+Be, given in linear plotting. p(30)+Be 25

Figure 3.4 Neutron yield and energy spectrum for p(30)+Be. 26

Figure 3.5 Illustration of hydrogen embrittlement inside beryllium. 27

Figure 3.6 The chosen points under the bounded area of normalized density function $p^*(x)$. 33

Figure 4.1 METU-DBL. 42

Figure 4.2 The METU-DBL Test Setup. 42

Figure 4.3 The planned location of the target irradiation setup, outlined in red. 43

Figure 4.4 Side view of the beam screen which is currently installed on DBL. *IVMER* 44

Figure 4.5 A 3D sketch of the beam screen which is currently installed on DBL. 45

Figure 4.6 The camera and the beam screen currently which is currently installed on METU-DBL. 46

Figure 4.7 METU-NIDA being installed. 47

Figure 4.8 Outer geometry showing moderator (green), lead casing (gray outlines) and target-beam dump duo. 48

Figure 4.9 Inner geometry showing beam dump (light blue) and target(dark blue). 48

Figure 4.10 Constructed geometry of proposed setup using FLAIR and GeoViewer. 51

Figure 4.11 A simplified top view of the irradiation room. 52

Figure 5.1 Linear energy transfer of protons with different energies inside beryllium. 56

Figure 5.2 Neutron count for proton energies between 22 MeV and 30 MeV, taken at a generic point $P(x, 0, 0)$. 56

Figure 5.3 Linear plot of spectral fluence of neutrons resulting from different proton energies. 57

Figure 5.4 Lethargy plot of low energy spectral fluence of neutrons resulting from different proton energies. 57

Figure 5.5 Azimuthal (ϕ) fluence distribution of resulting neutrons. 61

Figure 5.6 Single differential neutron fluence inside beryllium target, normalized with volume. 62

Figure 5.7 Lethargy plot of neutron fluence per primary inside beryllium target for 30 MeV proton energy. Obtained with FLUKA using USRTRACK. 63

Figure 5.8 Neutron fluence across the room given in per primary, plotted with USRBIN 63

Figure 5.9 2D plot of gamma equivalent dose during irradiation inside the room given in per primary. 64

Figure 5.10 2D plot of neutron equivalent dose during irradiation inside the room given in per primary. 64

Figure 5.11 Geant4 and FLUKA comparison of fluence and energy spectrum of neutrons resulting from 30 MeV proton beam. 65

Figure 5.12 Lethargy plot of neutron spectral fluence inside the 3 mm thick beryllium target. p(30) + Be. 66

Figure 5.13 Single-differential linear plot of neutron spectral fluence inside the beryllium target. p(30) + Be. 66

Figure 5.14 Spectral flux variations of neutrons that were produced due to 30 MeV proton beam irradiating the 3mm thick beryllium target. Before, after, and without moderation. 67

Figure 5.15 Azimuthal angular distribution of probability density function (PDF) of neutrons emerging from the beryllium target. 68

Figure 5.16 Polar angular distribution of probability density function (PDF) of neutrons emerging from the beryllium target 68

Figure 5.17 Direction of maximum neutron flow where $\theta = 70, \phi = 0$ in spherical coordinates. 69

Figure 5.18 Resulting gamma flux spectrum, y-axis in logarithmic scale . . . 71

Figure 5.19 Resulting gamma flux spectrum, y-axis in linear scale 71

Figure 5.20 Neutron Fluence Projection and Fitted 2D Gaussian Distribution at 5 cm away from the target. 72

Figure 5.21 Gaussian beam profile of neutrons given in probability distribution (PDF) across YZ plane at 5 cm away from the target. (COLZ representation). 73

Figure 5.22 Gaussian beam profile of neutrons given in probability distribution across YZ plane (LEGO representation). 73

Figure 5.23 A neutron funnel that was used by IVMER in previous studies. . 74

Figure 5.24 Comparison of experimental $^{9}\mathrm{Be}(p,x)^{7}\mathrm{Be}$ reaction cross-sections with TENDL-2012 and TENDL-2013 library between 13.4 and 70 MeV [35]. 74

Figure 5.25 Decay scheme of $^{7}\mathrm{Be}$ 76

Figure 5.26 $^{7}\mathrm{Be}$ Activity with respect to time for one half-life. 77

Figure 5.27 $^{7}\mathrm{Be}$ Activity with respect to time, up until the cooling time of 1 week. 77

Figure 5.28 Production cross-section of $^{7}\mathrm{Be}$ between 0-30 MeV. The reaction starts to take place after E_{th}:13.4 MeV. Obtained with TALYS. . . . 79

Figure 5.29 Production cross-sections of residual nuclei resulting from proton+beryllium reaction. 79

Figure 5.30 Production cross-section of tritium $^{3}\mathrm{T}$. 81

Figure 5.31 p(30) exit spectral fluence in 3 mm beryllium target. 45° target orientation. 83

Figure 5.32 Thermal analysis result of 150μA proton current, 30 MeV energy. 87

Figure 5.33 Lattice displacement per proton inside beryllium target. Obtained with SRIM. 88

Figure 5.34 Ionization given in energy per proton inside beryllium target. Obtained with SRIM. 89

Figure A.1 100μA proton current with 30 MeV kinetic energy. 102

Figure A.2 50μA proton current with 30 MeV kinetic energy. 104

Figure A.3 1μA proton current with 30 MeV kinetic energy. 106

LIST OF ABBREVIATIONS

ABBREVIATONS

BNCT	Boron Neutron Capture Therapy
ENSDF	Evaluated Nuclear Structure Data File
EXFOR	Experimental Nuclear Reaction Data
GEO	Geostationary Orbit
HVL	Half-Value Layer
IAEA	International Atomic Energy Agency
IVME-R	The Research and Application Center for Space and Accelerator Technologies
KWI	The Kaiser Wilhelm Institute for Chemistry
LEO	Low Earth Orbit
METU-DBL	Middle East Technical University Defocusing Beam-Line
METU-NIDA	Middle East Technical University Neutron Irradiation and Distribution Area
NDT	Non-Destructive Testing
NUKEN	Nuclear Energy Research Institute
PAF	Proton Accelerator Facility
RFQ	Radio-Frequency Quadrupole
SANS	Small Angle Neutron Scattering
SEU	Single Event Upset
SIRT	Selective Internal Radiation Therapy
SPECT	Single Photon Emission Computed Tomography
TENDL	TALYS Evaluated Nuclear Data Library
TENMAK	Turkish Energy Nuclear and Mining Research Agency

TVL	Tenth-Value Layer
TUBITAK	Scientific and Technological Research Council of Turkey
XRD	X-Ray Diffraction
XRF	X-Ray Fluorescence

CHAPTER 1

PREFACE

1.1 Research Questions and Approach

This study arose from the necessity of a versatile neutron source that is capable of providing neutrons of various, adjustable energies and fluxes in Türkiye. As such, some modifications to METU-DBL were proposed such that a neutron beam with adjustable flux and energy can be achieved. Irradiation of some elements with protons can induce neutron emission. One such element that can be leveraged to produce neutrons when bombarded with protons is beryllium. Due to its high neutron production cross-section in the proton energy interval of 1.85-30 MeV, compared to other cyclotron based nuclear neutron production channels relatively high neutron yields with minimal residual nuclei production may be achieved. By simulating the proposed setup with the existing facilities and foundations, optimal experimental conditions were studied to assess the feasibility of a solid, beryllium based target system to achieve a consistent and configurable neutron beam. Overall, this thesis has been written to serve as a guidance for beryllium irradiation for neutronic applications.

1.2 Structure of the Thesis

In Chapter 2, the required knowledge of general nuclear physics, introduction to neutrons, various ways of producing neutrons, working principles of Monte-Carlo simulation toolkits, and the comprehensive core concepts for proton irradiation of a beryllium target have been given. In Chapter 3, previous usages of beryllium for neutron production in nuclear physics have been presented, as well as the fundamentals of

Monte Carlo approaches and the experimental background. In Chapter 4, the existing setup of METU-DBL and the intended target station, as well as the proposed geometry, its code in simulation toolkits, physics and how the setup may proceed have been discussed. In Chapter 5, results of the simulation of the intended experiment are given. These results include the achievable neutron flux and its energy spectrum (given in both lethargy and linear plots), effects of target orientation and thickness on overall neutron yield, residual nuclei activity and their corresponding production cross-sections, dose rate inside the irradiation chamber and shielding calculations, angular distribution of neutrons and Gaussian neutron beam profile. A comprehensive investigation went into finding the optimal settings for ideal outcomes and a feasible design that can be realized in the laboratory has been proposed with this thesis.

CHAPTER 2

INTRODUCTION

The discovery of neutron by Sir James Chadwick in 1932 catalyzed a significant and rapid advancement in nuclear physics. From medicine to military, energy to material science, archaeology to particle physics, it opened many windows of opportunities for applications in different fields. This progress paced at such a remarkable speed that it took as little as twelve years from the discovery of neutrons to the detonation of the first atomic bomb.

As the periodic table expanded in the 20th century and various isotopes of different elements were discovered, physicists realized that neutrons could prove useful in many areas. They were so tightly bound with in the nucleus, in fact, the stability of nucleus of heavy elements (atomic number greater than 20) turned out to be the direct result of neutron presence in the core. Soon after the discovery of nuclear fission in December 1938, by German chemist Otto Hahn and his colleague Fritz Straßmann in Kaiser Wilhelm Institute for Chemistry, the importance and both the destructive and constructive potential of neutrons were well understood [32]. Extensive research in nuclear weapons and nuclear reactors accelerated the studies conducted on neutrons, and hence our knowledge of neutrons and their fields of use skyrocketed.

2.1 Discovery of Neutrons and the Role of Beryllium

In the 1930s, physicists were already experimenting with known radioactive sources. The alpha-emitting property of polonium was known, and physicist Walther Bothe and Herbert Becker in Physics Institute of the University of Giessen in Germany were using $^{210}\mathrm{Po}$ as a mono-energetic alpha-emitting source having 5.3 MeV to irradiate

target samples with different elemental compositions, specifically beryllium, boron, and lithium. During the irradiation of a beryllium sample with alpha particles, highly penetrating, non-ionizing radiation was detected. It was initially thought to be gamma radiation, but it was still difficult to explain the extent of penetration as it was higher than gamma photons [13]. In 1932, Irène Joliot-Curie and Frédéric Joliot further investigated this radiation. They irradiated hydrogen-rich substances such as paraffin wax with this mysterious particle. Irradiation resulted in detection of highly energetic protons, which had energies around 5 MeV [41]. Calculations showed that this type of scattering event would require the incident gamma photons to possess energies above 50 MeV, which was deemed to be difficult to achieve. Upon examining the results, James Chadwick (depicted in Figure 2.1) and Ernest Rutherford decided to show the untenable nature of the gamma ray hypothesis. Following the experiment, which was repeated using the identical reaction that Walther Bothe and Herbert Becker used:

$$^{9}\mathrm{Be} + {}^{4}\mathrm{He}\,(\alpha) \rightarrow {}^{12}\mathrm{C} + \mathrm{n}$$

Chadwick subsequently channeled the unknown radiation onto the paraffin wax, as had been done before by Irène and Frédéric Curie. He then carefully measured the travelling distance of the ejected protons. By analyzing the recoil, Chadwick concluded that the unknown particle must have a mass similar to the proton. This particle was later named neutron, and J. Chadwick was awarded a Nobel Prize in physics in 1935 for his discovery.

In the mid 1950s, reactions resulting in liberation, creation, absorption, and moderation of neutrons were being discovered expeditiously due to high investments in neutron experiments and studies conducted on developing nuclear reactors. As such, most of our knowledge of neutron induced daughter products (such as fission products), decay energies, half lives, mean lives, excited state lives etc. come from this era.

To better understand the necessity of the work being handled in this thesis, we must first reason up from the very basic properties of neutrons as the first principles method dictates and then climb up the ladder.



Figure 2.1: A photograph of Sir James Chadwick circa 1935.[24]

2.2 General Properties of Neutron

The ordinary matter we see, smell and feel are composed of subatomic particles which fall under the category of *hadrons* and *leptons*. In particle physics, a particle is considered a hadron, if it is composed of two or more *quarks* sticking to each other by the gluons, the force carrier of strong nuclear force. Quarks are the literal building blocks of matter. As of 2024, a quark is the most elementary component of hadrons. There are some theories that propose even smaller constituents that make up quarks, but so far they have not yet been experimentally verified [22]. Protons and neutrons are combination of up and down quarks. Proton is composed of two up, one down, neutron is composed of two down, one up quark. This makes them both a hadron and a baryon (composing of three quarks) [33]. A proton and a neutron are almost identical except for a small difference in mass. As a matter of fact, the liquid-drop model which was developed to describe the nucleus of the atom treats both proton and neutron the in the same way, under, where both the particles have the same spin of 1/2 [28].

In Figure 2.2 we see the individual quarks making up all the matter. Although this thesis does not study quantum chromodynamics and nuclear forces, understanding quarks carries an uttermost importance due to the fact that the decay of liberated

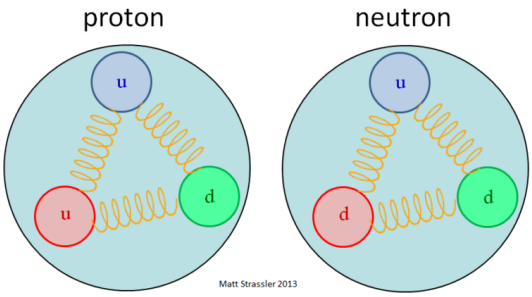


Figure 2.2: Simplified diagram of both proton and neutron internal structure. The quarks, which are shown in red green and blue, can be seen.[69]

(unbounded from nucleus) neutrons is a direct result of neutron beta decay. This decay, will, in turn, contribute to experimental background as the decay products will also generate gammas.

In nuclear physics, the neutrons are classified according to the Table 2.1.

Table 2.1: Neutron categories according to its kinetic energy. [4]

Category	**Energy Range**
Cold	Energies below 0.01 eV*
Thermal	0.01 eV to 0.3 eV*
Epithermal	0.3 eV to 10 keV*
Fast	10 keV to 20 MeV
Relativistic	> 20 MeV

* Slow neutrons

2.2.1 Nuclear Cross-Section

In nuclear physics the outcome of nuclear reactions due to collisions are not predetermined, but has many branches depending on initial parameters. The probabilistic occurrence of reactions had to be quantified to deduce the likelihood of a certain nuclear reaction. In order to parametrize this stochastic process, a novel type of definition was devised. This measure has units of barns (1 barn = 10^{-28} m^2). It can

easily be seen that it has units of area. This area is the area around the nucleus, within which the incident particles will have an interaction with the nucleus. The larger the target gets, the higher the chance of an incoming particle to hit the target and induce a nuclear reaction. However, the size of the target is not the only parameter of a cross-section. Different type of interaction between bodies yield different cross-section values. Hence, one should know the corresponding nuclear reaction mechanisms beforehand to accurately evaluate cross-section.

The vast majority of an atom is actually empty space, therefore when incident particles are bombarded onto a target material, most of them do not hard scatter. Depending on the type of the incident particle, the cross-section takes different values. That is because different particles through different force carriers. To estimate the extent of how many particles will interact and induce a reaction and how many will not, the nuclear cross-section value is used. Depending on the desired context, cross-

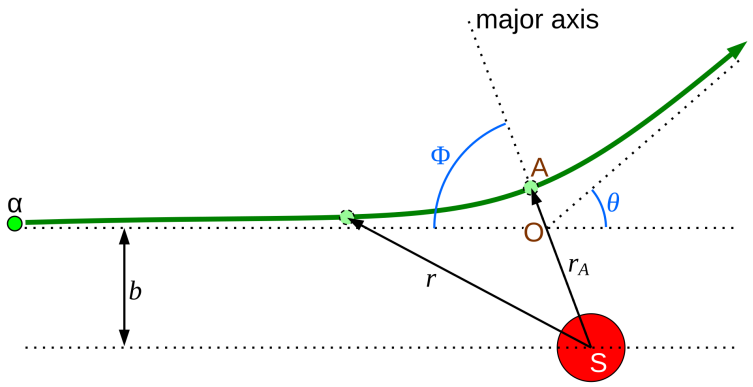


Figure 2.3: An example diagram showing the interaction between an alpha particle (green) and a nucleus (red). This is the geometry of Rutherford's scattering formula, where ϕ represents the scattering angle of the alpha particle with respect to the closest approach point (A) and θ represents the deviation of the alpha particle from the original path after scattering due to Coulomb force exerted by the target nucleus.[47]

sections may take different notations. Every notation stands for distinct information. The techniques and their possible applications are given in Table 2.2.

By the nature of interactions, cross-sections can be broken down into various categories, such as:

Table 2.2: Different types of reaction cross-sections and their notations. [45]

Cross-Section	**Symbol**	**Technique**	**Units**
Total	σ_t	Attenuation of beam	Shielding
Reaction	σ	Integration over all angles and energies of b (all excited states of Y)	Production of radioisotope Y in a nuclear reaction
Differential (Angular)	$\frac{d\sigma}{d\Omega}$	Observe b at (θ, φ) while integrating over all energies	Formation of beam of b particles in a certain direction
Differential (Energy)	$\frac{d\sigma}{dE}$	Don't observe b, but detect excitation of Y by subsequent γ-emission integrated over solid angle.	Study of decay of excited states of Y
Double Differential	$\frac{d^2\sigma}{dE_b\, d\Omega}$	Observe b at (θ, φ) at a specific energy	Information on excited states of Y via the angular distribution of b

- **Scattering Cross-sections**: Involves elastic (where no energy loss is present and hence no internal excitation) and inelastic (where there exists some energy transfer and hence there may exist some internal excitation) scattering. In Figure 2.3, a diagram depicting Rutherford scattering is given as an example. The number of particles scattered into angle θ can be given as:

$$N(\theta) = \frac{N_i n L Z^2 k^2 e^4}{4r^2 K E^2 \sin^4(\theta/2)} \tag{2.1}$$

  where N is the number of particles, L is the target thickness, Z is the atomic number of the target, n is the atoms per unit volume in target, e is the electron charge, k is the Coulombs's constant, r is the target to detector distance, KE is the kinetic energy of the projectile, and θ is the scattering angle.

- **Absorption Cross-Section**: Represents the probability of target nucleus absorbing the projectile particle. This includes all types of absorbing reactions; including radiative capture, fission, charged particle emission.

- **Fission Cross-Section**: Represents the probability of occurrence of fission after absorption. Fission can only be induced after absorption, with the exception of ^{252}Cf, which undergoes spontaneous fission due to internal quantum tunneling through the fission barrier [51].

- **Capture Cross-Section**: Similar to absorption, but capture cross-section refers to neutron capture, while absorption refers to just any reaction involving the formation of a compound nucleus.

2.2.2 Neutron Decay

When a neutron is not bound to any nucleus, it quickly transforms into a proton, electron, and an electron antineutrino [74]. Inspecting the data sheet obtained from Particle Data Group (PDG)[75], we see that the neutron has a mean lifetime of 14 minutes and 38 seconds. To model and estimate the number of neutrons in the proposed METU-NIDA (Middle East Technical University Neutron Irradiation and Distribution Area), all the neutron production channels need to be accounted for. Hence, the short amount of neutron mean life indicates the decay byproducts will also be a significant contributor in correct data acquisition.

$$n \rightarrow p^{+} + e^{-} + \bar{\nu}_{e} \tag{2.2}$$

This reaction is defined as a pure, left-handed chiral V-A interaction [29]. In another decay channel, we may also observe an extra gamma ray. This gamma is not directly coming from the excited (or isomeric) nucleus itself but rather from the internal *bremsstrahlung* radiation caused by electromagnetic interaction of emitted beta particle and proton [25].

$$n \rightarrow p^{+} + e^{-} + \bar{\nu}_{e} + \gamma \tag{2.3}$$

The probability of this channel is given as one in a thousand. So we may expect to see one gamma for every thousand neutrons. For a neutron fluence at the order of

$10^9/\text{cm}^2$, this would imply nearly a million gamma particles will contribute to our background.

2.3 Neutron Applications

It is clear that any aspect of engineering that is built on neutrons or research that either directly or indirectly requires neutrons will find itself looking for a viable and reliable neutron flux. Some areas where a neutron beam can be utilized can be given by:

- **Radio-pharmacy**: In nuclear medicine, some specific radio-nuclides serve their purpose as either diagnostic, therapeutic or both, namely called theranostic agent for cancer treatment. There are some isotopes that can only be produced when a neutron is used to bombard a target to induce a reaction. Each isotope targets a particular organ of the human body depending on which molecules they bind to and how that specific chemical structure is recognized and engaged with. For instance, Iodine-131 targets the thyroid gland because that is where the natural absorption of iodine takes place in our body. Our cells are unable to tell apart the difference between isotopes of the same element, so this property is leveraged to achieve the administration of radiopharmaceuticals. Some of these isotopes can be produced from neutron irradiation of a particular target material are: [38] [56]

    1. Molybdenum-99 (Technesium-99m $^{99\text{m}}$Tc): Most widely used diagnostic agent. Its emission of gamma rays (140 keV) is utilized.
    2. Iodine-131 (^{131}I): Used as a therapeutic radiopharmaceutical. Beta radiation from it is used to kill the cancerous tissue that is harmful.
    3. Lutetium-177 (^{177}Lu): Used as a theranostic agent, that is, it is both therapeutic due to beta emission, and diagnostic due to gamma emission that is suitable for SPECT (Single Photon Emission Computed Tomography).
    4. Yttrium-90 (^{90}Y): A therapeutic beta-emitter that is widely used in SIRT(Selective Internal Radiation Therapy)[43].
    5. Samarium-153 (^{153}Sm): A therapeutic beta-emitter that is mostly used for pain palliation in bone metastases.

6. Chromium-51 (^{51}Cr): A diagnostic agent primarily used for labeling red blood cells.
7. Iridium-192 (^{192}Ir): A therapeutic agent used in brachytherapy.
8. Xenon-133 (^{133}Xe): A diagnostic agent in gas form, mostly used for lung imaging and pulmonary function.
9. Gold-198 (^{198}Au): A therapeutic beta-emitter used for localized radiation therapy. Similar to Iridium-192, it is used in brachytherapy.
10. Phosphorus-32 (^{32}P): A therapeutic beta-emitter used in intracaviatary applications.
11. Rhenium-186 and Rhenium-188 (^{186}Re & ^{188}Re): Both are therapeutic beta-emitting agents. Their application is analogous to technetium.

- **Structural Analysis**: [73, Halban and Preiswerk (1936)] demonstrated that neutrons exhibit wave phenomena and can be diffracted by or scattered from matter. Methodologies such as neutron diffraction (ND) which is shown in Figure 2.5, small angle neutron scattering (SANS), neutron radiography, magnetic structure determination[63] and in-situ and operando measurements[6] are all achievable with a neutron source. Unlike X-Rays, which struggle to pass through dense materials, neutrons easily penetrate metals and highlight lower density materials. A particle demonstration on aerospace valves given in Figure 2.4 shows the significant difference of neutrons in comparison to X-Rays. In modern aerospace technologies, critical systems such as cryogenics and control units are expected to work flawlessly without malfunction caused by tiny defects. By using NDT (non-destructive testing) utilizing neutrons, material degradation and cracks can easily be detected during the tests. As a result, given sufficient beam flux, it is possible to have an in-depth construction of a material's spacial structure similar to XRF and XRD.

- **Nuclear Industry**: Reactor material tests: Structural integrity tests against neutron radiation, calculation of radiation resistance, analyzing the byproducts of neutron induced reactions, determining the thickness for shielding against neutrons can all be achieved by a stable neutron flux.

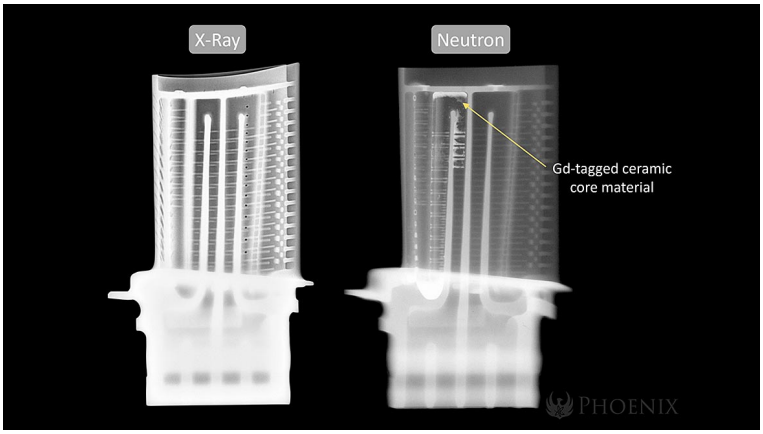


Figure 2.4: Gadolinium(due to its high reaction cross-section with neutrons)-tagged turbine blade under X-Ray and Neutron radiography. Utilizing neutrons, ceramic core can be highlighted, which is completely undetectable with X-Rays. *Source: Phoenix LLC*

- **Aviation Applications**: In some occasions, electronic components that will be subject to cosmic radiation may experience single event upsets (SEU). SEUs happen when a particle, such as a neutron, interacts with a microchip and flips a logic state. Due to high intensity of cosmic rays in the upper atmosphere, the induced secondary neutrons (increases 10-fold at $\sim$ 3 km based on studies [31, 30] and the simulation toolkit CARI-7, which plots the flux of cosmic ray induced particles in the atmosphere in Figure 2.7.) compared to ground level neutron count. neutrons may contribute significantly to SEUs. Highly energetic neutrons (typically > 1 MeV) may undergo inelastic scattering or absorption due to the presence of a neutron absorbing element inside the semiconductor devices [9]. Inelastic scattering events that result in the recoil of silicon, and nuclear reactions induced by absorption of neutrons, result in the creation of charged secondaries, ionizing their environment. This ionization is simply depicted in Figure 2.6, and it leads to creation of electron-hole pairs. Furthermore, the materials employed in spacecraft construction possess a complex and a heterogeneous elemental makeup, where this diversity is crucial to accommodate distinct functional requirements. In order to design better enduring electronic boards and eliminate the error causing events that have potential to jeopardize a mission, crucial avionics are irradiated with neutrons. Having

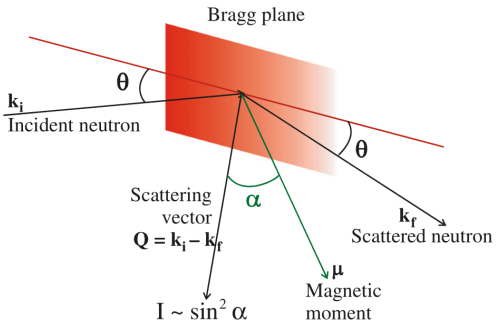


Figure 2.5: Example diagram depicting the diffraction of neutrons. Typically cold and thermal neutrons are used. By analyzing the neutron diffraction angle and vector Q, it is possible to determine the intrinsic magnetic moment.[77]

such, prior to the actual manufacturing of such craft, extensive study on neutron induced reactions is indispensable in order to prevent (or diminish the effects of) neutron related damage. Neutron irradiation tests are mandatory to ensure a smooth component operation. The neutron beam that can be achieved with the proposed setup in this thesis, is suitable for neutron radiation test standards ESCC-25100, ESCC-22500, MIL-STD-883 Test Method 1017.3, MILD-STD-750.

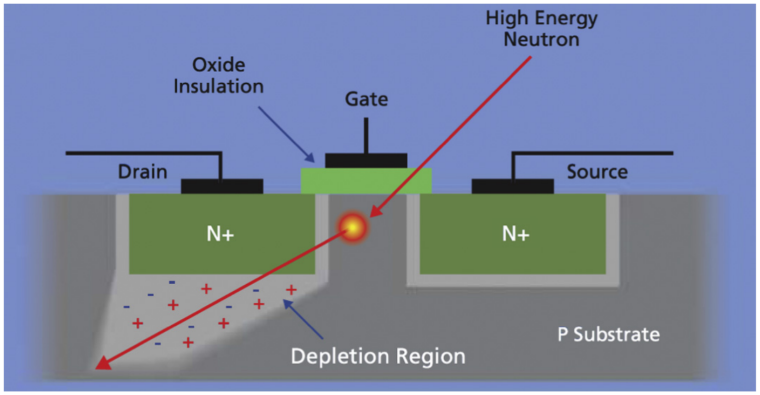


Figure 2.6: Simplified diagram of ionization caused by high energy neutrons inside a semiconductor. [18]

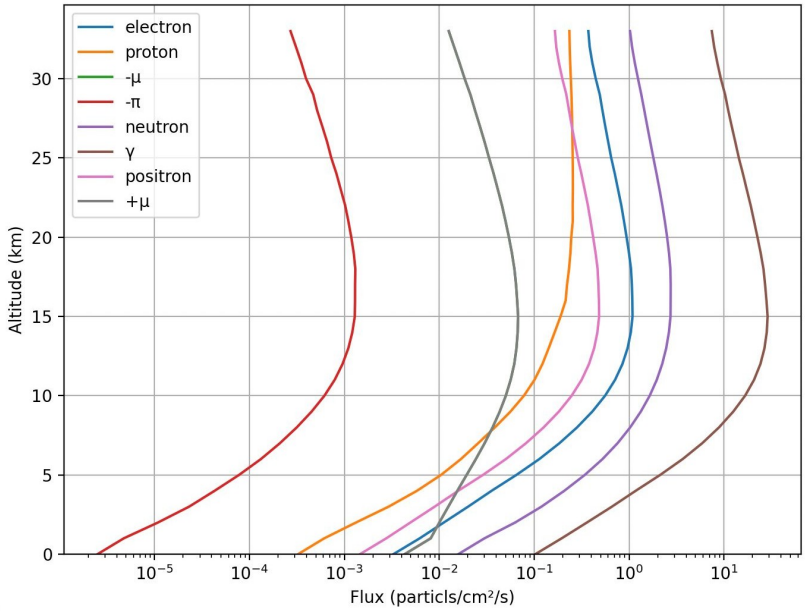


Figure 2.7: Calculated flux of various induced particles resulting from the cosmic rays with respect to altitude in atmosphere. The location was assumed to be Ankara, Kecioren. Obtained with CARI-7.

2.4 Neutron Production Methods

There are numerous methods for creating neutrons. Apart from fission reactors, the most commonly used neutron source solution are the radioisotope based channels. Alpha emitting radioisotopes are used to trigger neutron emitting reactions (α, n) [71]. This channel can generally be formulated as:

$$ {}_{Z}X^{A} + {}_{2}He^{4} \rightarrow {}_{Z+2}Y^{A+3} + {}_{0}n^{1} + Q \tag{2.4} $$

One such popular isotopic channel that fits this equation is the usage of ^{241}Am (or ^{238}Pu, ^{210}Po, ^{226}Ra) as the alpha emitter, and beryllium as the target. Various other sources are given in Table 2.3. It is seen that among other sources, americium-beryllium duo has the highest neutron yield.

Similar to alpha induced reactions, photoneutron (γ, n) sources may also be deployed. When the photon energy is greater than the Q-value of the reaction, neutron production may be induced. For instance, for a beryllium target, the photon energy needs to exceed 1.67 MeV to trigger neutron emission. The energy of the resulting neutrons at

$^{\circ}0$ (hence the plus sign, for $^{\circ}180$ it is minus) can generally be formulated as:

$$E_{\mathrm{n}} = \frac{\mathrm{A}-1}{\mathrm{A}}(\mathrm{h}\nu - |\mathrm{Q}|) \pm \sqrt{\frac{2(\mathrm{A}-1)(\mathrm{h}\nu - |\mathrm{Q}|)}{931\mathrm{A}^3}} \tag{2.5}$$

Where A is the atomic number, *h* is the Planck constant and *v* is the frequency of the photon.

As for a spontaneous neutron source, ^{252}Cf is most commonly used to obtain neutrons. This neutron emitting isotope decays by α emission with probability of 96.91% and spontaneous fission with 3.09% probability, with average kinetic energy of 2.1 MeV. It's neutron spectrum is almost identical to a reactor, and can have a maximum energy of 15 MeV which follows Watt function. Its resulting specific neutron yield is given as 2.314×10^6 s^{-1} μg^{-1} with specific activity 19.832 MBq μg^{-1} [52]. The high cost of ^{252}Cf (or any other radioisotope based solution in general) may not make it viable for choice as a source (over $27 million per gram [27]), not to mention the complicated transportation procedures and safety measures. In contrast to spontaneous fissioning ^{252}Cf or alpha-emitting radioisotope based sources.

Table 2.3: Neutron yield from radioactive α source irradiation of various targets. [61].

α-emitter	**Target**	**Reaction and Q-value**	**Neutron yield per α**
^{241}Am	^{11}B	$^{10}\mathrm{B}(\alpha, n)$, $+1.07\,\mathrm{MeV}$	1.3×10^{-5}
^{241}Am	^{18}F	$^{19}\mathrm{F}(\alpha, n)$, $-1.93\,\mathrm{MeV}$	4.1×10^{-6}
^{241}Am	^{9}Be	$^{9}\mathrm{Be}(\alpha, n)$, $+5.71\,\mathrm{MeV}$	7.0×10^{-5}
^{238}Pu	^{13}C	$^{13}\mathrm{C}(\alpha, n)$, $+2.2\,\mathrm{MeV}$	1.1×10^{-5}
^{210}Po	^{7}Li	$^{7}\mathrm{Li}(\alpha, n)$, $-2.79\,\mathrm{MeV}$	1.0×10^{-6}

2.5 Cyclotron Based Neutron Source Solutions

Cyclotrons have the advantage of supplying neutrons on demand. With the correct setup, a cyclotron based neutron source is a safer, more affordable and more modifi-

able alternative to stationary, radioisotope sources. This aspect significantly improves and simplifies safety, as well as the storage and maintenance of the source. Another advantage is that the accelerator can provide neutrons in bunches (or pulses). Similar to a nuclear reactor, neutron pulsing can allow neutron die-away analysis which is a form of non-destructive assay technique to detect the presence of fissile material inside a sample [17]. The method works by channeling wide pulses of neutrons into the sample. Due to attenuation (absorption and leakage), fast neutrons slowly disappear within a few microseconds. This time is labeled as die-away time of neutrons. If there is presence of fissile material, fission can be induced and hence new neutrons may be introduced into the system, causing a slight delay in the die-away time extending it to hundreds of microseconds even milliseconds [79]. In Figure 2.8, a demonstration with uranium samples with different masses is given. Although pulsed neutron analysis is not in the scope of this thesis, modifying the cyclotron to supply pulsed protons could also result in pulsed neutrons.

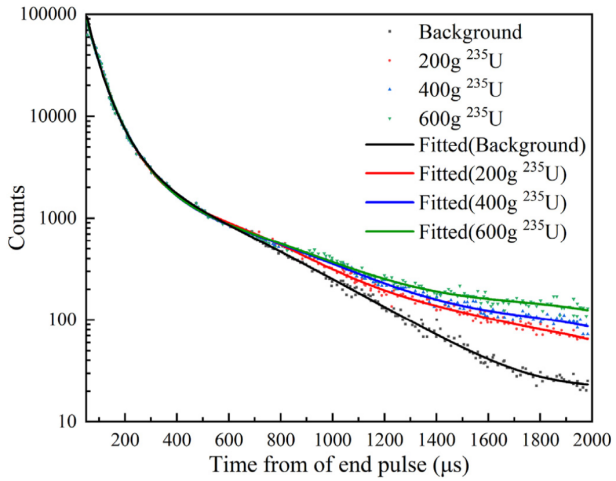


Figure 2.8: Example neutron counts resulting from different masses of uranium samples, with respect to time in die-away analysis. Higher target compositions lead to longer die-away time. [79]

2.6 Neutron Producing Nuclear Channels

In Table 2.4, some previously explored accelerator based reactions are given. The choice of target is based on both accelerator capabilities and available target irradiation chambers (in which, the target state can take one of three forms: solid, liquid or gas).

Table 2.4: Example hydrogen accelerator based neutron–producing reactions. Their threshold energy, Q values and minimum product energies are given.[17]

Shorthand	**Q Value [MeV]**	**Threshold Energy [MeV]**	**Minimum Product Energies [MeV]**
$^{2}\mathrm{H}(d,n)^{3}\mathrm{He}$	$+3.269$	Exothermic	^{3}He: 0.82; n: 2.45
$^{3}\mathrm{H}(d,n)^{4}\mathrm{He}$	$+17.589$	Exothermic	^{4}He: 3.54; n: 14.05
$^{7}\mathrm{Li}(p,n)^{7}\mathrm{Be}$	-1.644	1.880	^{7}Be: 0.21; n: 0.03
$^{7}\mathrm{Li}(d,n)^{8}\mathrm{Be}$	$+15.031$	Exothermic	^{8}Be: 1.68; n: 13.35
$^{9}\mathrm{Be}(p,n)^{9}\mathrm{B}$	-1.850	2.057	^{9}B: 0.18; n: 0.023
$^{9}\mathrm{Be}(d,n)^{10}\mathrm{B}$	$+4.361$	Exothermic	^{10}B: 0.40; n: 3.96

To leverage a solid target irradiation station, the choice of target may either be lithium or beryllium. As can be seen in Figure 2.9, $^{7}\mathrm{Li}(p,n)^{7}\mathrm{Be}$ channel has higher neutron production yield (that is, more neutrons are created per proton) compared to beryllium. Beryllium also has the lowest neutron binding energy [10] which makes it suitable for neutron production. Examining Table 2.5, due to low melting point of lithium and excellent thermal conductivity of beryllium, proceeding with the latter is ultimately more feasible. Moreover, beryllium has lower gamma-to-neutron ratio, and hence produces less unwanted gammas [40]. But although beryllium is easier to cool with a liquid water cooling system, it is a highly toxic metal that should be handled with care, as incautious exposure to its dust or fumes can lead to serious health

issues.

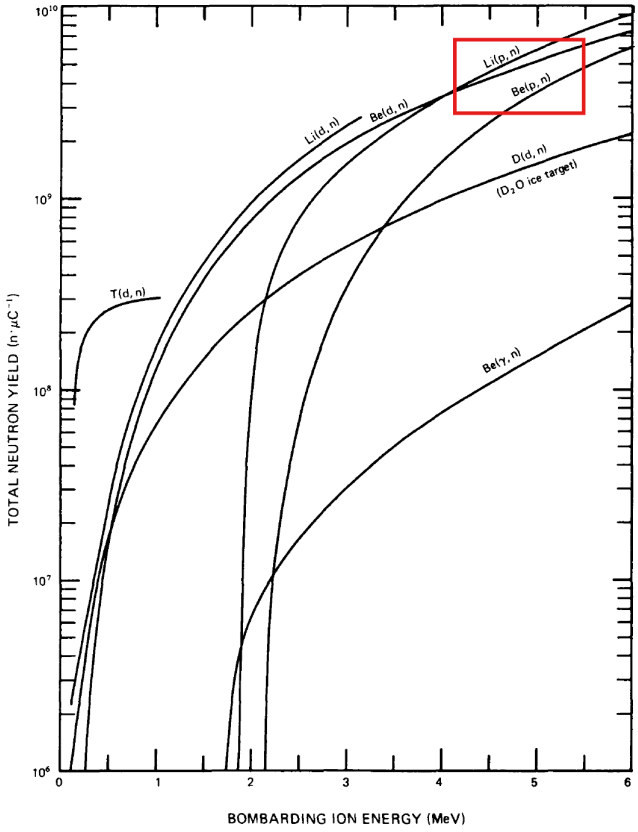


Figure 2.9: Comparison of neutron yields of (Li, Be, T, D) target materials that are irradiated with either D or ^{1}H. Irradiating lithium with protons in the energy interval 1.9 and 6 MeV produces a higher yield of neutrons than beryllium.[34]

Table 2.5: Comparison of lithium and beryllium for neutron production.

Property	**Lithium**	**Beryllium**
Neutron Production Reaction	$^{7}\mathrm{Li}(p,n)^{7}\mathrm{Be}$ $[E_{\mathrm{thr}} = 1.9\,\mathrm{MeV}]$	$^{9}\mathrm{Be}(p,n)^{9}\mathrm{B}$ $[E_{\mathrm{thr}} = 2.1\,\mathrm{MeV}]$
Melting Point (°C)	181	1287
Thermal Conductivity (W/(m·K))	71	210
Radioactive Decay Products	$^{7}\mathrm{Be}$ $[E_{\mathrm{thr}} = 2.1\,\mathrm{MeV}]$	$^{7}\mathrm{Be}$ $[E_{\mathrm{thr}} = 13.4\,\mathrm{MeV}]$

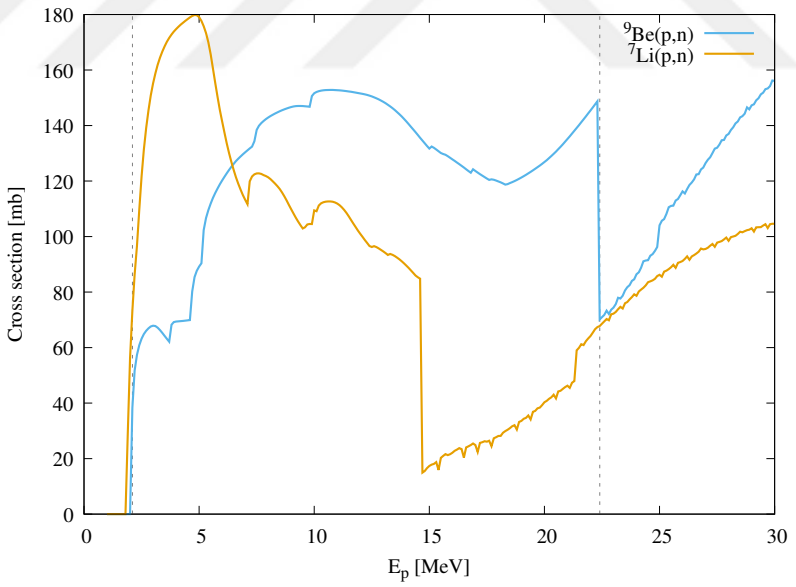


Figure 2.10: Beryllium and lithium neutron production cross-section using protons comparison. Obtained with TALYS.

CHAPTER 3

BERYLLIUM IN NUCLEAR PHYSICS FOR NEUTRON PRODUCTION: MONTE CARLO APPROACHES AND EXPERIMENTAL BACKGROUND

Beryllium has been previously implemented in various institutes for the purpose of neutron production, which will be explained in Section 3.1. These works prove that beryllium can be successfully implemented in various fields requiring a neutron beam.

To model the probable outcome of the proposed setup that is capable of producing neutrons from a beryllium target, Monte Carlo approaches have been used. As such, introduction to Monte Carlo method, as well as the experimental background will be given now.

3.1 The Beryllium Channel and The Previous Beryllium Studies for Neutron Production

Since 1970s, proton/deuterium-beryllium reactions have been studied extensively. This reaction channel has been tested and implemented in various research institutes and radiopharmaceutical centers. For example, BNCT is a type of radiation therapy that utilizes the high neutron absorption cross-section of boron that is injected to patient with cancer. If the boron captures a neutron, it emits an alpha particle that destroys the surrounding cancer infected tissue. For the purpose of Boron Neutron Capture Therapy (BNCT), Kyoto University Research Reactor Institute (KURRI) and Sumitomo Heavy Industries, Ltd. (SHI) collaborated to develop a cyclotron based neutron source using beryllium. It is currently installed at KURRI Osaka preface, and is capable of reaching thermal neutron flux of $1.7 \times 10^9/\text{cm}^2/s$ using 1 mA proton beam with kinetic energy 30 MeV [55]. The neutron beam's characteristics align

perfectly with the IAEA's (International Atomic Energy Agency) established requirements for BNCT, which are given in Table 3.1. Their work successfully proves that beryllium target stations can be implemented in medical fields.

Table 3.1: Mandatory values for epithermal neutron beam required for BNCT, based on IAEA TECDOC (Technical Documents) [21]

Particle Intensity	**Required value**
Epithermal neutron	
$\times 10^9$ epi-neutron/cm^2/s	
(0.5 eV – 10 keV)	> 1.0
Fast neutron (> 10 keV)	
$\times 10^{-13}$ Gy cm^2/epi-neutron	< 2.0
Gamma ray	
$\times 10^{-13}$ Gy cm^2/epi-neutron	< 2.0

Another exemplar use has been demonstrated by NPI Rez Fast Neutron Facility, where thick Be, D_2O and Li(C) target stations are utilized to construct high energy neutron field [67]. High energy neutron field production can further be amplified by using deuterium as the projectile particle. In Table 3.2 comparison of neutron fields generated from both deuterium and proton is given. It is seen that using deuterons rather than protons as the projectile is more advantageous. But Proton Accelerator Facility can currently only accelerate protons. Average neutron energy was calculated according to relation $\bar{E}_n = (0.47 \cdot E_p) - 2.2$ [19]. Compared to protons, using deuterium results in higher neutron current for higher energy intervals, but for the purpose of this thesis proton induced reactions will be of interest, as it is the preferred source of TENMAK NUKEN and METU DBL. TENMAK NUKEN's proton cyclotron accelerates protons in the energy interval [15,30] MeV. The studies in this thesis will focus on this interval. Any other energy outside this interval would require considerable cyclotron modifications. Most studies of neutron fields have been conducted with proton energies below 5 MeV. Above 2.1 MeV (the threshold for (p, n)

reaction), RFQ (radio-frequency quadrupole) may also be deployed to irradiate the beryllium target with high proton current (in the orders of mA). Many of these studies anticipate increase in neutron flux with increasing proton energy. For instance in Figure 3.1, the increase in neutron yield with respect to the increase in proton energy can be seen. In Figure 3.2, higher neutron mean energies due to proton energies can also be observed.

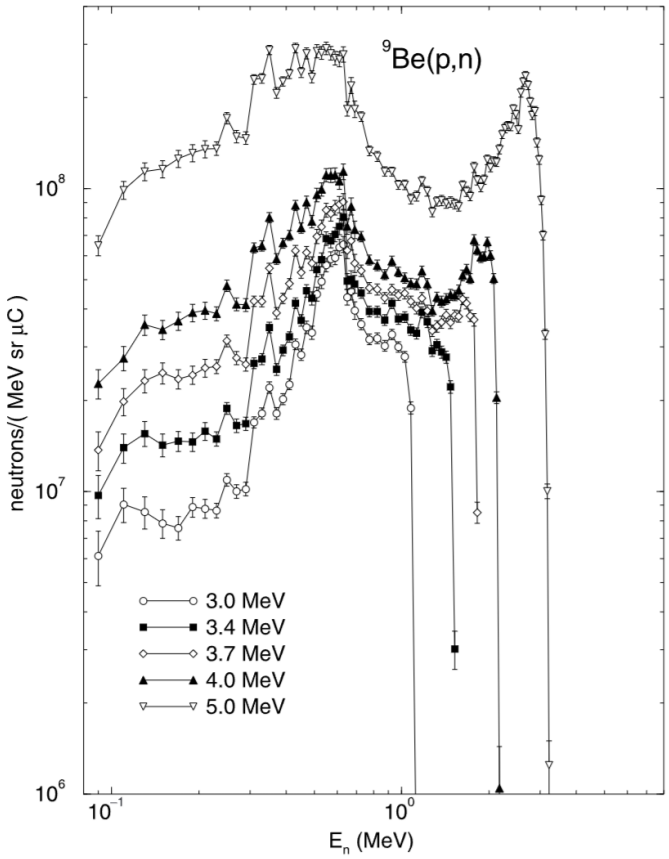


Figure 3.1: Low energy $^9\mathrm{Be}(p, n_0)$ reaction neutron spectrum and yield for ground state Be, with various proton energies between 3.0 and 5.0 MeV. [36]

For a 30 MeV proton beam, the obtainable neutron energy spectrum is given in Figures 3.3 and 3.4.

The resulting neutron field spans a large energy interval. Energy levels down to 1×10^{-4} MeV are anticipated. This lower energy section of spectrum is caused by the

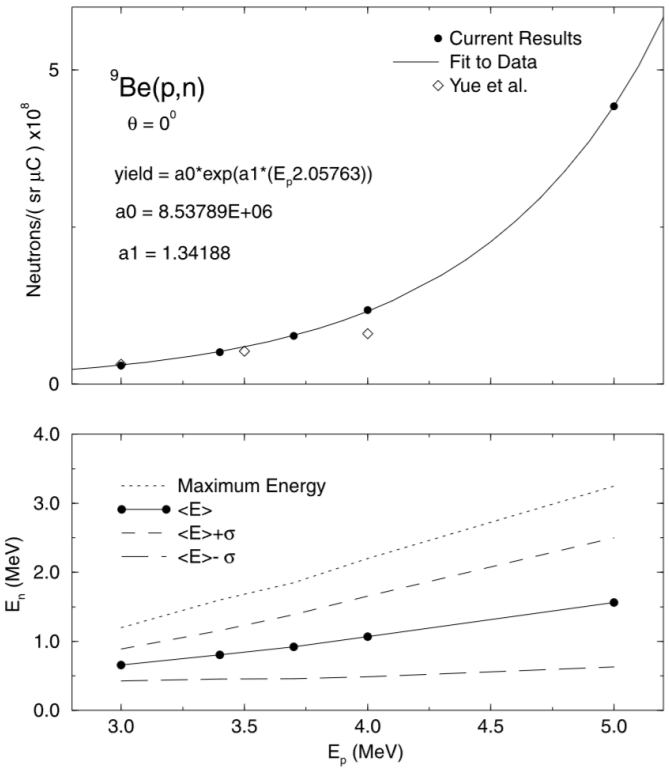


Figure 3.2: Neutron yield with respect to different proton energies and respective mean neutron energies. In the upper panel, neutron yield with respect to different low energy proton levels from 3.0 to 5.0 MeV is given. In the lower panel, mean neutron energy and its first moment of its energy distribution is given. [36]

multi-body breakup processes [68]:

$$^{9}\mathrm{Be}(p,\, pn)\, ^{8}\mathrm{Be},$$
$$^{9}\mathrm{Be}(p,\, p\alpha)\, ^{5}\mathrm{He},$$
$$^{9}\mathrm{Be}(p,\, \alpha n)\, ^{5}\mathrm{Li},$$
$$^{9}\mathrm{Be}(p,\, p\alpha n)\, ^{4}\mathrm{He}.$$

which all posses negative Q values.

Quasi-isotropic neutron distribution can be seen in Figure 3.4. It is observed that the neutrons are produced in 4π direction and span the entire azimuthal angle ϕ, hence novel collimators are required to construct and channel a proper neutron beam. In Figure 3.2, the mean distribution of neutron energy and yields with respect to different proton energies are given. It is observed that there is a considerable increase in yield as the proton energy increases. The yield will later be studied over a wide range of proton energies extensively in Chapter 5.

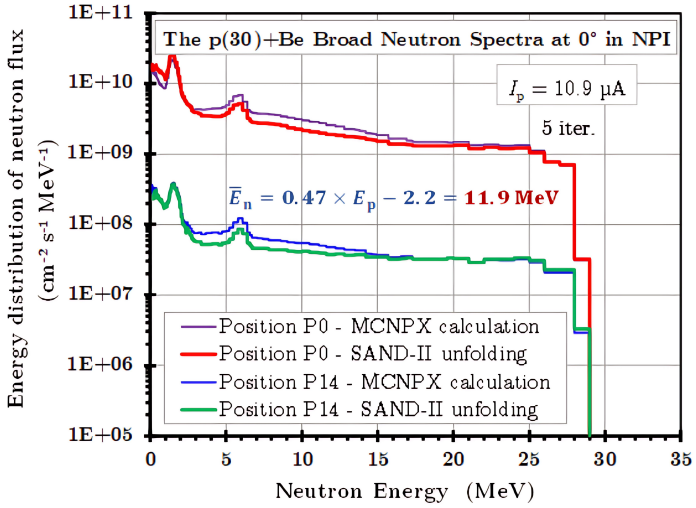


Figure 3.3: Spectral flux and mean energy of neutrons resulting from p(30)+Be at different detector locations P0 and P14. Data from MCNPX and SAND-II calculations are compared.[68]

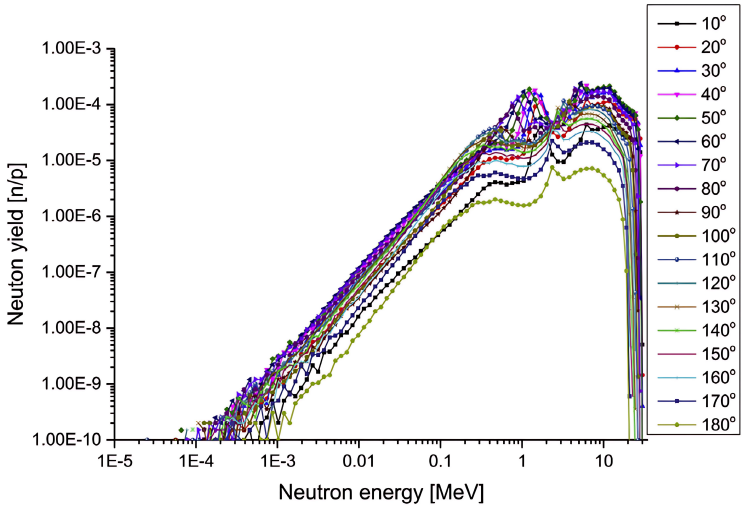


Figure 3.4: Neutron yield and energy spectrum for p(30)+Be, calculated at various detector angles extending from 10° to 180°.[40]

The resulting neutron field of p(30)+Be reaction, given in both linear plot for higher energies in Figure 3.3, and logarithmic for lower at various detector angles in Figure 3.4. Target thickness is 5.2 mm.

Table 3.2: Neutron emission characteristics for the $^{9}\mathrm{Be}(d,n)$ and $^{9}\mathrm{Be}(p,n)$ reactions at zero and $0°$–$40°$ detector angle. I_Ω represents the neutron current at solid angle Ω. [49]

Reaction	**Energy (MeV)**	**Zero degrees**		$\theta = 0°$–$40°$
		$\bar{E}_n$ (MeV)	I_Ω (10^{16} n/sr · s · A)	$\int I_\Omega \, d\Omega^c$ (10^{16} n/s · A)
$^{9}\mathrm{Be}(d,n)$	8.0	3.7	0.6	0.6
	14.8	5.1	3.8	3.1
	18.0	5.8	6.3	4.7
	23.0	7.5	11.8	8.2
$^{9}\mathrm{Be}(p,n)$	14.8	3.0	1.35	1.9
	18.0	3.4	1.9	2.8
	23.0	4.9	3.0	4.4

3.2 Hydrogen Blistering Inside Target

If low energy protons are in use, there is a risk of embrittlement caused by the gradual deposition of hydrogen inside the target. This hydrogen deposition is the result of proton range falling behind the total penetration depth. Stated differently, if the thickness of the target is significantly less than the Bragg peak of protons within beryllium, this suggests that the protons stop entirely inside the target and subsequently fill it gradually. This deposition then inflates the embrittled layer [7], leading to cracks and damages inside the target, possibly leading to disintegration. Avoiding this phenomenon and its adverse effects requires careful evaluation of stopping power and Bragg peak of protons inside beryllium. Precautionary measures can be taken by investigating and solving the Bethe-Bloch formula.

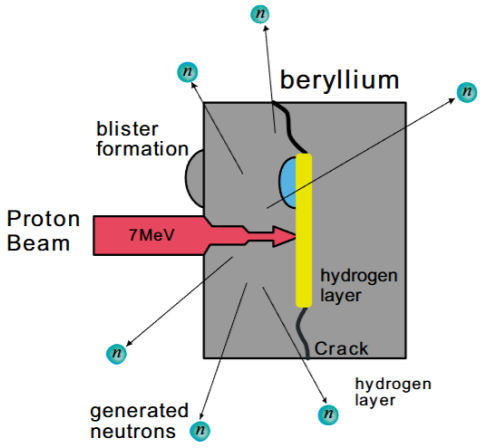


Figure 3.5: Illustration of hydrogen embrittlement inside beryllium. [76]

3.2.1 Bragg Peak and Bethe-Bloch Formula

The mean rate of energy loss per unit distance travelled inside a medium is given by the Bethe-Bloch formula. For heavy charged particles such as protons, the equation is given as [11]:

$$-\left\langle \frac{dE}{dx} \right\rangle = K\rho z^2 \frac{Z}{A}\frac{1}{\beta^2}\left[\frac{1}{2}\ln\left(\frac{2m_e c^2\beta^2\gamma^2 T_{\max}}{I^2}\right) - \beta^2 - \frac{\delta(\beta\gamma)}{2}\right] \tag{3.1}$$

which gives a numerical value in the units of $[\mathrm{MeV/cm}]$ where A is the atomic mass of absorber ρ is the density of the medium, I is the mean excitation potential of the material, β is the velocity of the particle divided by the speed of light c, z is the atomic number of the incident particle (here, proton) and capital Z is the atomic number of the absorber, with some fundamental constants:

$$K = 4\pi N_A r_e^2 m_e c^2 = 0.307 \text{ MeV cm}^2/\text{mol} \tag{3.2}$$

$$r_e = \frac{e^2}{4\pi\epsilon_0 m_e c^2} \approx 2.8 \text{ fm} \tag{3.3}$$

T_{max} is the maximum energy transfer of a single collision which can also be derived from:

$$T_{\text{max}} = \frac{2m_e c^2 \beta^2 \gamma^2}{1 + 2\gamma\frac{m_e}{M} + \left(\frac{m_e}{M}\right)^2} \approx \begin{cases} 2m_e c^2(\beta\gamma)^2 & m_e \ll M \\ \gamma M c^2 = E & \gamma \to \infty \\ m_e c^2(\gamma - 1) = E - m_e c^2 & M = m_e \end{cases} \tag{3.4}$$

$\delta(\gamma\beta)$ is the density effect correction to ionization loss, which is relevant for relativistic velocities, and γ is the relativistic factor. In some cases, the stopping power is divided by ρ and written in the units of $\mathrm{MeV/cm^2/g^{-1}}$ for convenience. Overall, the mean stopping power is characteristic, hence can be utilized to identify particles inside a known medium (detector) [23]. Another characteristic feature is the outcome of the mean stopping power. If the stopping power versus path length is to be plotted, the immediate peak just before a complete stop is called the Bragg Peak. As the particle travels and slows down gradually, the energy deposition becomes larger. This is due to decreasing value of β. $1/\beta^2$ grows exponentially as the particle slows down. The location of the Bragg Peak may be regarded as the point where maximum energy deposition occurs. This peak can effectively be utilized. For instance after determining a tumors' depth, oncologists adjust the energy of the proton beam to deliver maximum amount of dose to this area while delivering minimal dose to healthy tissue along the path. In the case of beryllium, the proton range and stopping power is investigated to locate the Bragg peak, and hence it is aimed to keep the target thickness well below this point. If the proton range exceeds the target thickness, blistering effect becomes irrelevant.

3.3 Methods of Solving Particle Transport Equations

Differential equations have profound applications in physics. Heat conduction, fluid mechanics, hydrodynamics, magnetohydrodynamics, electrohydrodynamics etc. all serve as exemplars of applied differential equation solutions [54]. A system with several degrees of freedom may also have a moderate amount of particles. Having such, each single one of these particles requires their own analytical solution. This would require an immense computation power that would simply scale up with the increasing particle count. The traditional methods of computation would become impractical in this sense. Advancement in modern computational methods have enabled practical simulation of difficult mathematical problems, such as the behavior, interaction, and transportation of particles inside a medium. The probabilistic nature of the quantum world, the stochastic interactions of nuclei and the Gaussian distribution of certain aspects of physics meant that analytical solutions to complex problems with moderate number of particles were far too difficult to achieve without utilizing a repeated random sampling method. Hence, numerical techniques became a necessity to solve transport problems. The deployed simulation toolkits in this thesis (GEANT4 and FLUKA) both utilize Monte-Carlo methods to estimate outcomes of nuclear reactions as well as the transport of resulting particles in a media.

3.3.1 Introduction to Monte Carlo

The simulation toolkits (Geant4 and FLUKA) played a crucial role in the estimation of parameters of interest in our experiment and are based on the Monte Carlo technique. In the most basic sense, Monte Carlo method is the utilization of random numbers to sample the phase space and to solve a non-analytical problem. All Monte Carlo calculations are hence equivalent to integrations [39]. Deterministically, it may be impossible to predict the exact value of a random variable, but for many aspects in nuclear physics, the *distribution* of its possible values are known. For instance, the cross-section of a particular process over a wide range of energies may be obtained experimentally. Although this data is plotted deterministically as a function of energy, the outcome is inherently random. As such, for neutrons, they may either scatter, undergo fission, or be absorbed, all of which are closely tied to random distributions.

A Monte Carlo code takes in experimentally determined cross-section, and randomly samples by generating events according to the probability distribution of each event over many cycles to provide a numerical solution, which is our best estimate to predict the outcome.

3.3.2 Random Sampling

Let's assume that the events (E_i) of a particular particle are mutually exclusive (that is only one of them can occur at a given time). Summing up the probability of each one of them clearly adds up to 1 ($p_1 + ... + p_n = 1$). If we choose a random number ξ, for a particular event E_i [14]:

$$p_1 + ... + p_{i-1} \leq \xi < p_1 + ... + p_i \tag{3.5}$$

And we do know:

$$\int_a^b p(x)dx = 1 \tag{3.6}$$

Now we have assigned ξ value to an individual event E_i. If we construct a probability density function as $p(x) = p_i$, the probability distribution function then becomes

$$\xi = \mathrm{P}(x) = \int_0^x \mathrm{p}(t)dt \;\; (0 \leq x < n) \tag{3.7}$$

Now x has been set as a function of ξ. Assume that we want to sample the distance to a collision. In the infinitesimal flight path dl, the probability of collision is given as:

$$\mathrm{p}(l)\, dl = e^{-\Sigma_t l}\Sigma_t\, dl \tag{3.8}$$

The collision probability per unit length is given as Σ_t, which is the macroscopic cross section. Cumulative probability can then be expressed as:

$$\xi = \int_0^l e^{-\Sigma_t s}\Sigma_t\, ds = 1 - e^{-\Sigma_t l} \tag{3.9}$$

Solving for path length l

$$l = -\frac{1}{\Sigma_t}\ln(1-\xi) \tag{3.10}$$

But $1 - \xi$ acts in the same manner as ξ, hence it can just be reduced to ξ. As a result, the collision distance is reduced to, and sampled from:

$$l = -\frac{1}{\Sigma_t}\ln\xi \tag{3.11}$$

Similar technique can be approached to sample solid angle Ω, to estimate the direction of an outgoing particle. For simplicity, let us assume that the distribution is spherically symmetric (i.e isotropic). If every patch of $d\Omega$ receives the same contribution, probability density function $p(\theta, \varphi)$ can be written in terms of independent variables θ, φ:

$$p(\theta,\varphi)\,d\theta\,d\varphi = \frac{d\Omega}{4\pi} = \frac{\sin\theta\,d\theta\,d\varphi}{4\pi} = \underbrace{\frac{\sin\theta}{2}}_{\theta \text{ coefficient}}\,d\theta \cdot \underbrace{\frac{1}{2\pi}}_{\varphi \text{ coefficient}}\,d\varphi \tag{3.12}$$

Here, we can sample via inverse transform sampling (ITS). For any random variable X having cumulative distribution function $F_X(x)$, x can be sampled by generating a random number ξ between the interval $[0, 1]$[53]. Setting $\xi = F_X(x)$ and solving for $x = F_X^{-1}(\xi)$ then results in the variable of interest. Given that we already know the coefficient of θ using the separation of variables,

$$p_1(\theta) = \frac{\sin\theta}{2} \text{ where } \theta \in [0, \pi] \tag{3.13}$$

$F_\Theta(\theta')$ is just:

$$\begin{aligned} F_\Theta(\theta') &= \int_0^{\theta'} p_1(\theta)\,d\theta \\ &= \int_0^{\theta'} \frac{\sin\theta}{2}\,d\theta \\ &= \frac{1}{2}\left[-\cos\theta\right]_0^{\theta'} \\ &= \frac{1}{2}(-\cos\theta' - (-\cos 0)) \\ &= \frac{1}{2}(1 - \cos\theta') \end{aligned} \tag{3.14}$$

Using the randomly generated ξ and setting $\xi_1 = F_\Theta(\theta')$, we get:

$$\xi_1 = \frac{1 - \cos\theta'}{2} \tag{3.15}$$

From this, we can solve for $\cos\theta'$:

$$2\xi_1 = 1 - \cos\theta' \quad \Longrightarrow \quad \cos\theta' = 1 - 2\xi_1 \tag{3.16}$$

$$\theta' = \arccos\left(1 - 2\xi_1\right) \tag{3.17}$$

Sampling of φ can be done in the same manner. Considering $p_2(\varphi) = \frac{1}{2\pi}$ for $\varphi \in [0, 2\pi]$. Cumulative distribution function is written as:

$$F_\Phi(\varphi') = \int_0^{\varphi'} p_2(\varphi)\,d\varphi = \int_0^{\varphi'} \frac{1}{2\pi}\,d\varphi \tag{3.18}$$

$$\xi_2 = \frac{1}{2\pi}\int_0^{\varphi} d\varphi' \tag{3.19}$$

$$\xi_2 = \frac{1}{2\pi}\left[\varphi'\right]_0^{\varphi} = \frac{1}{2\pi}(\varphi - 0) = \frac{\varphi}{2\pi} \tag{3.20}$$

$$\varphi = 2\pi\xi_2 \tag{3.21}$$

We have related ξ_1 and ξ_2 with polar angles θ and φ, which were needed to construct the new direction of the outgoing particle. Using:

$$\sin\theta = \sqrt{1 - \cos^2\theta} \tag{3.22}$$

We have new the directions:

$$\begin{aligned} \Omega_x &= \sin\theta\cos\varphi \\ \Omega_y &= \sin\theta\sin\varphi \\ \Omega_z &= \cos\theta \end{aligned} \tag{3.23}$$

3.3.3 The Rejection Technique

In some cases, applying the inverse transform sampling to a CDF might not be as straightforward. Even when there is no CDF or no full form of PDF to work with, the rejection sampling can still be utilized. To sample a random variable in the interval $[a, b]$, another distribution $p^*(x)$ is introduced by normalizing $p(x)$ with its upper bound (supremum) [15, 57, 12]. $p^*(x)$ is just any arbitrary function that only needs to satisfy two criteria: it needs to be *similar* to our original function $p(x)$, and it needs to be easy to sample from.

$$p^*(x) = \frac{p(x)}{\textbf{Sup}\ p(x)} = \frac{p(x)}{Max} \tag{3.24}$$

This new distribution has the exact shape as $p(x)$, but it is divided by the upper bound so the maximum value is 1. This means $0 \leq p^*(x) \leq 1$. Then, we introduce a random variable pair (ξ, η), both in the range $[0, 1]$. Assuming that we are interested in the sample x', we introduce:

$$x' = a + \xi(b - a) \quad a \leq x \leq b \tag{3.25}$$

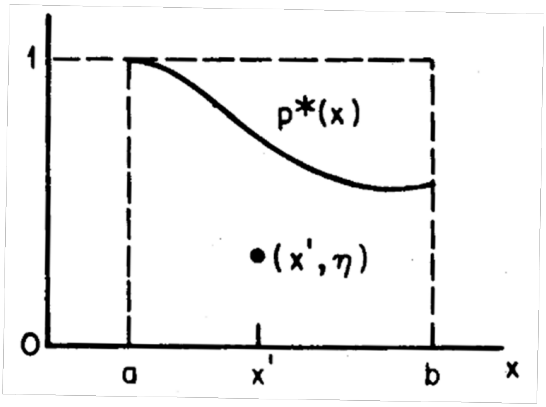


Figure 3.6: The chosen points under the bounded area of normalized density function $p^*(x)$. [14]

This also means that x' is uniformly distributed over $[a, b]$. Setting η as the threshold height, sample x' is only accepted if

$$p^*(x') > \eta \tag{3.26}$$

And rejected otherwise. The iteration of generating ξ and η continues until the condition is satisfied. In Figure 3.6, the points (x', η) which are uniformly distributed in the rectangle $[a, b] \times [0, 1]$ is shown. Let us consider a small strip dx. In the interval $[x, x + dx]$, probability of generating x' is:

$$dx/(b - a) \tag{3.27}$$

As we have a uniform distribution of x in the range [a,b], the probability of accepting this sample is represented by $p^*(x')$, which is due to $\eta \in U[0, 1]$. Then the joint probability, which is the multiplication of generating x' in $[x, x + dx]$ **and** accepting it can be given by:

$$P(\text{accept and } x' \in [x, x + dx]) = P(\eta < p^*(x')) \cdot P(x' \in [x, x + dx]) \tag{3.28}$$

$$= p^*(x') \cdot \frac{dx}{b - a} \tag{3.29}$$

Substituting $p^*(x') = \frac{p(x')}{M}$ Equation 3.28 becomes:

$$= \frac{p(x')}{M} \cdot \frac{dx}{b - a} \tag{3.30}$$

This gives the distribution of the *accepted* points. $p_{\text{accepted}}(x)$, is proportional to this probability.

$$p_{\text{acc}}(x)\, dx \propto \frac{p(x)}{M(b - a)}\, dx \tag{3.31}$$

This is the intended result. By sampling from a generated function $p^*(x)$, we can also indirectly sample from our original probability density $p(x)$, whose exact form was unknown. Geometrically speaking, this is the ratio of the proportional area of the small strip dx under the curve $p^*(x)$, over the total area under it.

$$\frac{p^*(x)\,dx}{\int_a^b p^*(x)\,dx} = \frac{p(x)\,dx}{\int_a^b p(x)\,dx} = p(x)\,dx \tag{3.32}$$

3.3.4 Phase Space and Flux Estimation

Phase space is defined as a set which comprises all possible physical states of a given system [58]. It is a way of analyzing the evolution of dynamical systems by representing each dimension with a unique point. Each of these points have the information of instantaneous state of a system. This information, combined with classical and statistical mechanics, provides the time evolution of a system. In the case of Boltzmann transport equation, each individual particle traces a trajectory through the phase space, which has the complete history of particle's possible interactions and paths. Dimensions of this phase space consist of generalized coordinates and their conjugate momenta. A particle in three dimensions could have three spatial coordinates (x, y, z) and three momentum coordinates (p_x, p_y, p_z) (or energy and direction, E, θ, ϕ), which amounts to six dimensions. This indicates that a system with N degrees of freedom will possess a phase space of $2N$ dimensions. The restriction on the number of dimensions is not limited to six, as more dimensions may be introduced such as quantum numbers (spin). Using the corresponding dimensions, the number of particles in an infinitesimal phase-space element can be given as:

$$dN = f(x, p, t, \alpha) d^3p d^3x dt d^n\alpha \tag{3.33}$$

$f(x, p, t, \alpha)$ is the probability density function and $d^3p d^3x$ terms represent the spatial and momentum dimensions. Extra degrees of freedom can be included in $d^n\alpha$ term. The time evolution of $f(x, p, t, \alpha)$ results in the transportation of the corresponding particle, including forces and interactions. Such a function is hence the basis of the integro-differential form of the Boltzmann transport equation which in general has the base form of:

$$f(x, p, \alpha) = \iiint G(x, p, \alpha, x', p', \alpha') f_0(x', p', \alpha') d^3p' d^3x' d^n\alpha' \tag{3.34}$$

Here, G represents a multidimensional operator which accounts for all microscopic interactions. As the nature of particle transport and interactions in a given media of interest is stochastic, particle transport equations are described by probability distributions. Acquiring analytical solutions are hence eliminated, but taking the integral over the region of interest in the phase space gives a numerical solution (or estimation, as FLUKA calls it. Detectors in FLUKA are called estimators). This means that the simulations (or calculations) are an attempt at solving the Boltzmann equation at numerical level.

For a system containing various particles, another degree of freedom may very well be the particle itself, as each of these unique particles will have their own phase space dependent on their disparate interaction and transport mechanism.

Transportation of particles in a phase space are governed by the Boltzmann transport equations [37]. The derivation of the equation given below is valid for neutrons and gamma rays. Any other particle with a non-net zero charge will involve electromagnetic interaction terms as well, but any particle that goes under a stochastic interaction can be subject to such equation governed by linear Boltzmann equation. For example for neutrons, assuming the particles have linearity (interactions are independent of each other. They do not influence each other's probability), the integro-differential form of the steady state transport equation can be given as [60]:

$$\hat{\Omega} \cdot \nabla\phi(\bar{r}, \bar{E}) + \Sigma_t(\bar{r}, \bar{E})\phi(\bar{r}, \bar{E}) = S(\bar{r}, \bar{E}) + \int \Sigma_s(\bar{r}, \bar{E}' \rightarrow \bar{E})\phi(\bar{r}, \bar{E}')d\bar{E}' \quad (3.35)$$

On the left-hand side, $\hat{\Omega}$ is the solid angle unit vector which is in the direction of particle motion. $\phi(\bar{r}, \bar{E})$ is the angular flux of particles and $\Sigma_t(\bar{r}, \bar{E})$ is the total macroscopic cross-section, which is the sum of absorption and scattering cross-sections. $\bar{E}$ here, represents the direction and magnitude of the *flow* of the energy $(E, \hat{\Omega})$. In summary, in a volume element, the first terms are the leakage of a particle out of the element, and the second term is the rate of change due to interactions such as removal due to absorption or scattering out of a volume. This means the left-hand side is the total number of particles coming out of a volume. The right-hand side accounts for the gain of particles of interest. Their source could be from scattering or any other

source. If the explicit time dependency is present, equation 3.35 becomes:

$$\underbrace{\frac{1}{v}\frac{\partial\Phi(\mathbf{r},\hat{\Omega},E,t)}{\partial t}}_{\text{time dependency}} + \underbrace{\hat{\Omega}\cdot\nabla\Phi}_{\text{translation (flow)}} + \underbrace{\Sigma_t(\mathbf{r},E)\,\Phi}_{\text{absorption}} - \underbrace{S(\mathbf{r},\hat{\Omega},E,t)}_{\text{source}} = \underbrace{\iint \Phi(\mathbf{r},\hat{\Omega}',E',t)\;\Sigma_s\big(\mathbf{r},\hat{\Omega}'\to\hat{\Omega},\;E'\to E\big)\,\mathrm{d}\hat{\Omega}'\,\mathrm{d}E'\,.}_{\text{differential scattering}} \tag{3.36}$$

Here, $\Sigma_t = \sigma_t N_a \rho/A$ is the total macroscopic cross-section (probability of any interaction) and $\Sigma_s = \sigma_s N_a \rho/A$ is the total scattering macroscopic cross-section. Expanding the gains and losses, the rate of accumulation of particles in a given element can be given as:

$$\begin{aligned}\frac{1}{v(E)}\frac{d\Phi(\mathbf{r},\hat{\Omega},E,t)}{dt} &= -\Omega\cdot\nabla\Phi(\mathbf{r},\hat{\Omega},E,t)\\ &\quad - \Sigma_r(\mathbf{r},\Omega,E)\Phi(\mathbf{r},\Omega,E,t)\\ &\quad + \chi(E)\int_{E'}dE'\int_{\Omega'}d\Omega'\;\nu\Sigma_f(\mathbf{r},\Omega',E')\Phi(\mathbf{r},\Omega',E',t)\\ &\quad + \int_{E'}dE'\int_{\Omega'}d\Omega'\;\Sigma_s(\mathbf{r},\Omega'\to\Omega;E'\to E)\Phi(\mathbf{r},\Omega',E',t)\end{aligned} \tag{3.37}$$

Here, contribution from fission has also been added in the right-hand side as a sum. $\chi(E)$ represents the energy spectrum produced in fission, and the last term in the sum is the scattering of neutrons from the direction and energy of Ω', E' to Ω, E. This integro-differential form is not yet suitable for a Monte Carlo study. In order to transform the equation into a single integral equation, and hence be able to carry out the integral over all histories (path lengths R) to conduct numerical analysis, the time independent integral can be re-written as:

$$\phi(\mathbf{r},E) = \int_{R=0}^{\infty} \underbrace{e^{-\int_0^R \Sigma_t dR'}}_{\substack{\text{for no collison}\\ \text{over } R}} \times \left[\underbrace{S(\mathbf{r}',E)}_{\text{source}} + \underbrace{\int \Sigma_s(\mathbf{r}',E'\to E)\phi(\mathbf{r}',E')dE'}_{\substack{\text{particles}\\ \text{scattered into } E}}\right] dR. \tag{3.38}$$

Breaking down the terms:

- $e^{-\int_0^R \Sigma_t dR'}$: This factor is responsible for cases where no interaction occurs (i.e the particle traverses R without colliding with any particle along the trajectory). At a given point in phase space, Σ_t is the macroscopic cross section.

This implies that the integral is the cumulative probability of interaction. If we exponentiate this with a minus sign, we end up with the probability of *not colliding*.

- $\int \Sigma_s(\mathbf{r}', E' \rightarrow E)\phi(\mathbf{r}', E')dE'$: When scattering happens, a new state with energy E' is introduced. If we multiply the differential scattering cross-section at any given $\mathbf{r}'$ and integrate over possible E' values, we will end up with the number of scattered particles at $\mathbf{r}'$.

Going over equation 3.38, we can summarize this integral operation as: at an arbitrary distance R along $\hat{\Omega}$ the direction, there will be some particles that has undergone no interaction and hence survived until position vector $\mathbf{r}$, with its probability given in exponential term. At the source point $\mathbf{r}'$, a new particle may be created, or scattered. Integrating all of these terms over all of the possible trajectories R henceforth results in the anticipated particle flux. A Monte Carlo simulation toolkit utilizes this equation in its code by estimating or randomly sampling these corresponding terms inside the integral. Solving the equation hence requires at least one source, and one detector where a solution of the Boltzmann equation is being sought. The necessary parameters such as the direction of the outgoing particle, scattering angle etc need to be randomly sampled from a probability distribution.

3.3.5 Calculation of Particle Yield Inside Target Volume

Reaction yields can further be deduced from the particle fluence $\varphi_i[\text{cm}^{-2}]$. To find the neutron reaction yield in a tiny proton energy slice $E + dE$, we can write:

$$y_R(E)\,dE \;=\; \underbrace{\varphi_i(E)}_{\frac{N_i}{A_T}} \times \underbrace{\sigma(E)}_{\substack{\text{reaction}\\ \text{cross section}}} \times \underbrace{\frac{N_A\, f_T}{M_T}\, dm_T}_{\substack{\text{number of}\\ \text{target nuclei in } dm_T}} \tag{3.39}$$

By solving Equation 3.39, the number of neutrons in a tiny mass strip dm_T can be calculated. To have a more *natural* sense of calculation, it is better to write this equation in terms of a thin slice dx rather than dm_T.

$$dm_T = \underbrace{\rho_T}_{\substack{\text{mass density}\\ (\text{g/cm}^3)}} A_T\, dx \tag{3.40}$$

Substituting into dm_T and cancelling dA_T, it can be written as:

$$y_R(E)\,dE \;=\; \frac{N_i}{A_T}\,\sigma(E)\,\frac{N_A\,f_T}{M_T}\,(\rho_T\,A_T\,dx) \;=\; N_i\,\sigma(E)\,\frac{N_A\,f_T}{M_T}\,\rho_T\,dx \tag{3.41}$$

To have in the units of "per energy" instead of "per thickness"

$$y_R(E) \;=\; N_i\,\sigma(E)\,\frac{N_A\,f_T}{M_T}\,\rho_T\,\frac{dx}{dE}\,[\text{MeV}^{-1}\text{s}^{-1}] \tag{3.42}$$

Last term in 3.42 is familiar. It is the mass stopping power, in the units of MeV cm^2 g^{-1}. So far, we have assumed that yield of interest does not explicitly depend on time. In addition to formation of desired nuclei, there are negatively contributing terms to yield, such as self-depletion (loss of target nuclei due to knock-backs and nuclear reactions), absorption (although it may not be relevant if the particle of interest is a particular nucleus, it is useful if the observed particle is neutron) and active decay. Modifying Equation 3.42 [1]:

Formation of Residual Nuclei:

$$d\,(y_R(E,t))|_{\text{formation}} = N_i\,\sigma(E)\,\frac{N_A f_T}{M_T}\left(\frac{dE}{dx}\right)^{-1}\frac{dt}{\Delta t} \tag{3.43}$$

Self Depletion:

$$d\,y_R(E,t)|_{\text{depletion}} = -\frac{Y_n(E_0)}{A_T}\,\langle\sigma_R(E)\rangle\,y_R(E,t)\,dt \tag{3.44}$$

Absorption:

$$d\,(y_R(E,t))|_{\text{abs}} = -\frac{y_n(E)}{A_T}\,\langle\sigma_A(E)\rangle\,\frac{N_A f_A m_T}{M_T}\,\frac{dt}{\Delta t} \tag{3.45}$$

Decay:

$$d\,(y_R(E,t))|_{\text{decay}} = -\lambda_R\,y_R(E,t)\,dt \tag{3.46}$$

where λ_R is the decay constant of the residual nucleus, $Y_n(E)$ is the total neutron yield. Putting it all together we have:

$$\begin{aligned}\frac{d\,(y_R(E,t))}{dt} = {} & N_i\,\sigma(E)\,\frac{N_A f_T}{M_T}\left(\frac{dE}{dx}\right)^{-1}\frac{1}{\Delta t} \\ & - \frac{Y_n(E_0)}{A_T}\,\langle\sigma_R(E)\rangle\,y_R(E,t) \\ & - \frac{y_n(E)}{A_T}\,\langle\sigma_A(E)\rangle\,\frac{N_A f_A m_T}{M_T}\,\frac{1}{\Delta t} \\ & - \lambda_R\,y_R(E,t)\end{aligned} \tag{3.47}$$

Now, as calculations require definite time intervals, the ordinary differential equation above can be integrated over finite irradiation time Δt. The formation term can be treated as constant in time. For a monoenergetic, steady and constant current proton beam, we will see no time evolution. Separating the solution:

$$y_R(E, \Delta t) = \underbrace{N_i \frac{N_A f_T}{M_T} \sigma(E) \left(\frac{dE}{dX}\right)^{-1}}_{\text{Formation}} \times \theta(\Delta t), \tag{3.48}$$

where $\theta(\Delta t)$ is given by

$$\theta(\Delta t) = \frac{\Omega_T}{\Delta t} \cdot \frac{1}{\left(\lambda_R + \langle \sigma_R \rangle \frac{y_n}{A_T}\right)} \left(1 - \exp\left[-\left(\lambda_R + \langle \sigma_R \rangle \frac{y_n}{A_T}\right) \Delta t\right]\right) \tag{3.49}$$

This is the solution of a standard first-order linear ODE (ordinary differential equation). The target absorption factor:

$$\Omega_T(E) = \left(1 - m_T \frac{f_A}{f_T} \frac{\langle \sigma_A \rangle}{\sigma(E)} \frac{y_n(E)}{N_i A_T} \frac{dE}{dX}\right) \tag{3.50}$$

Integrating over an energy interval [0,E_0] we have:

$$Y_R(E_0, \Delta t) = N_i \frac{N_A f_T}{M_T} \int_0^{E_0} \frac{\sigma(E)}{\frac{dE}{dX}(E)} \theta(\Delta t)\, dE. \tag{3.51}$$

In summary, the equations governing the particle yields, trajectories, and fluences need random sampling methods to be utilized in Monte Carlo simulation toolkits. This chapter has been written to provide a fundamental understanding of how these simulation tool kits basically operate.

CHAPTER 4

EXPERIMENTAL STATION DESIGN OF METU-NIDA AND DESCRIPTION OF COMPUTATIONAL TOOLS

The proposed experimental setup is planned to be implemented onto the existing METU-DBL infrastructure. The planned location of the target station, as well as the requirements that need to be considered will be discussed here. The computational tools that will be employed to simulate the proton-beryllium reaction will also be detailed in this chapter.

4.1 METU Defocusing Beam-Line

METU Defocusing Beam-Line (DBL) has been designed to conduct high atmosphere and deep space ionizing radiation tests. In accordance with ESA ESCC No.25100 standard, tests on avionics and multiple different electronic components such as ASICs, FPGAs, coating layers and shielding materials for LEO (Low Earth Orbit) and GEO (Geo-Stationary Orbit), optical lenses and structural elements can all be conducted. These tests are aimed at simulating Single-Event-Effects (SEE) in harsh space radiation environments. It is located in the R&D room of TENMAK-NUKEN Proton Accelerator Facility (PAF). The beam line is an extension that advances from a single port of the five-port switching magnet. It is capable of delivering a proton beam in the energy range 15-30 MeV with fluxes ranging from $\sim 10^6$ to $\sim 10^{10}$. protons$/\mathrm{cm}^2/\mathrm{s}^{-1}$ [42] Because of its modular design, the current infrastructure can be expanded upon and improved. In Figure 4.1, the beam-line can be seen. In Figure 4.2, the setup and its components are shown. Using 3 quadrupole magnets, the proton beam is expanded to 15.40 × 21.55 cm area to comply with ESA radiation test

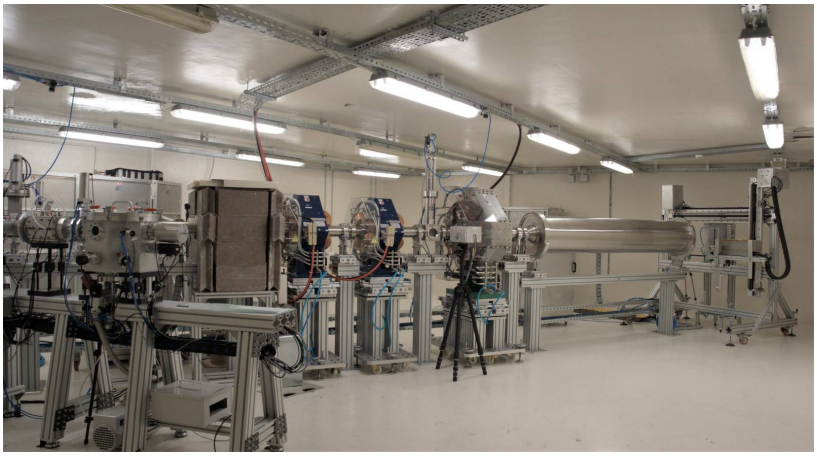


Figure 4.1: METU-DBL.

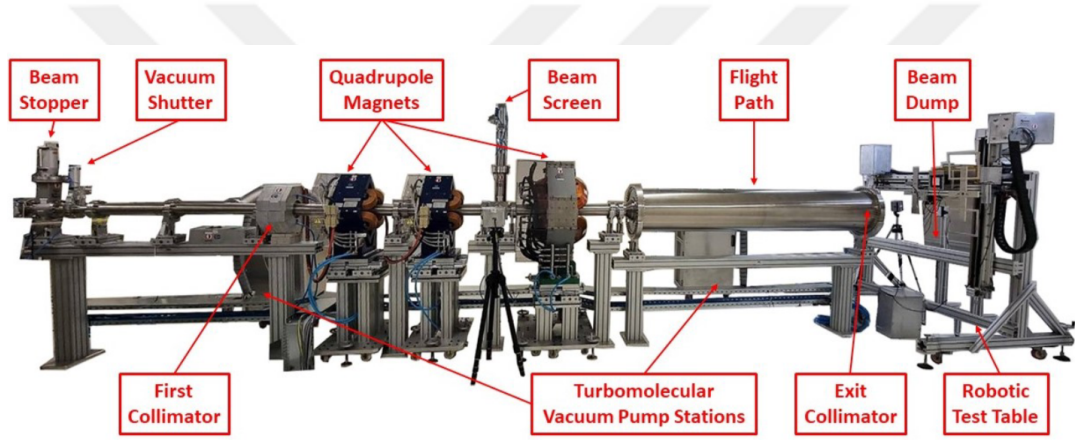


Figure 4.2: The METU-DBL Test Setup. [42]

standards.

Respectively, METU-DBL setup consists of a beam stopper, vacuum shutter, collimator, quadrupole magnets, beam screen, flight path, exit collimator and a beam dump. The required vacuum is supplied by the turbomolecular vacuum pump stations. Just after beam stopper and vacuum shutter, there is a vacant spot for neutron irradiation station. A stainless steel beam pipe can be seen in Figure 4.3 marked with a red outlined rectangle. This pipe can easily be removed, and be replaced with our target design for producing neutrons that is compatible with the dimensions and the volume of the available space.



Figure 4.3: The planned location of the target irradiation setup, outlined in red.

4.2 The Beam Screen

The name of the proposed target station is METU-NIDA, which stands for Middle East Technical University Neutron Irradiation and Distribution Area. METU-NIDA needs to be designed under the below considerations:

- The station shall not interrupt the regular space radiation operations of METU-DBL. Hence, the target should be able to enter and exit the beam-line on demand.
- The beryllium target needs to be irradiated in vacuum to not activate the air in the room and be compatible with the rest of the beam-line. Vacuum also prevents oxidation and degradation of beryllium which can lead to generation of beryllium dust (highly toxic). Hence, the whole setup shall be connected to IVMER's turbomolecular vacuum pump system.
- The beryllium target needs to be cooled down to avoid possible melting and disintegration. Target station has to be cooled with forced convection water cooling system, same as the rest of the METU-DBL.
- The continuity of the beam-line needs to be conserved. In the direction of the

beam (in simulations, it has been assumed as z axis using the right-handed coordinate system), there is no unoccupied space to establish the irradiation station. Hence, by taking advantage of the quasi-isotropic nature of neutron distribution, a station perpendicular to the proton beam direction is proposed. In x direction, there is enough space for the experimental setup.

To address these requirements, our proposal is the modification of the existing beam screen design. As such, the vacant spot shown in red in Figure 4.3 has dimensions suitable for additional installation of a beam screen apparatus. The beam screen

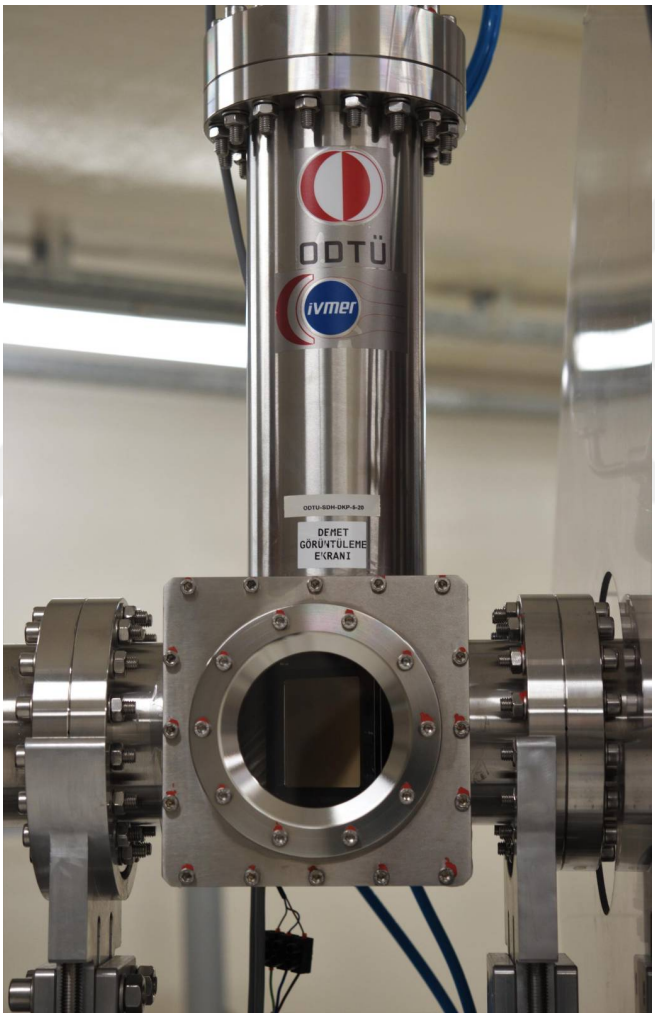


Figure 4.4: Side view of the beam screen which is currently installed on DBL. *IVMER*

is shown in Figure 4.4 and Figure 4.5. The target platform can be seen in the middle. This is where the beryllium is planned to be mounted on. This screen is currently being used for the visual analysis of beam profile. In space radiation tests, the beam

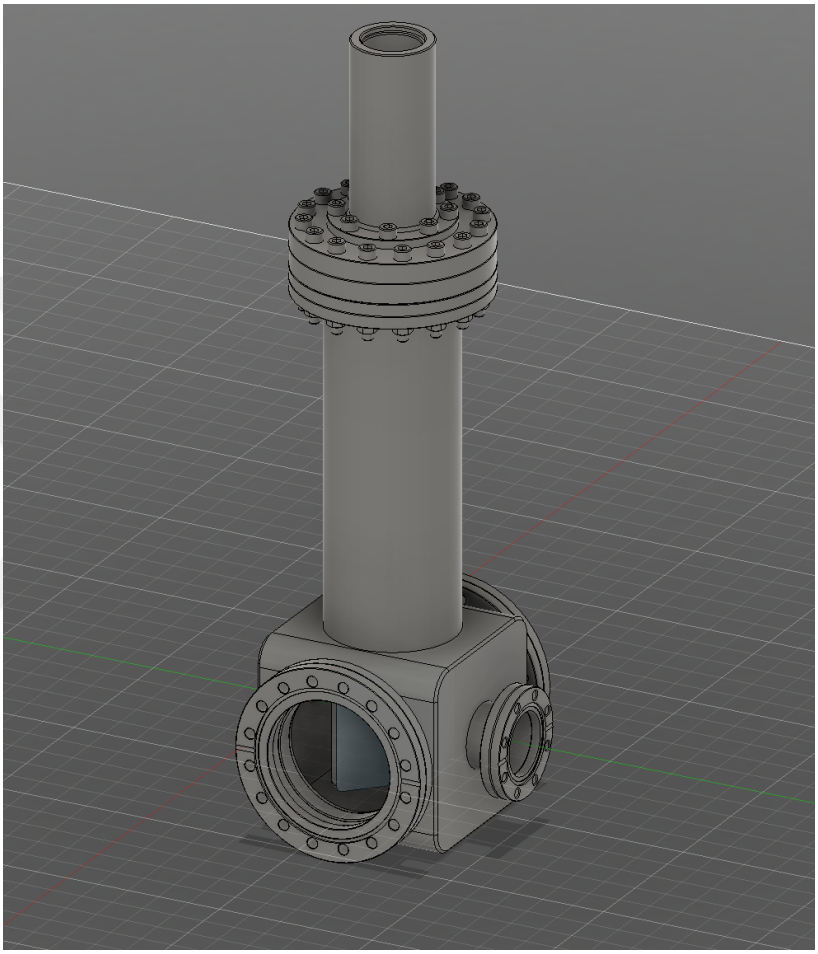


Figure 4.5: A 3D sketch of the beam screen which is currently installed on DBL. Designed by Zenotek.

uniformity is a critical parameter that must essentially be monitored. A pneumatic linear actuator is utilized to vertically insert and remove the beam viewing screen. The screen is designed to maintain stable vacuum and is water cooled as the beam is completely stopped by it. The visible rectangular shaped plate in the middle is illuminated upon irradiation. Its image is monitored on-line by a video camera facing it.The proposed beam screen (target holder) was installed on METU-DBL. The installed setup is seen in Figure 4.7. Beryllium target has not yet been mounted.

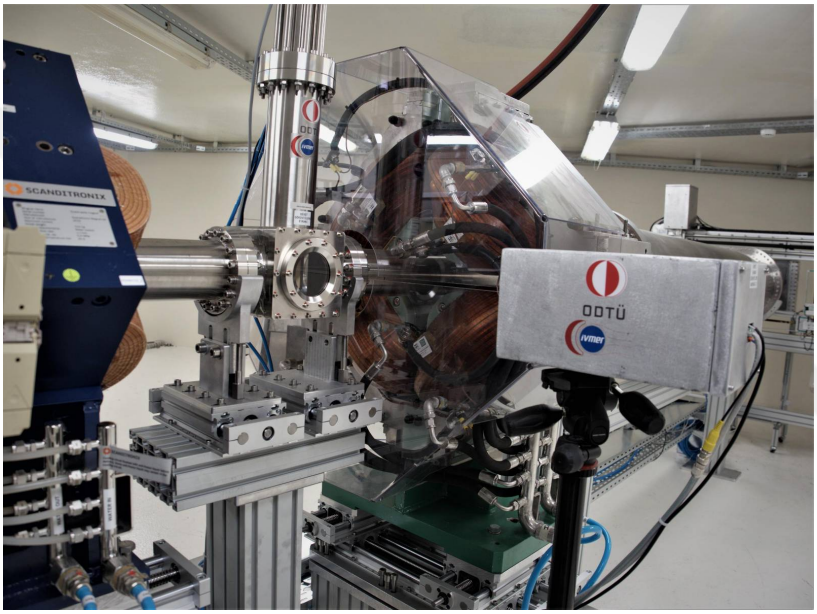


Figure 4.6: A camera has been installed to visually inspect the beam profile inside the beam screen. It is shielded to protect from the effects of ionizing radiation, which can be seen on the right. *IVMER*

This thesis proposes insertion of a thin beryllium target on top of the inner aluminum plate. More generally, by creating an insertion hole, the aluminum screen can be re-designed to hold thin solid target sheets, such as beryllium. After thorough Monte-Carlo and transient thermal analysis simulations, the target's precise dimensions are determined, and presented next.



Figure 4.7: METU-NIDA being installed.

4.3 GEANT4 Configuration and Code Description.

Geant4(GEometry ANd Tracking 4) is an open source Monte Carlo based simulation toolkit designed and developed for particle interactions and transportations. It was developed by **Geant4 Collaboration**[5, 2] which is an international community of scientists actively improving and maintaining the toolkit. The toolkit emphasizes object-oriented programming by utilizing C++. It allows flexible geometry and physics registration. Compared with FLUKA, it is more configurable in the sense that the user can switch between different models such as Binary Cascade, Bertini Cascade, INCL++ etc. For our work, suitable physics lists and geometries were presented to optimize the numerical output data which better simulates neutron production channels and the neutron transportation and interaction in the medium.

The 5 steps of a Geant4 simulations are initialization, primary event generation, tracking, stepping and event management. The first step includes geometry definition with logic volumes. The logic volume defines the properties of a volume. This includes its

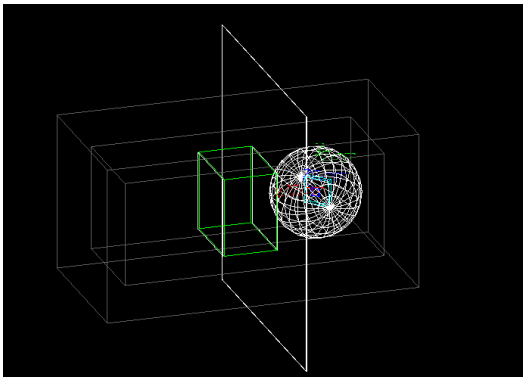


Figure 4.8: Outer geometry showing moderator (green), lead casing (gray outlines) and target-beam dump duo.

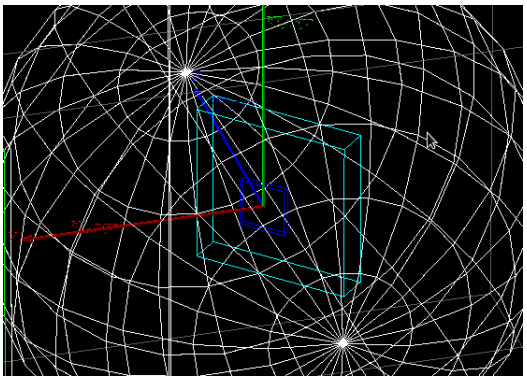


Figure 4.9: Inner geometry showing beam dump (light blue) and target(dark blue).

shape, material and size. Each unique component in our simulation (the moderator, the target, the detector etc.) was first defined as a logic volume. Positioning them in the world results in a physical volume. In Figure 4.8 and 4.9, a Geant4 geometry of proposed target moderator system with lead encapsulation for gamma shielding is shown. A Gaussian proton beam with σ of 500 keV/c and diameter of 1 cm was defined for the particle gun, and it traverses in Z axis (blue). Its energy spread of 1σ is 0.3 MeV for 30 MeV proton [78]. Using this beam profile, a particle gun was defined on the positive Z-axis. In Figure 4.8, a rectangular moderator (green) with a plane sheet in front can be seen. The thin plane vacuum sheet was used for neutron fluence projection on YZ plane to conduct neutron beam analysis. The beryllium target has dimensions 15 mm x 15 mm x 3 mm, where its thickness was determined according to the Bragg peak of 30 MeV proton inside the beryllium target, and the width was determined according to dimensions of the proton beam. It rests on an aluminum beam dump with 45 degree inclination. A thin spherical shell encompassing the beam dump-target system is implemented to measure the angular distribution of quasi-isotropic neutrons with respect to polar and azimuthal coordinates. At a 5 cm distance away on the X-axis, a plane with dimensions 50 cm x 50 cm is defined to register the neutrons. To do so, stepping action counted neutrons when the pre-step point was inside the plane, and the post-step point was inside the logic world. In both simulation toolkits, target is centered at origin (0,0,0).

4.3.1 Physics

In this work, slight modifications were imposed on radioactivation example that is preconfigured and present in the GEANT4 examples directory. As both this example and our goal handles hadronic cascade reactions, choice of hadron inelastic physics plays an important role as different physics lists can yield different results. For that, QSP_BIC_HP physics list for inelastic and HadronElasticPhysicsHP for elastic scattering have been registered. High precision (HP) addition carries utmost importance as the resulting neutron energy ranges from thermal to fast. HP enables the transport of thermal neutrons (or more generally, neutron energies < 19.5 MeV). G4NDL 3.16 (Neutron Data Library) was set for ENDF/B-VII to retrieve thermal neutron cross section. The complete list of physics list that was registered are as follows:

- **HadronElasticPhysicsHP**: Handles elastic scattering of hadrons using high-precision (HP) models, which are particularly important for low-energy neutron interactions.
- **G4HadronPhysicsQGSP_BIC_HP**: Manages inelastic scattering of hadrons. The "QGSP" refers to the Quark-Gluon String Model for high-energy interactions, while "BIC" (Binary Cascade) is used for intermediate-energy interactions.
- **G4IonElasticPhysics**: Governs elastic scattering processes for ions, such as alpha particles or heavier nuclei, ensuring an accurate treatment of nuclear interactions.
- **G4IonPhysicsXS**: Handles inelastic interactions of ions, incorporating cross-section data to improve simulation accuracy for processes like spallation or fragmentation
- **G4StoppingPhysics**: Deals with stopping mechanisms for short-lived hadrons, including processes like nuclear capture at rest and interactions of low-energy charged particles with matter.
- **GammaNuclearPhysics**: Simulates interactions between gamma rays and nuclei, including photonuclear reactions where high-energy gamma photons in-

duce nuclear disintegration.

- **ElectromagneticPhysics**: Covers electromagnetic interactions such as ionization, Bremsstrahlung, Compton scattering, and pair production, ensuring accurate modeling of charged particle and photon interactions

- **G4DecayPhysics**: Implements decay processes for unstable particles, including weak decays of elementary particles like muons and mesons.

- **RadioactiveDecayPhysics**: Models radioactive decay of nuclei, including alpha, beta, and gamma emissions, as well as spontaneous fission. This will give better sense for dose calculations around the target.

- **G4NeutronTrackingCut**: Applies tracking cuts to low-energy neutrons to improve simulation efficiency by removing very slow neutrons that would not contribute significantly to the results.

4.3.2 Fluence Estimation Principle of Geant4

The fluence estimations in Geant4 are done by normalizing the particle count inside a logic volume. The counts were obtained by investigating tracks inside logic volumes. The count was incremented by 1 when a particle's pre-step point was inside the volume of interest, and the post-step point was inside the logic world. This ensured the particle was only counted once. Neutrons with various energies were counted inside the volumes. To interpret and analyze the wide spectrum of neutron energy and hence plot a lethargy plot, logarithmic binning was essential. The binning in Geant4 is done manually in post calculation unlike the user routines feature in FLUKA. Results were acquired in counts, hence the redistribution of neutron counts to their corresponding energy bin intervals was done by a ROOT macro file. The logarithmic energy binning was applied according to[48]:

$$E_i = E_{\min} \times \left(\frac{E_{\max}}{E_{\min}} \right)^{\frac{i}{N}} \tag{4.1}$$

This ensured both FLUKA and Geant4 gave results in the same dimensions and physical quantities.

4.4 FLUKA Configuration and Code Description.

FLUKA (FLUktuierende KAskade), is a similar Monte Carlo simulation toolkit that serves the purpose of modeling particle interactions and transportations in a medium. It was a result of joint work between CERN (European Organization for Nuclear Research) and INFN (Istituto Nazionale di Fisica Nucleare) but since 2019 [3], there have been two distinct versions of FLUKA, each being maintained by CERN and INFN independently. It uses both semi-empirical and theoretical models. Most of them are proprietary so unlike Geant4, this limits the configurability. The models are more rigid in FLUKA. This work utilizes FLUKA.CERN version.

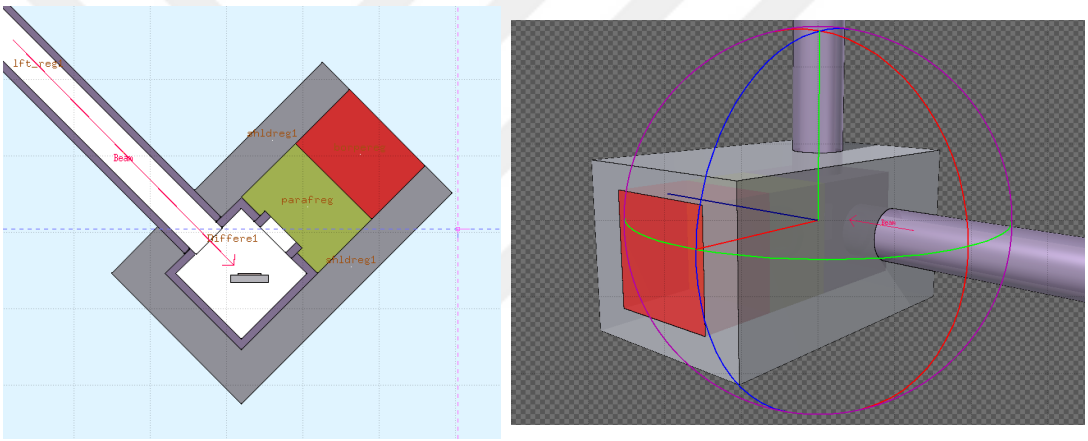


Figure 4.10: Constructed geometry of proposed setup using FLAIR and GeoViewer, graphical interface of FLUKA. The moderator pockets are shown in red and green. Target is positioned in the center. [72].

In Figure 4.10, the diagram of proposed geometry is given. Protons coming from one port of the switching magnet are introduced into the setup from the left corner (which is METU-DBL). The entrance to the moderator pockets (shown in red and green) sit at 5 cm away from the target. Each section of moderators are 5 cm. Depending on the desired neutron output energy, order, material, and thickness of moderators may be altered. For our simulations, we assumed 10 cm thick polyethylene.

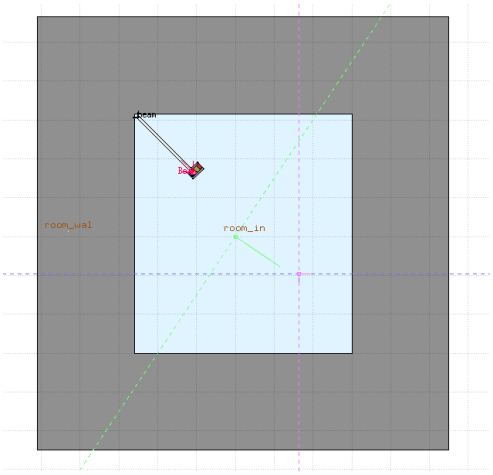


Figure 4.11: A simplified top view of the irradiation room. The outer gray box represents concrete shielding.

4.4.1 Physics

All runs were performed with FLUKA version 4-3.3. For base level predefined physics settings, "PRECISION" option was selected. This option ensures low energy neutrons are properly transported (below 20 MeV). As for additional physics, COALESCE card was activated to ensure light cluster formation takes place, which is also included in FLUKA's PEANUT model (Pre-Equilibrium and Evaporation Nuclear Model). This model is particularly useful for nuclear inelastic interactions for neutron energies above 20 MeV. Below this threshold, nuclear elastic scatterings are based on Ranft model (see [62]) and FLUKA follows group-wise approach for treatment of neutrons. This means at each energy group, reaction cross-sections are taken from evaluated nuclear databases such as ENDF, JEFF, JENDL are averaged over neutron fluence. Cross-sections calculations are hence concluded by equation (4.2)[65]

$$\sigma_i = \frac{\int_{E_{i,\text{low}}}^{E_{i,\text{high}}} \sigma(E)\Phi(E)dE}{\int_{E_{i,\text{low}}}^{E_{i,\text{high}}} \Phi(E)dE} \tag{4.2}$$

Here, $\Phi(E)$ represents the particle fluence (number of incident particles per unit area, typically in cm^{-2}, $\sigma(E)$ represents the cross-section (in barn) and E is the energy. Due to the projectile particle being a proton having an energy in the order of few MeV, the coalescence process could result in the formation of light nuclei like, $^{2}\text{H}, ^{3}\text{H}, ^{3}\text{He}, ^{4}\text{He}$ which can indirectly contribute to neutron and gamma yield via fur-

ther interactions[8]. To count neutrons more accurately, decays to neutrons shall also be taken into consideration, hence DECAYS card was also activated. Another neutron source is the nuclear evaporation process. Neutron emission from excited nuclei was activated using EVAPORAT card. All calculations were done using built-in scoring by utilization of various estimators.

4.4.2 Fluence Estimation Principle of FLUKA

Flux calculations in FLUKA inside volumes were handled by USRTRACK, where it estimates particle fluence by dividing the total track length of the responding particle by the volume.

$$\dot{\Phi}(v)dt = n(v)vdt = \frac{dN(v)}{dV}\frac{dl(v)}{dt}dt = \lim_{\Delta V \to 0}\frac{\sum_i l_i(v)}{\Delta V} \tag{4.3}$$

where $\dot{\Phi}$ is the fluence rate or flux density, which has units [$cm^{-2}s^{-1}$], N is the number of particles, $n(v)$ is the density of particles with velocity $v = dl/dt$ and V is volume. Which is in simple terms, just

$$\frac{\text{Total Track Length of Neutrons}}{\text{Total Volume}} = \phi[\text{particles per area}] \tag{4.4}$$

As the intended purpose of this proposed setup is for experiments concerning neutron irradiation without regard for net directional flow of neutrons, results will be calculated in terms of zeroth order of neutron angular flux $\Psi(r, \hat{\Omega}, E, t)$ where the neutron flux can be found as [46]:

$$\phi(r, E, t) = \int_{4\pi} \Psi(r, \hat{\Omega}, E, t)d\hat{\Omega} \tag{4.5}$$

This gives total neutron population at a given point, regardless of their direction. The current, which is the first order moment of angular flux can be found as:

$$J(r, E, t) = \int_{4\pi} \hat{\Omega}\Psi(r, \hat{\Omega}, E, t)d\hat{\Omega} \tag{4.6}$$

which is obtained by weighting Ψ with the direction $\hat{\Omega}$. This accounts for directional flow of neutrons. It can be seen that the fluence is independent of surface orientation, while current is not. We will be interested in $\phi(r, E, t)$.

4.5 TALYS Configuration and Code Description

TALYS is a nuclear reaction modelling code designed to evaluate reactions in the energy range 1 keV to 200 MeV involving light projectiles such as protons, deuterons, neutrons, tritons, $^{3}\mathrm{He}$ and alpha particles [44]. It is designed to provide a fundamental insight when comparison between experimental data and theoretical evaluations is being made. It is capable of providing cross-section data as well as production rate and inventory of residual nuclei. TALYS 1.96 was deployed to perform cross-section calculations, evaluate residual nuclei production rates, estimate yields and activities, and determine the deposited heat. The initial irradiation parameters were set as follows: proton current of 100 μA irradiates a beryllium target of area 2.25 cm^2 (1.5 cm x 1.5 cm) for 1 hour. *Ebeam* and *Eback* are set as 30 and 19 MeV respectively. This energy drop was found using FLUKA, which is explained in Section 5.9. *Tcool* time was set for 1 week. It should be noted that target orientation in TALYS is not configurable, hence all the results assume target is perpendicular to proton beam.

CHAPTER 5

SIMULATION RESULTS AND MECHANICAL FEASIBILITY

In this chapter, the simulations of the proposed setup have been conducted and results are presented. Each simulation toolkit result has been assigned to a separate section, although some sections had to be interconnected with other toolkits as some desired outcomes required joint work of multiple kits.

FLUKA was first used to plot the penetration depth and hence the Bragg peak of protons inside beryllium. These were crucial to determination of target thickness to avoid hydrogen blistering, and also to finding the highest neutron fluence. To find a suitable proton energy for a target with various thicknesses, Geant4 was used to see the fluence response to different proton energies.

5.1 Monte-Carlo Simulations of the Setup

The initial phase of the design began with deciding the target dimensions. The target thickness was determined by taking the blistering effect into consideration. Proton energies from 10 to 30 MeV were investigated to see the location of their Bragg peak. Their linear energy transfer was plotted in Figure 5.1. At the highest possible proton energy output of the cyclotron (30 MeV), the Bragg peak is expected at around ~ 0.57 cm. This implies that exceeding this target thickness threshold will greatly amplify the occurrence of hydrogen blistering. In the intervals of 1 MeV, various proton energies have been tested to find the optimal energy to get the highest neutron yield from a perpendicular target (0 $^\circ$ tilt). For a perpendicular target, in Figure 5.2, a consistent increase from 22 MeV to 26 MeV can be seen. The peak was observed at around 26 MeV. After this threshold, the yield gradually decreases.

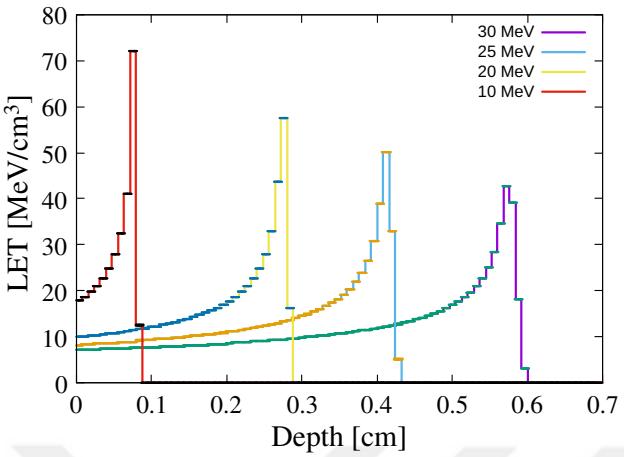


Figure 5.1: Linear energy transfer of protons with different energies inside beryllium. Obtained with FLUKA using USRBIN.

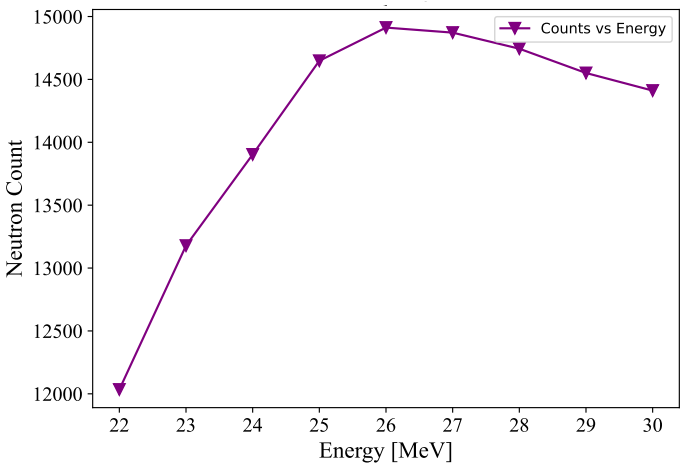


Figure 5.2: Neutron count for proton energies between 22 MeV and 30 MeV, taken at a generic point $P(x, 0, 0)$ for 3 mm beryllium target. Obtained with Geant4.

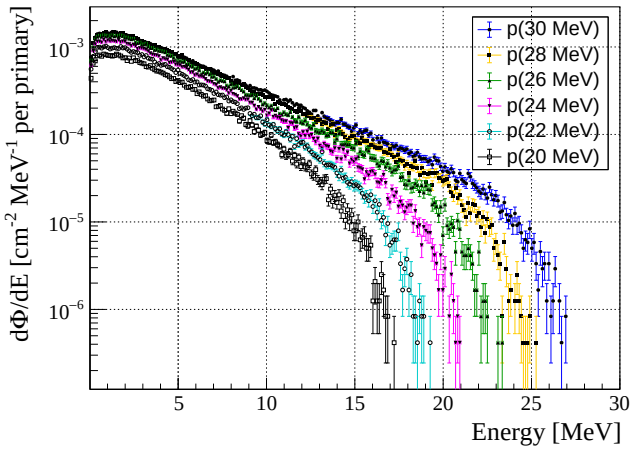


Figure 5.3: Linear plot of spectral fluence of neutrons resulting from different proton energies for 3 mm beryllium target. Obtained with Geant4.

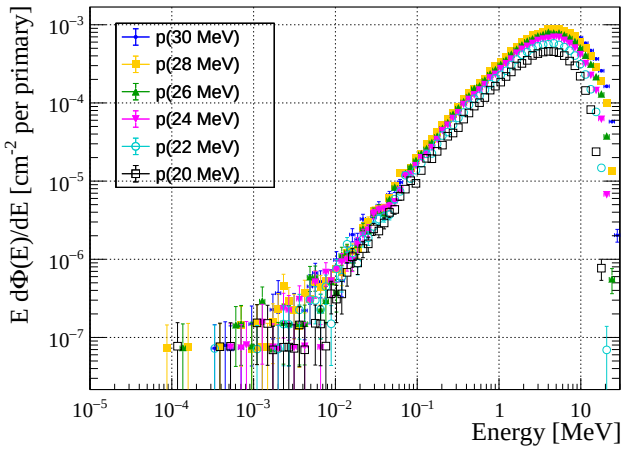


Figure 5.4: Lethargy plot of low energy spectral fluence of neutrons resulting from different proton energies 3 mm beryllium target. Obtained with Geant4

When studying the neutron yields, to observe the effect of optimal target orientation angle with respect to y axis various angles have been tested. As the proposed setup will be positioned on x axis, a random point $P(x, 0, 0)$ was chosen to estimate the effect of target orientation on neutron fluence. When the target is tilted, the outcome differs substantially than Figure 5.2. In Table 5.1, it has been found that target tilt of 45 ° results in the highest yield. Setting the target tilt as $45°$, the neutron spectral fluence was plotted in Figure 5.4 and Figure 5.3 both in linear and lethargy plots. The lethargy plots were plotted by multiplying the bin content with the bin width. This ensures lower energy contributions are not omitted when we are analyzing the graph. In contrast to linear energy graphs where the Y-axis units are $d\Phi/dE$ (MeV^{-1}, when lethargy plot is used, the Y-axis is given in $E \times \Phi(E)$, where the energy multiplication E is simply the bin width. Even though the neutron count was higher for a perpendicular target for 26 MeV protons, as shown in Figure 5.2, protons with higher energy lose their energy gradually, reaching and passing the energy point 26 MeV. Hence, 30 MeV proton energy was chosen as optimal for highest neutron yield. Higher neutron yields were observed at higher proton energies. The reason for this effect can be explained as follows: this tilt increases the effective target thickness. The effective path length of proton inside the target is now given as:

$$t_{\text{eff}} = \frac{t}{\cos 45°} \approx 1.414\, t \tag{5.1}$$

Each proton now sees more beryllium nuclei along its path. Hence, it has more chance to induce a neutron producing reaction (p, n). In Equation 3.42, we have seen that the yield is proportional to dx, i.e.

$$y_R \propto \sigma(E)\rho_T dx. \tag{5.2}$$

Tilted target means dx grows by $1/\cos\theta$. Increased dx just means more integrated area. In Table 5.2, various target thicknesses has been tested. A significant rise in neutron yield has been registered when the target thickness goes from 2.0 mm to 3.0 mm. Generally, it is observed that the yield increases in parallel with the thickness, although the rate of that increase has been found to decrease.

After fixating the target thickness at 3 mm, various runs has been conducted to calculate spectral neutron fluence, equivalent dose rate from both photon and neuron radiation, gamma spectra, energy deposition in volumes and activity of residual nuclei.

Table 5.1: Total fluence response (particles per area per primary) due to different target tilts at a point $P(x, 0, 0)$ on the x-axis for 30 MeV proton. Obtained with FLUKA using USRBDX.

Angle (°)	**Total Response (neutron/cm^2/proton)**
45	$3.3 \times 10^{-5} \pm 0.6\%$
30	$3.0 \times 10^{-5} \pm 3.0\%$
20	$2.8 \times 10^{-5} \pm 1.1\%$
10	$2.6 \times 10^{-5} \pm 2.3\%$
0 (perpendicular)	$2.2 \times 10^{-5} \pm 0.8\%$

Table 5.2: Total neutron counts for different beryllium thicknesses (30 MeV proton, $45°$ target angle). Obtained with Geant4.

Thickness (mm)	**Counts**
2.0	14 441 $\pm$120
3.0	21 244 $\pm$146
4.0	24 074 $\pm$155
5.0	24 260 $\pm$156

Putting together the optimal parameters of the experiment, geometries were drawn in both Geant4 and FLUKA

5.2 FLUKA Results

Ideal target orientation was determined by analyzing double differential fluence of neutrons using USRBDX detector card, which is an embedded boundary crossing estimator. Due to the quasi-logarithmic group energy structure of neutrons, logarithmic energy binning was imposed with 200 energy bins to study the wide energy spectrum. For the solid angle binning, we set up 15 angular bins, starting from 0 to $\pi/2$. This

angle is with respect to surface normal (i.e. target). As the target itself is positioned 45-degree angle with respect to origin, another 45-degree angle with respect to surface normal is equivalent to 90 degrees angle with respect to beam direction(i.e. polar angle θ where z axis is the beam direction).

Next, we calculated the angular distribution of neutrons with respect to azimuthal angle. In Figure 5.5, angular distribution of neutrons was registered. Neutron scattering events within a target material induce a deviation in the neutron flux trajectory, shifting it towards a more orthogonal direction. The figure on the right shows the high tendency for higher angles. For neutrons of higher energies, scattering emerges as the primary mechanism governing the channeling (or collimation) of the neutron beam. At lower energies, we observe the exact opposite. Lower energy neutrons exhibit a greater tendency to travel along paths parallel to the coordinate axes, hence motion along the directions defined by the orthogonal coordinate axes is more prevalent at lower neutron energies.

In order to compare how neutron output fluence behaves under various materials and moderation stages, initial resulting neutron count from proton-beryllium reaction was calculated using USRTRACK estimator. A USRTRACK card was defined for the target, which has dimensions of 1.5 cm x 1.5 cm with 0.3 cm thickness. This results in a volume of 0.675 cm^3 which is used by USRTRACK to normalize fluence (integrated over solid angle Ω). Figure 5.6 shows the resulting single differential energy spectrum and fluence of neutrons inside the target. Distance from the target is virtually 0, hence this can be treated as the total number of neutrons resulting from beryllium only. In order to properly evaluate the neutron fluence data, a single differential lethargy plot was also given in Figure 5.7. There is a considerable amount of neutrons present at significantly lower energies, extending to $\sim 10^{-8}$ MeV. Total neutron yield of the target was calculated using USRBDX that registers neutrons emitting from the target to the void. Integrating the result over solid angle, we obtained 2.11×10^{-3} particles per primary proton per unit area. Multiplying this value with the maximum proton operation current of 150 μA (9.37×10^{14} protons per second), we get a total neutron flux of $\sim 1.98 \times 10^{12} \pm 0.61\%$ n/cm^2/s. At a distance of 5 cm, which is the outer boundary of the beam screen, the neutron fluence decreases to 3.19×10^{-5} particles per primary proton per unit area, which when converted to flux,

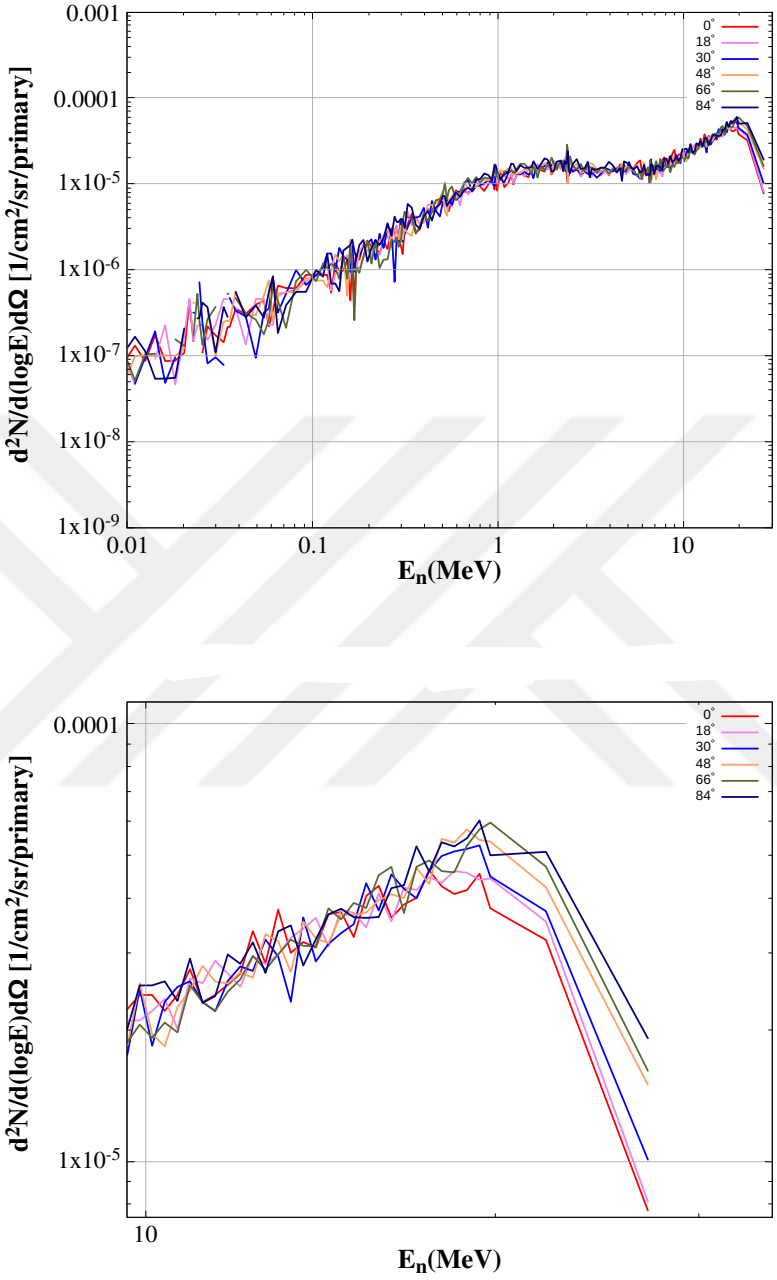


Figure 5.5: Azimuthal (ϕ) fluence distribution of resulting neutrons per primary at angles from 0° to 84° for 30 MeV proton. Obtained with FLUKA using USRBDX.

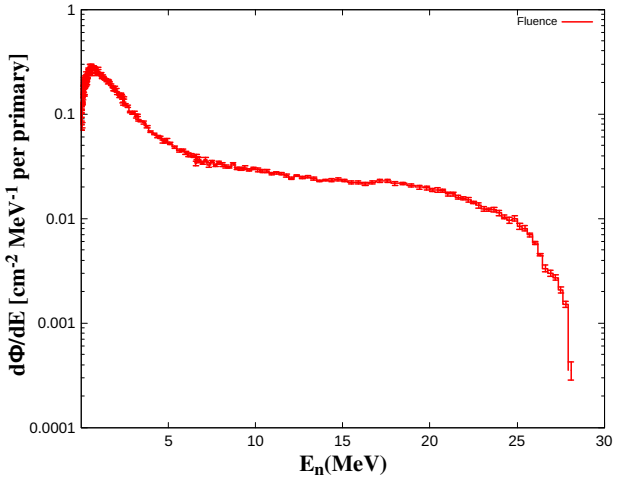


Figure 5.6: Single differential neutron fluence per primary inside beryllium target for 30 MeV proton energy, normalized with volume. Obtained with FLUKA using USRTRACK.

is $3.0 \times 10^{10} \pm 1.05\%$ n/cm^2/s. The general neutron fluence across the irradiation chamber was calculated using USRBIN. While little neutron leakage from the chamber is expected, with neutrons penetrating the surrounding walls to a certain depth, the concrete shielding of 150 cm is adequate to effectively attenuate neutron flux, as it can be seen in Figure 5.8. Consequently, no neutron readings are anticipated beyond the confines of concrete shielding. Any neutron detection outside the shielding should therefore yield a background level reading.

To calculate the dose inside the chamber, where neutron and gamma radiation contribute individually, USRBIN was utilized as well. Figure 5.9 shows the gamma equivalent dose inside the chamber. The results were given in the units of pSv/primary. The dose extends the neutron irradiation port, which has an opening that lacks lead shielding. As the outer lead shell has an opening after polyethylene moderator, gamma dose has higher value on that corresponding plane. Similar to neutrons, little to no gamma readings are anticipated beyond concrete walls.

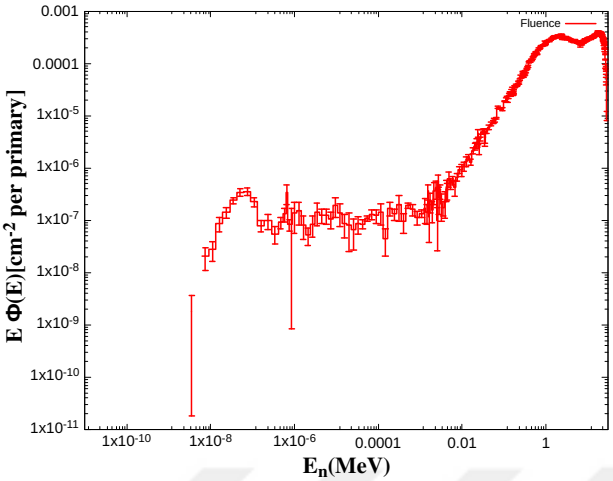


Figure 5.7: Lethargy plot of neutron fluence per primary inside beryllium target for 30 MeV proton energy. Obtained with FLUKA using USRTRACK.

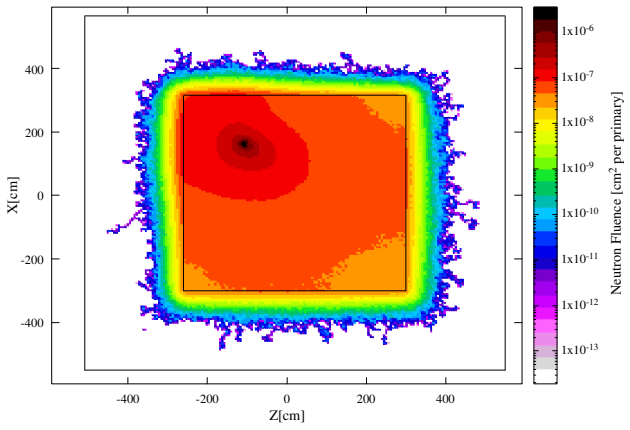


Figure 5.8: Neutron fluence across the room given in pico Sievert per primary proton for 30 MeV proton, plotted with USRBIN.

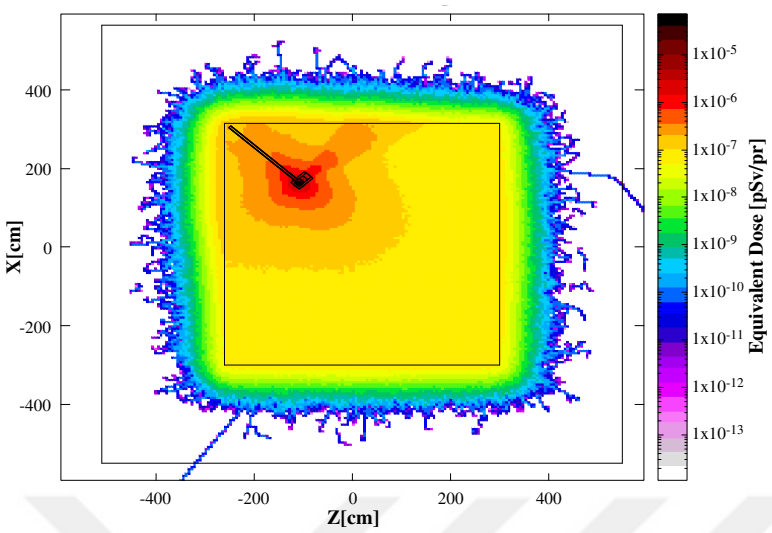


Figure 5.9: Gamma equivalent dose during irradiation inside the room given pico Sievert per primary proton (pr) for 30 MeV proton, plotted with USRBIN.

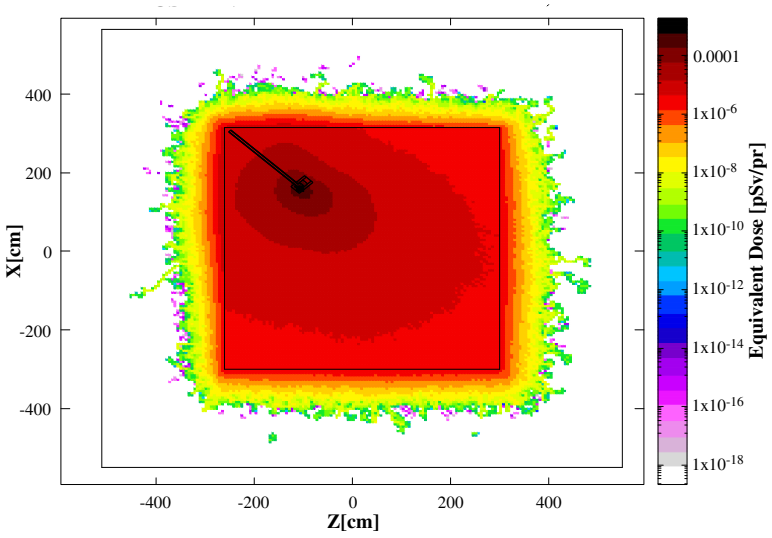


Figure 5.10: Neutron equivalent dose during irradiation inside the room given in pico Sievert per primary proton (pr) for 30 MeV proton, plotted with USRBIN.

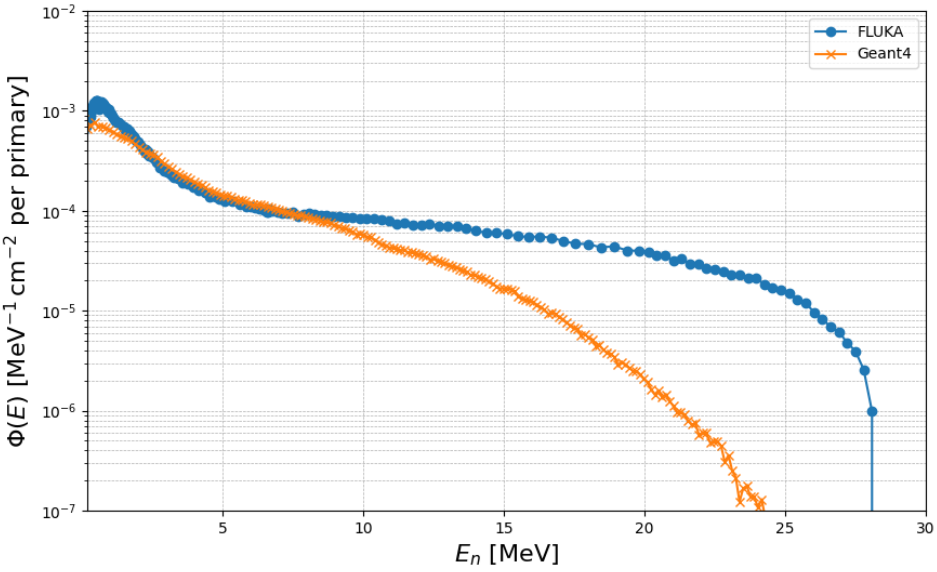


Figure 5.11: Geant4 and FLUKA comparison of fluence and energy spectrum of neutrons resulting from 30 MeV proton beam.

5.3 Geant4 Results

By registering the neutrons and their energy inside the target volume, the resulting energy spectrum was plotted. Figure 5.12 and 5.13 show neutron flux per primary and resulting spectral fluence of neutrons inside the target, normalized with volume. At lower energies (< 1 MeV), FLUKA and Geant4 agrees on neutron spectral fluence. At higher energies, the results tend to deviate from each other. This deviation can be better seen in Figure 5.11, where the fluence and spectrum obtained from Geant4 and FLUKA are compared.

Figure 5.14 shows the moderation done by polyethylene block of 20 cm and its comparison with the case where no moderator is present. The observed increase in thermal neutron concentration, as evidenced by the heightened intensity of closer peaks in lower energy bands, suggests a moderating effect induced by the presence of polyethylene. The reason is that when no moderating material is present near the beryllium target, no thermal neutrons are registered.

A thin spherical shell was used to encapsulate the beryllium target to register the

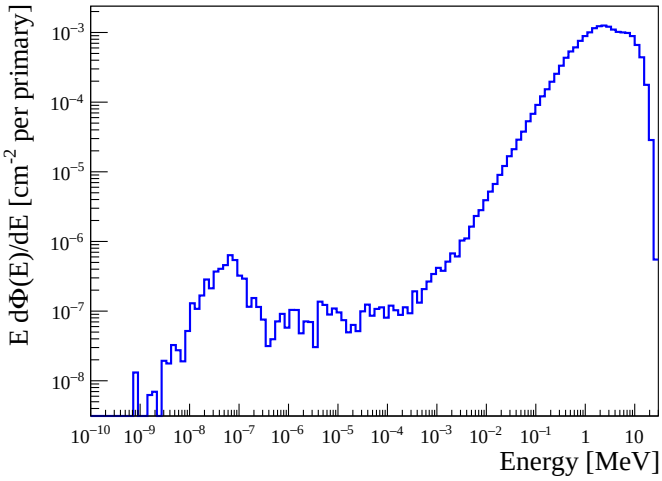


Figure 5.12: Lethargy plot of neutron spectral fluence inside the 3 mm thick beryllium target. p(30) + Be. Obtained with Geant4.

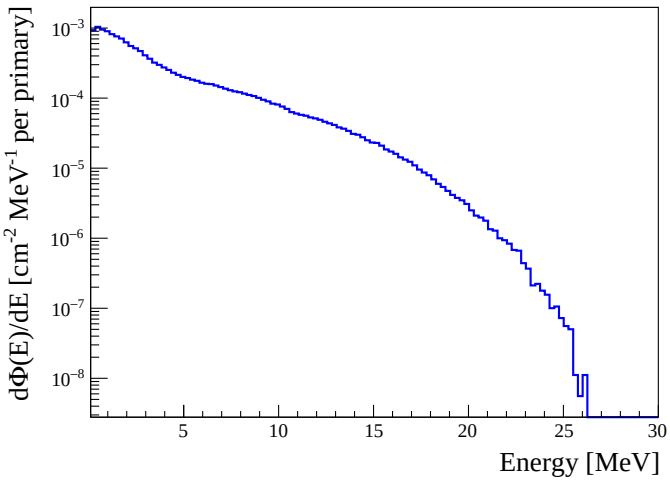


Figure 5.13: Single-differential linear plot of neutron spectral fluence inside the 3 mm thick beryllium target. p(30) + Be. Obtained with Geant4.

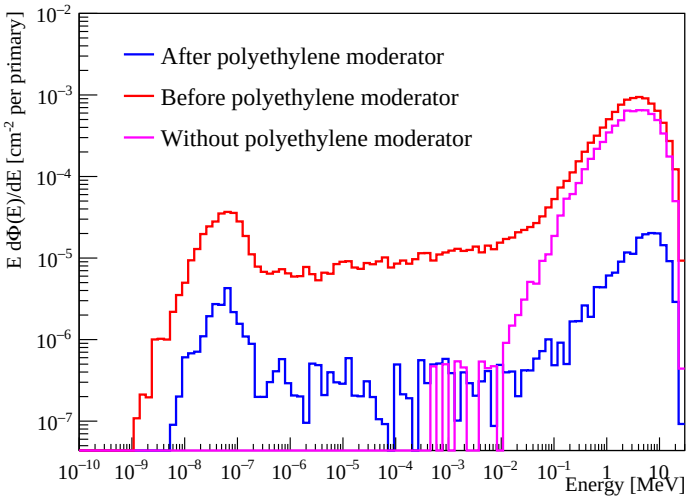


Figure 5.14: Spectral flux variations of neutrons that were produced due to 30 MeV proton beam irradiating the beryllium target. Before, after, and without moderation. Obtained with Geant4.

angular distribution of outgoing neutrons. Right-handed coordinate system was used. Θ is the angle from the positive z-axis, and Φ is the angle from the positive x-axis. A peak in neutron count around $\theta \sim 70$ was observed. The probability density function of Θ depicted in Figure 5.16 demonstrates a neutron fluence shift towards 60°–80° angle band. This shift, interpreted as a consequence of the initial target orientation, indicates the contribution of target tilt of 45 degrees to the observed beam orientation.

In Figure 5.15, the azimuthal distribution of the resulting neutrons is given. X-axis is the perpendicular to the proton beam direction, hence is the direction of the intended neutron flow. Observing higher neutron counts at 0 degrees proves that the target tilt successfully directs the neutrons in X-axis where neutron irradiation is planned to be conducted. The resulting direction of the neutrons is given in Figure 5.17 where Z-axis is the direction of the proton beam, and positive Y-axis is the upward direction, towards the ceiling.

The resulting gamma flux and spectrum was also plotted using Geant4. The peaks

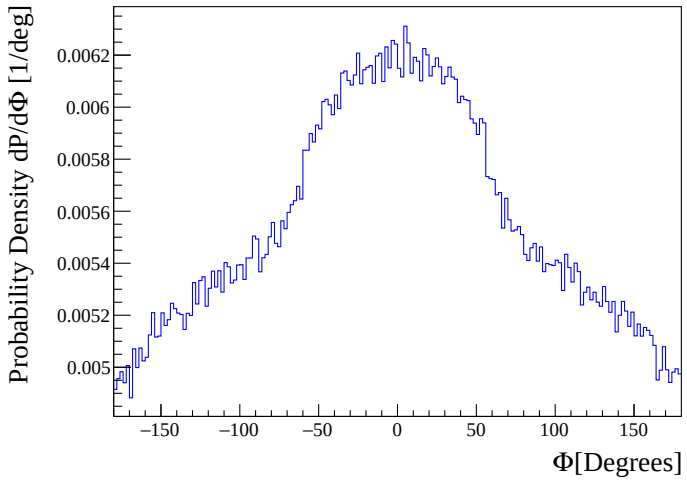


Figure 5.15: Azimuthal angular distribution of probability density function (PDF) of neutrons emerging from the beryllium target for 30 MeV protons. Obtained with Geant4.

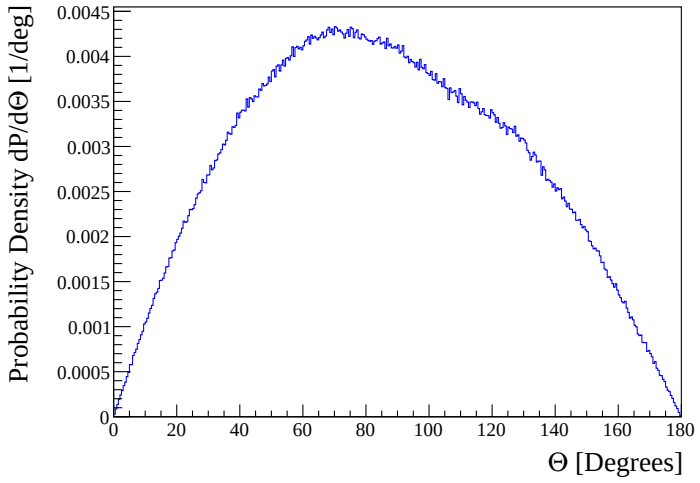


Figure 5.16: Polar angular distribution of probability density function (PDF) of neutrons emerging from the beryllium target for 30 MeV protons. Obtained with Geant4.

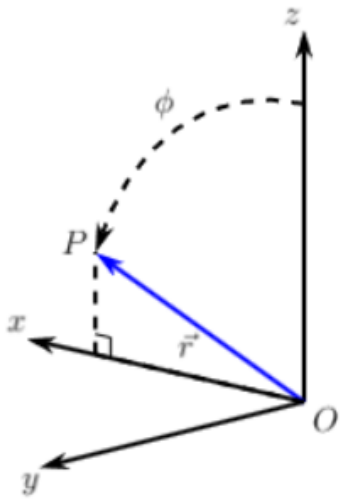


Figure 5.17: Direction of maximum neutron flow where $\theta = 70, \phi = 0$ in spherical coordinates. The notation for θ and ϕ are reversed.

are thought to be the result of residual nuclei that were produced due to irradiation of both the beryllium target and the aluminum dump. The non-stable residual nuclei that were produced is given in Table 5.3.

Table 5.3: Geant4 was used to generate an output that lists all the produced isotopes with count>1 and non-stable mean lives.

Nucleus	Count	Mean life
^{26}Al	2536	1.0351×10^6 y
^{26}Al*	928	1.8034 ns
^{28}Al	3	3.2388 min
^{10}B*	3	1.02 ns
^{7}Be	15	76.78 d
^{6}He	3	1.1638 s
^{8}Li	17	1.2117 s
^{25}Mg*	23	4.8763 ns
^{27}Mg	20	13.645 min
^{13}N	8	14.37 6min
^{24}Na	7	21.636 h
^{27}Si	437	5.9872 s

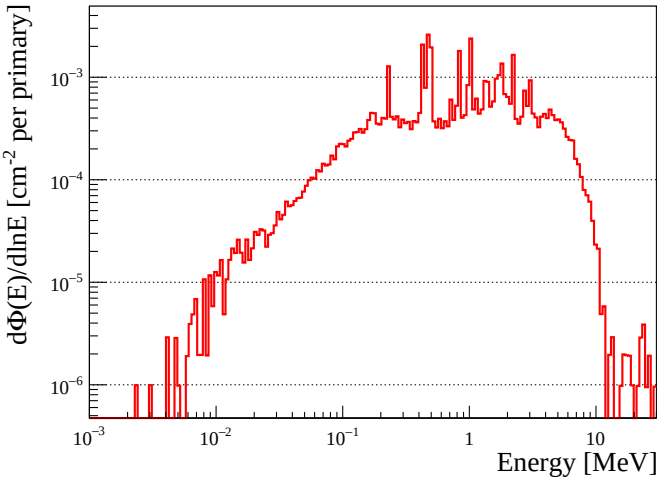


Figure 5.18: Resulting gamma flux spectrum, y-axis in logarithmic scale. Obtained with Geant4.

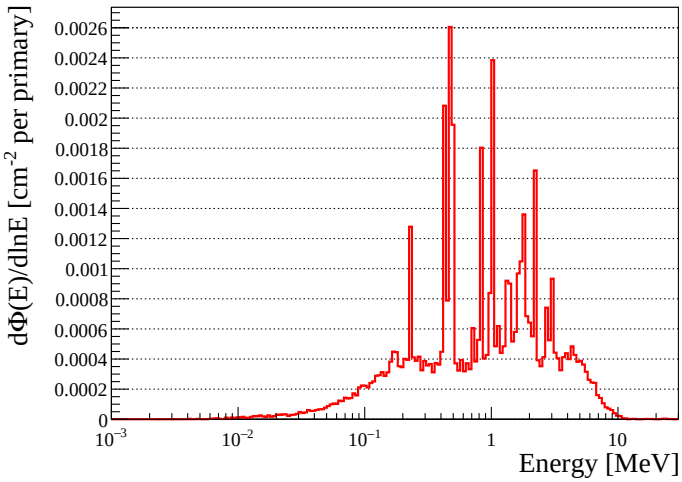


Figure 5.19: Resulting gamma flux spectrum, y-axis in linear scale. Obtained with Geant4.

5.4 Neutron Beam Distribution Profile

Figure 5.20 shows the neutron profile projected onto 50 cm x 50 cm YZ plane which is positioned at a distance of 5 cm away from the target. This is the outer surface of the METU-NIDA. The constructed neutron stream was found to follow a Gaussian profile. To determine the fitted 2D Gaussian of the neutrons, we used [66]

$$f(z,y) = A\exp\left(-\left(\frac{(z-z_0)^2}{2\sigma_Z^2} + \frac{(y-y_0)^2}{2\sigma_Y^2}\right)\right) \tag{5.3}$$

where the fitted parameters were extracted from the ROOT file. The calculated Gaussian parameters were as follows: A=749.252, y_0=0.009 cm, z_0=2.942 cm with standard deviations σ_y=14.874 cm, σ_z=14.220 cm. For comparison, the FWHM of incoming proton beam was 1.5 cm with $\sigma = 0.636$ cm, $\sigma_p = 500$ keV/c. Figure 5.21 and 5.22 shows the LEGO plot of beam profile in 2D and 3D respectively. The neutron projection spans a large area, which extends to ~ 100 cm in each direction. To collimate the beam and obtain focused neutron distribution, novel collimator designs should be implemented such as [56]. The cone that may be used is given in Figure 5.23.

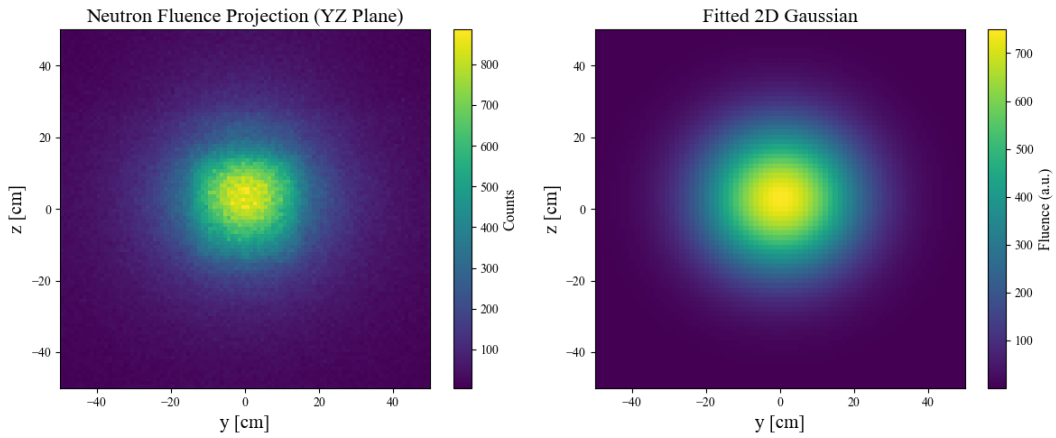


Figure 5.20: Neutron Fluence Projection and Fitted 2D Gaussian Distribution at 5 cm away from the target. Obtained with Geant4.

In conclusion, the simulations show spherical propagation of neutrons. The neutron fluence follows a Gaussian distribution. If any collimator design were to be proposed, Figure 5.20 may be studied to understand where the neutrons are concentrated.

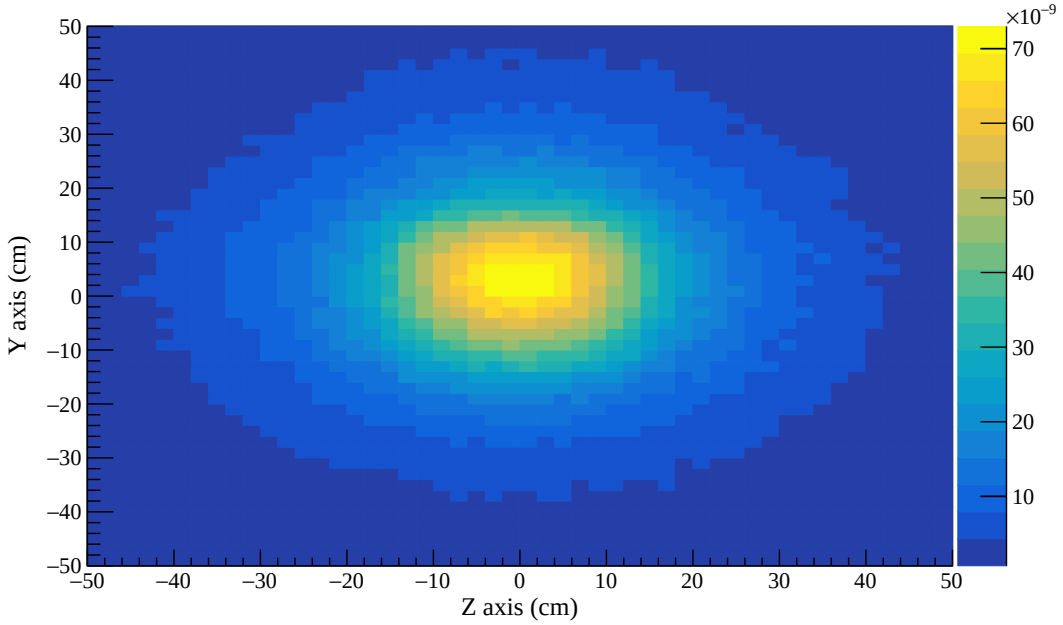


Figure 5.21: Gaussian beam profile of neutrons given in probability distribution (PDF) across YZ plane at 5 cm away from the target for 30 MeV proton on beryllium (COLZ representation). Obtained with Geant4.

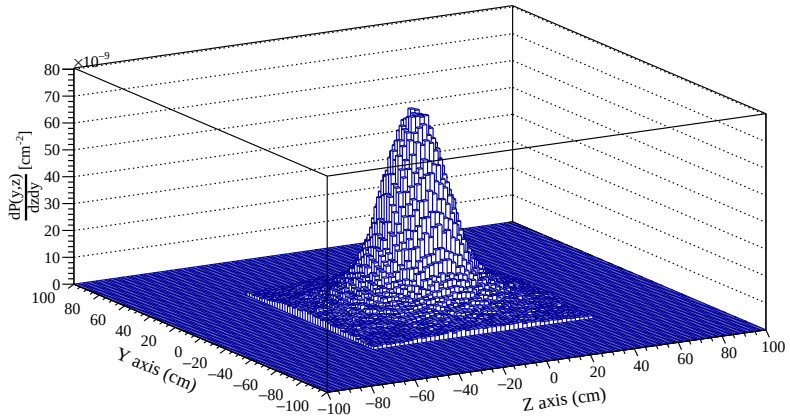


Figure 5.22: Gaussian beam profile of neutrons given in probability distribution across YZ plane at 5 cm away from the target for 30 MeV proton on beryllium (LEGO representation). Obtained with Geant4.



Figure 5.23: A neutron funnel that was used by IVMER in previous studies.

5.5 TALYS Results

For residual nuclei cross-section data for our experiment, there has been observed a gap around 22.4 MeV for reasons that remain unclear. In Figure 5.24, experimental cross-section evaluation of $^{7}\mathrm{Be}$ is given. The gap in TENDL (TALYS Evaluated Nuclear Data Library) data can be seen. The sharp fall does not exist in experimental data. As TALYS uses this data for activity calculations, the actual resulting activity may be less than the TALYS anticipates. This means that the rose rate that was calculated in Section 5.8 may actually be less in the experiment.

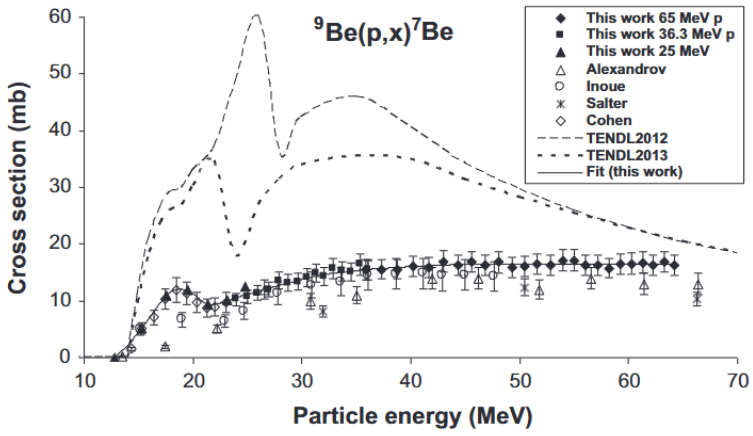


Figure 5.24: Comparison of experimental $^{9}\mathrm{Be}(p,x)^{7}\mathrm{Be}$ reaction cross-sections with TENDL-2012 and TENDL-2013 library between 13.4 and 70 MeV [35].

Table 5.4: Maximum isotope production rates, decay rates, activities, and yields for 30 MeV energy, 100 μA current proton beam. Obtained with TALYS.

Nuc.	**Prod. rate [s^{-1}]**	**Decay rate [s^{-1}]**	**Activity [GBq]**	**Yield [GBq/mAh]**
^{10}B	2.2×10^{-14}	-	-	-
^{9}B	1.3×10^{-11}	8.7×10^{17}	1.2×10^{3}	1.2×10^{5}
^{8}B	3.1×10^{-13}	9.0×10^{-1}	2.9×10^{1}	2.9×10^{3}
^{9}Be	1.9×10^{-11}	-	-	-
^{8}Be	5.4×10^{-11}	9.9×10^{15}	5.2×10^{3}	5.2×10^{5}
^{7}Be	8.0×10^{-12}	1.5×10^{-7}	4.1×10^{-1}	4.1×10^{0}
^{8}Li	5.7×10^{-13}	8.3×10^{-1}	5.4×10^{1}	5.4×10^{3}
^{7}Li	1.1×10^{-11}	-	-	-
^{6}Li	2.7×10^{-11}	-	-	-

5.6 Residual Nuclei Production and ^{7}Be

After irradiation, the high amount of long-lived radioactive isotopes would prohibit entrance to the R&D room and access to METU-DBL. To identify the isotropic inventory, TALYS and FLUKA were deployed to determine the produced isotopes, their corresponding production and decay rates, yields and post-irradiation activities. Among the isotopes given in Table 5.4 and Table 5.5, the residual nucleus with the highest half-life was found to be ^{7}Be with 53.3 days, which decays to ^{7}Li through electron capture channel ε, with 100% probability [16]. The decay scheme is given in Figure 5.25. This decay has 10.44 % probability of leaving ^{7}Li in the first excited state, and this state rapidly decays to ground state by emission of a 477.6 keV gamma ray. Some isotopes are stable, and the other produced unstable isotopes have rather short and minuscule half-lives, lasting milliseconds or even less. Hence, can be neglected. Residual nuclei and their corresponding attributes have been found using RESNUCLEI estimator in FLUKA. Irradiation beam profile with 1 hour of irradiation time and 100 μA (6.24×10^{14} p/s) proton current had been set. The DCYSCORE card was set to 0.0 cooling time, which just scores the activity just at the end of the

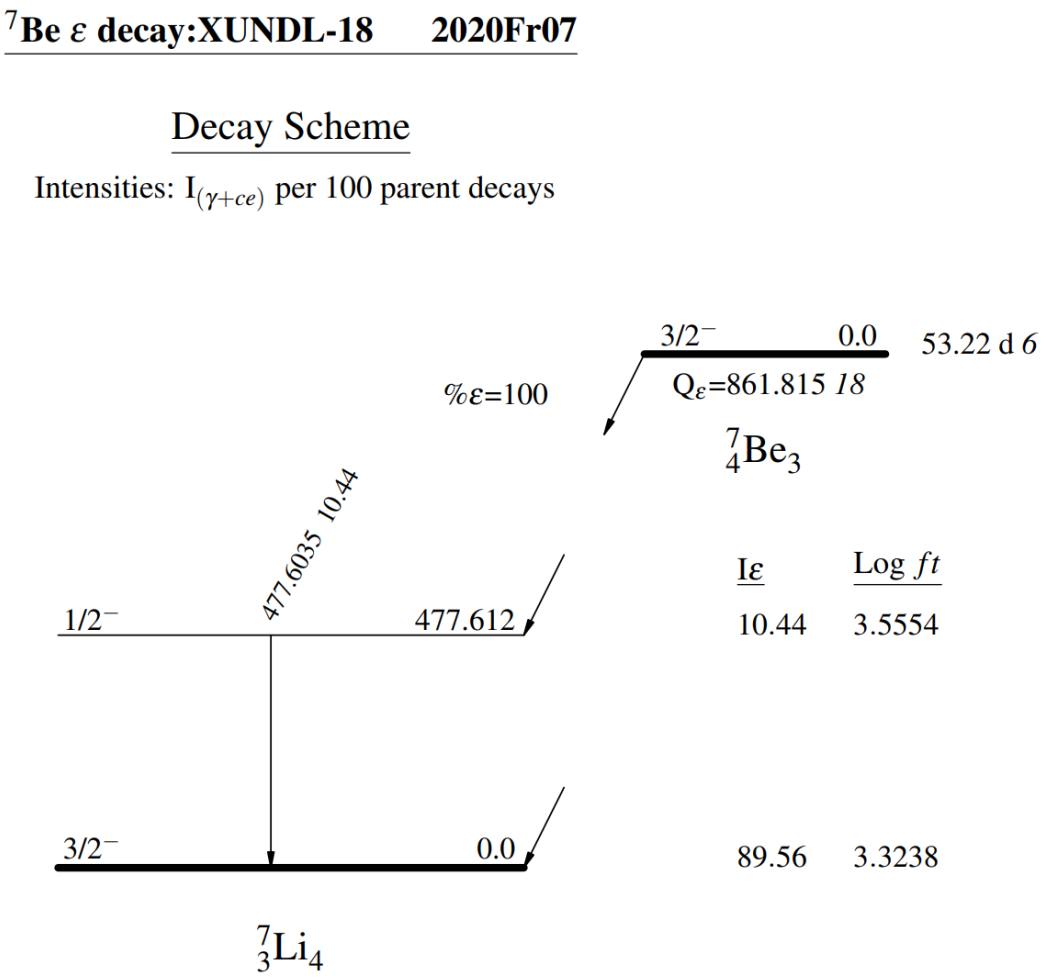


Figure 5.25: Decay scheme of ^{7}Be. Evaluated Nuclear Structure Data File (ENSDF) [26].

irradiation. The results are given in Table 5.5. In Table 5.6, the activities after 1 hour of cooling are given. Results indicate that after brief cooling times, only remaining nuclei are going to be ^{7}Be and tritium (^{3}H).

Half-life of tritium is 12.33 ± 0.02 years [50], which is relatively long. But it decays to ^{3}He through β^- decay $^{3}_{1}\mathrm{H} \rightarrow {}^{3}_{2}\mathrm{He} + e^- + \bar{\nu}_e$. This decay has mean electron energy $\bar{E} = 5.7$ keV, which results in limited penetration depth of only 6 mm in air [59]. Consequently due to the nature of low penetration of β radiation this aspect will not be incorporated into shielding calculations.

It has been found that around 22.4 MeV, cross-section experiences a sharp decrease,

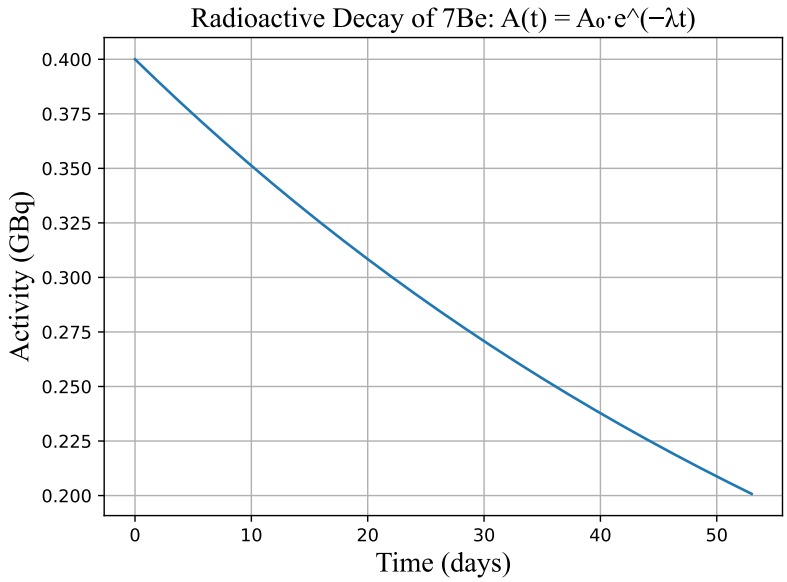


Figure 5.26: ^{7}Be Activity with respect to time. Time extends from beginning of the irradiation (1 hour of irradiation, 100 μA, 30 MeV) to 1 half-life. Obtained with TALYS.

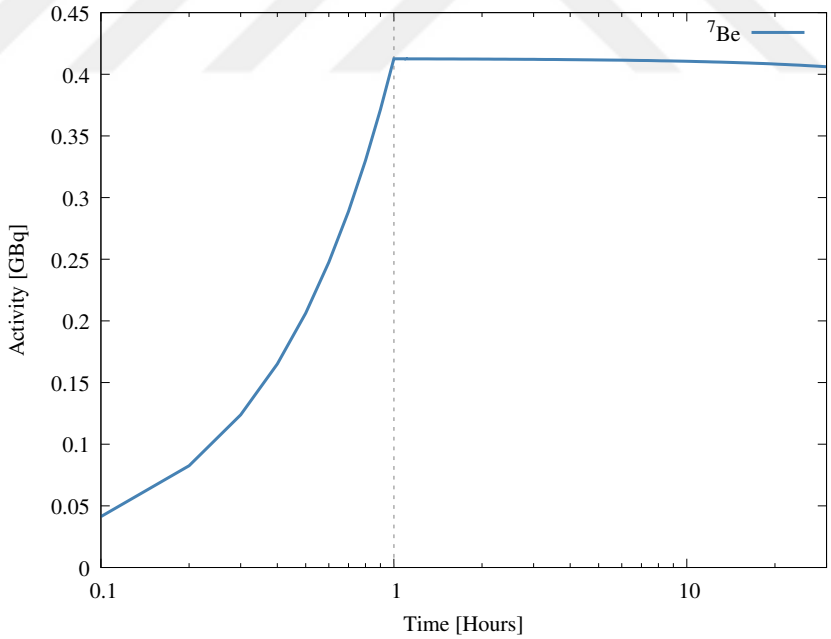


Figure 5.27: ^{7}Be Activity with respect to time. Time extends from beginning of the irradiation (1 hour of irradiation, 100 μA, 30 MeV) to total cooling time (1 week). Obtained with TALYS.

Table 5.5: Activities (Bq/cm^3 vs. A and Z Each cell: value (± uncertainty %). At the end of the irradiation. Obtained with FLUKA using RESNUCLEI.

$A\backslash Z$	**H**	**He**	**Li**	**Be**	**B**
10	-	-	-	5.33×10^{-1} (±5.2%)	-
9	-	-	9.24×10^{8} (±57.7%)	-	1.07×10^{12} (±0.3%)
8	-	-	5.05×10^{10} (±2.7%)	1.12×10^{12} (±0.4%)	2.77×10^{9} (±38.5%)
7	-	-	-	3.11×10^{8} (±2.3%)	-
6	-	2.40×10^{10} (±12.4%)	-	-	-
3	1.46×10^{7} (±0.9%)	-	-	-	-

and then moves up from that point with increasing proton energy.

Activation cross-section of $^{7}\mathrm{Be}$ is given in 5.28. Cross-sections of all the residual nuclei are given in Figure 5.29. Every other isotope except $^{7}\mathrm{Be}$ in Figure 5.29 has either short half-life or is stable. Lighter nuclei such as hydrogen and helium are not given in Figure 5.29. Similar to Figure 5.28, tritium production cross-section has also been found to be increasing with energy up until 22.4 MeV which is given in Figure 5.30.

5.7 Gamma Shielding Calculations for $^{7}\mathrm{Be}$

The dose rate inside the room will be dependent on the activity of $^{7}\mathrm{Be}$. To be able to safely enter the room after irradiation, shielding requirements need to be understood first. After calculating half-value and tenth-value layers, TALYS activity results will be investigated to predict the dose rate. By incorporating the activity and gamma

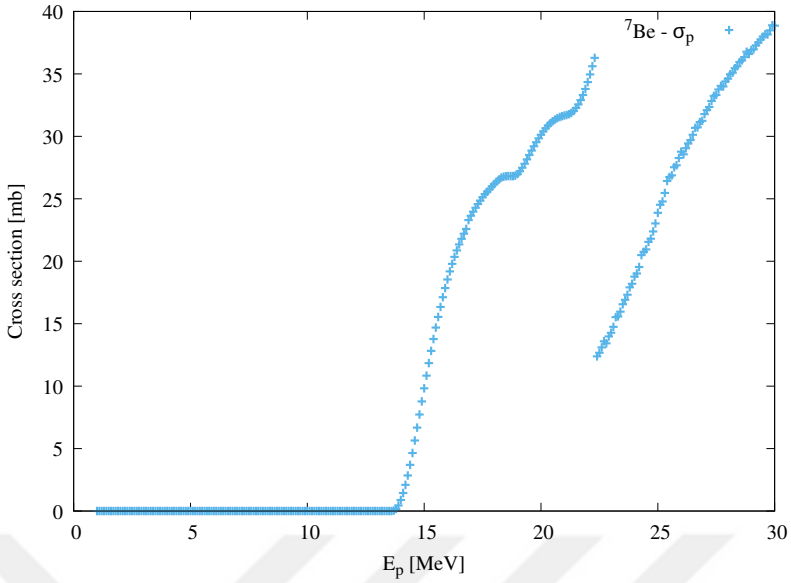


Figure 5.28: Production cross-section of ^{7}Be between 0-30 MeV. The reaction starts to take place after E_{th}:13.4 MeV. Obtained with TALYS.

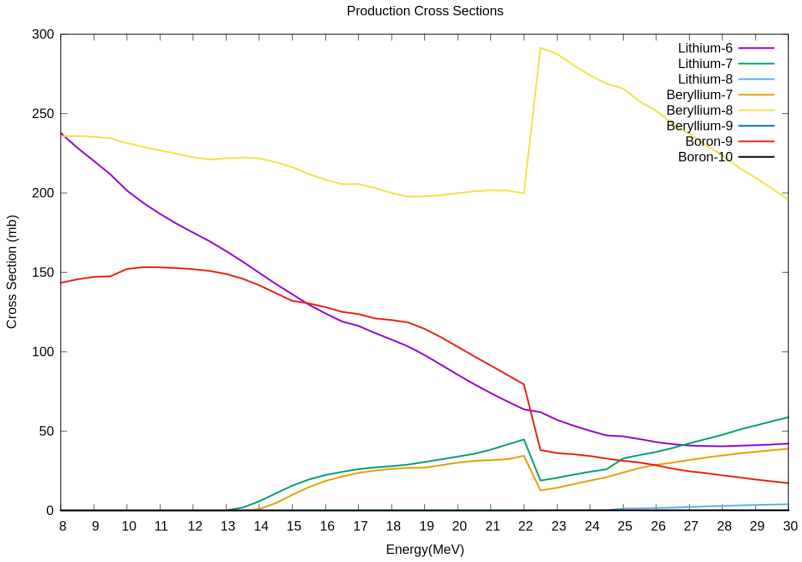


Figure 5.29: Production cross-sections of residual nuclei resulting from proton+beryllium reaction. Obtained with TALYS.

Table 5.6: Activities (Bq/cm^3 vs. A and Z Each cell: value (± uncertainty %). 1 hour cooling time. Obtained with FLUKA using RESNUCLEI.

$A\backslash Z$	**H**	**He**	**Li**	**Be**
10	-	-	-	5.33×10^{-1} (±5.2%)
7	-	-	-	3.11×10^{8} (±2.3%)
3	1.46×10^{7} (±0.9%)	-	-	-

emission energy values of ^{7}Be, shielding calculations were performed. The exponential attenuation law forms the fundamental basis for shielding calculations.

$$I(x) = I_0 \exp(-\mu x) \tag{5.4}$$

where I_0 is the initial value of intensity, μ is the linear attenuation coefficient, and x is the path length taken by the particle inside that volume. The gamma energy of ^{7}Be is 477 keV, and mass attenuation coefficient (μ/ρ) for lead at this value reads $\mu/\rho \approx 0.1614$ cm^2/g [64]. Using the density of lead $\rho = 11.34$ g/cm^3, μ_{eff} is given as:

$$\mu_{\text{eff}} = \frac{\mu}{\rho} \times \rho = 0.1614(\text{cm}^2/\text{g}) \times 11.34(\text{g/cm}^3) = 1.83\ \text{cm}^{-1} \tag{5.5}$$

For half-value and tenth-value calculations, this value will be used.

5.7.1 Half-Value and Tenth-Value Layers

Using this value, half-value layer (HVL) and tenth-value layer (TVL) can be calculated.

HVL

$$x_{1/2} = \frac{\ln 2}{\mu} \approx \frac{0.693}{1.83\,\text{cm}^{-1}} \approx 0.379\,\text{cm}\ (\approx 3.8\,\text{mm}). \tag{5.6}$$

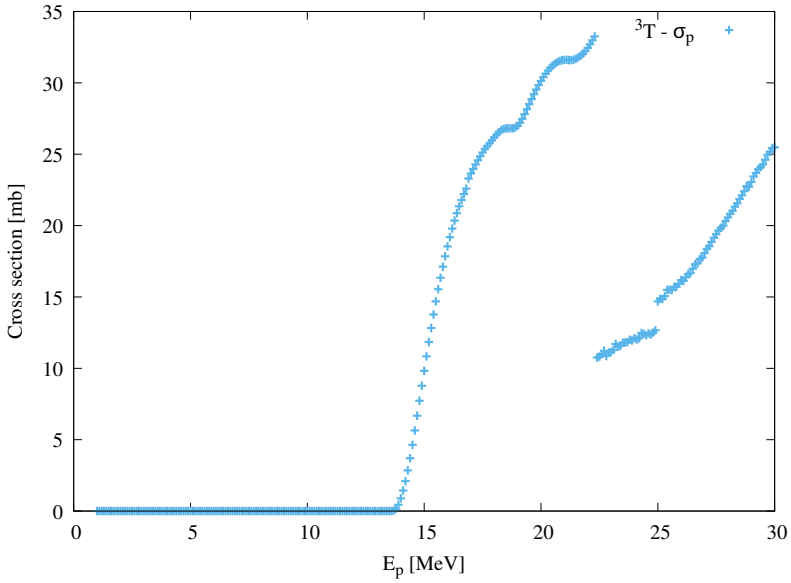


Figure 5.30: Production cross-section of tritium ^{3}T. Obtained with TALYS.

TVL

$$x_{1/10} = \frac{\ln 10}{\mu} \approx \frac{2.303}{1.83\,\text{cm}^{-1}} \approx 1.25\,\text{cm} \tag{5.7}$$

These imply that in order to decrease the gamma intensity by %50, one HVL (3.8 mm) is required. Reducing it by a factor of 100 would be 2 TVL, and for 1000, 3 TVL and so forth.

5.8 Dose Rate Inside the Room

Using the activity that we have obtained from TALYS, which is given in Figure 5.27, we can estimate the hourly dose rate due to ^{7}Be inside the room. The dose rate can be found from:

$$\dot{D} = \Gamma \cdot A \cdot \frac{1}{r^2} \tag{5.8}$$

Where Γ is the gamma constant for the ^{7}Be, r is the distance and A is the activity. The gamma constant for ^{7}Be is given as 9.3×10^{-6} mSv/h per MBq at 1.0 meter [70]. At the end of irradiation, Figure 5.27 reads 0.4 GBq activity.

$$1\ \text{GBq} = 1000\ \text{MBq}$$

$$\Gamma = 0.0093\ \mu\text{Sv/h/MBq} \times 1000 = \boxed{9.3\ \mu\text{Sv/h/GBq}}$$

$$\dot{D} = \Gamma \cdot A \cdot \frac{1}{r^2} = 9.3 \cdot 0.4 = \boxed{\sim 3.7\ \mu\text{Sv/h}}$$

This is the dose rate at 1.0 meter distance at the end of 1 hour of irradiation, with $100\mu A$ proton current with 30 MeV energy. To fall below the limit of 2μSv/h, 1 HVL would be sufficient. Encapsulating the target station with 0.38 cm lead bricks would decrease the dose rate to 1.85μSv/h. Using 1 TVL would decrease the dose to $0.37\ \mu$Sv/h.

5.9 Thermal Analysis

In the previous section, we have calculated the dose rate that is the result of high proton currents. We also need to anticipate how the target will hold up under high thermal loads due to high proton currents. Thermal analysis had been done by conducting joint work between various simulation kits. Initially, spectral fluence of proton beam's exit energy was plotted using FLUKA. In Figure 5.31 two target orientation angle were tested. A perpendicular target resulted in an energy drop of 11 MeV $(30 \rightarrow 19)$. This is the energy drop of a 3 mm target. A diagonal, 45° tilted target on the other hand, showed that most of the exiting protons resided around 14.5 MeV. The 15.5 MeV energy drop was then registered as *Eback* parameter in TALYS to see what thickness it corresponds to. It was found to be 4.43 mm, which was expected due to Equation 5.1. An energy drop of 15.5 MeV was then entered in the input of TALYS. In Table 5.7, the heat deposition in target with respect to different proton currents has been given. The highest tested current was 150 μA, which is currently the maximum allowed by METU-DBL Using these results, Fusion360 has been deployed to conduct steady state thermal analysis of the target system. Linear correlation between the deposited heat and proton current had been shown. It was seen that target orientation angle significantly changes proton exit energy.

In Figure 5.31, exit spectral fluence of 30 MeV protons were plotted using FLUKA. It has been shown that proton exit energy of a tilted target spans a larger area of energies than a perpendicular one, peaking at 14.5 MeV. The total power of the beam is calculated using the formula $P = E \times I$. Using the beryllium material properties given in Table 5.8, heat analysis were performed to assess whether the target was

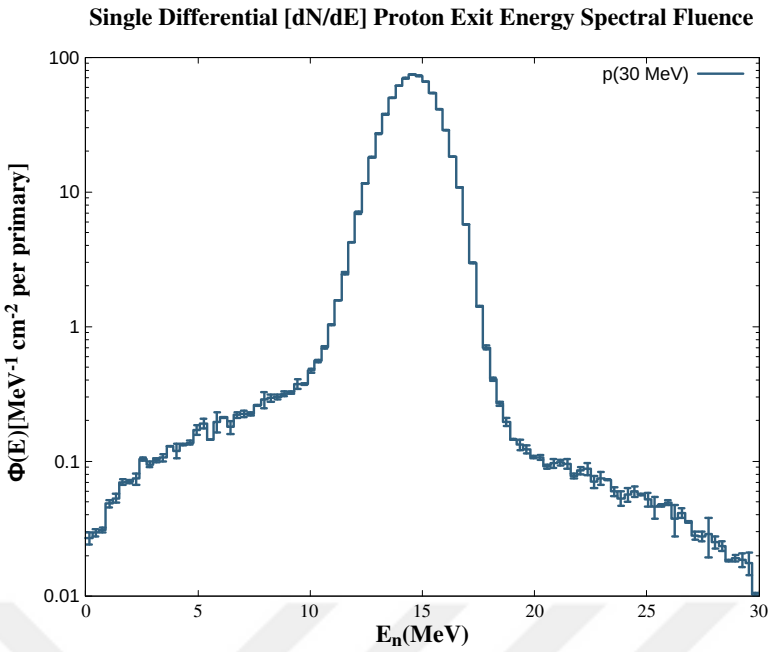


Figure 5.31: p(30) exit spectral fluence in 3 mm beryllium target. $45°$ target orientation. Obtained with FLUKA using USRBDX card.

capable of enduring the heat from the proton energy deposition.

Table 5.7: Power partition of 30 MeV proton beam with different proton currents given in both the beryllium target and the aluminum beam dump behind it.

Proton Current (μA)	**Target Heat Deposition [kW]**	**Aluminum Dump Heat Deposition [kW]**
150.0	1.8	2.7
100.0	1.2	1.8
50.0	0.6	0.9
1.0	0.012	0.018

5.9.1 Beryllium Material Properties

In nature, beryllium exists only in the form of $^{9}\mathrm{Be}$. Beryllium was defined in Fusion360 using the properties given in Table 5.8 for 99.9% pure $^{9}\mathrm{Be}$. Its high thermal conductivity and melting point favors its usage as target material.

Table 5.8: Mechanical properties of pure beryllium. [20]

Property	**Value**
Density	1.85 g/cm^3
Young's Modulus	276 – 303 GPa
Yield Strength	207 MPa (O-30)
	241 – 296 MPa (I-200)
Thermal Conductivity	220 W/m·K
Coefficient of Thermal Expansion	11.5 ppm/°C
Poisson's Ratio	0.08
Hardness	80 – 100 (Rockwell)
Melting Point	1287 °C

5.9.2 Thermal Loads and Cooling

Fusion360 requires thermal loads as input to conduct the thermal analysis. Four different loads were defined and material properties of beryllium given in Table 5.8 were entered.

Internal Heat: The heating caused by the proton beam inside the target was registered as an internal heat, due to its small volume of target.

Radiation: The heat exchange driven by electromagnetic waves was entered for all the faces in the setup. For a polished, smoothly cut beryllium and aluminum dump,

emissivity of $\epsilon = 0.1$ was registered.

Heat Source: Although the target is loaded with some portion of the heat, the rest of the proton power is going to dissipate inside the aluminum dump. To account for it, a heat source of $P_{\text{Proton}} - P_{\text{Target}}$ on the face of aluminum directly behind the target was registered.

Convection: This is the Neumann boundary condition. The turbulent liquid-water convection coefficient h of METU-DBL was assumed to be 6000 W$/(m^2.K)$ for a moderate water flow with the water temperature kept constant at 15°. The technical data sheet states the water pressure is at 4 bar with flow rate of 15 l/min.

The results of thermal simulation are given below. The results indicate that the existing liquid water cooling infrastructure of METU-DBL is sufficient for beryllium irradiation.

Table 5.9: Result Summary of Temperature, Heat Flux, and Thermal Gradient $150\mu A$ current, 30 MeV energy. Obtained with Fusion360.

Name	**Minimum**	**Maximum**
Temperature	93 °C	560 °C
Heat Flux		
Total	1×10^{-4} W/mm^2	7 W/mm^2
X	-4 W/mm^2	4 W/mm^2
Y	-4 W/mm^2	5 W/mm^2
Z	-7 W/mm^2	1 W/mm^2
Thermal Gradient		
Total	5×10^{-4} °C/mm	37 °C/mm
X	-19 °C/mm	17 °C/mm
Y	-20 °C/mm	17 °C/mm
Z	-3 °C/mm	35 °C/mm

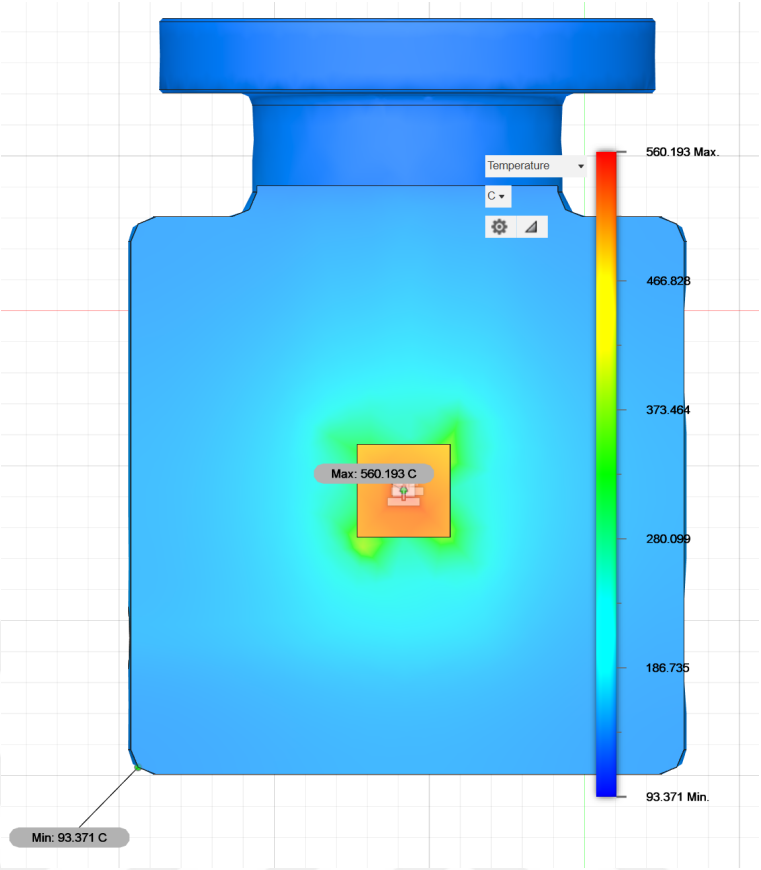


Figure 5.32: Thermal analysis result of 150μA proton current, 30 MeV energy. Obtained with Fusion360.

In Table 5.9 and Figure 5.32, the thermal analysis results of 30 MeV energy, 150μA current proton beam are given. Along the respective coordinates, minimum and maximum values are taken at distinct nodes inside the setup. The sum of the minimum or the maximum of each of the individual coordinates does not necessarily equal to the total. They are not simply arithmetic sums of the components, but are rather vector magnitudes. The maximum temperature reads 560.2 °C, which is below the melting point of beryllium, 1283 °C.

5.10 Ionization and Target Damage Caused by Lattice Displacement-SRIM/TRIM Results

SRIM (The stopping and range of ions in matter) [80] was deployed to predict the ionization and atomic displacement from their lattice positions. Both the target damage and ionization are plotted in 3D. In Figure 5.33, the number of displaced atoms is quantified, which signifies the extent of target damage. The displacement has been found as minimal, as indicated by 21 atoms per proton. Equivalency of vacancies to displacements indicate that no recombination takes place.

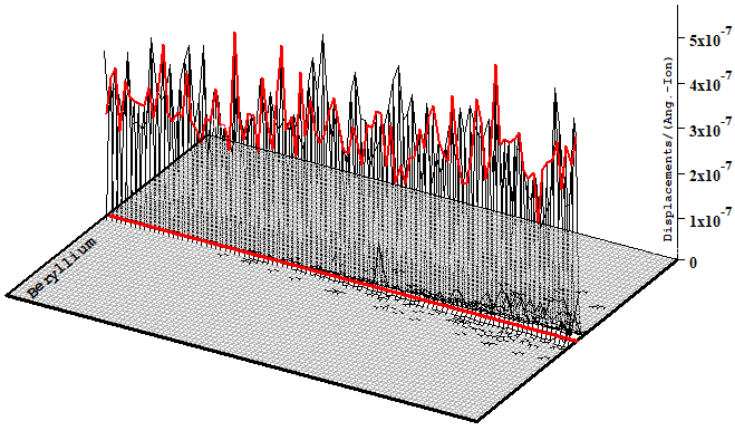


Figure 5.33: Lattice displacement per proton inside beryllium target. Obtained with SRIM.

In Figure 5.34, ionization inside the target is given. Y-axis represents the local ionization energy deposition per depth step. It is seen that almost all the proton energy is lost through electronic stopping. Homogenous distribution along the beam path suggest ionization rate is almost constant throughout the passage. Phonon production rate with 5.0 keV/proton indicates lattice vibrations are low. The total target damage value of 0.19 keV/proton shows that very little proton energy goes into permanent

damage. This value should be interpreted together with lattice displacement rate of 21 atoms per proton. They indicate that the low average target damage value (available energy to knock off atoms) falls behind the displacement threshold energy for beryllium. Therefore, during proton irradiation of a beryllium target, the target will preserve its integrity. In both of the figures, the proton beam enters from the left.

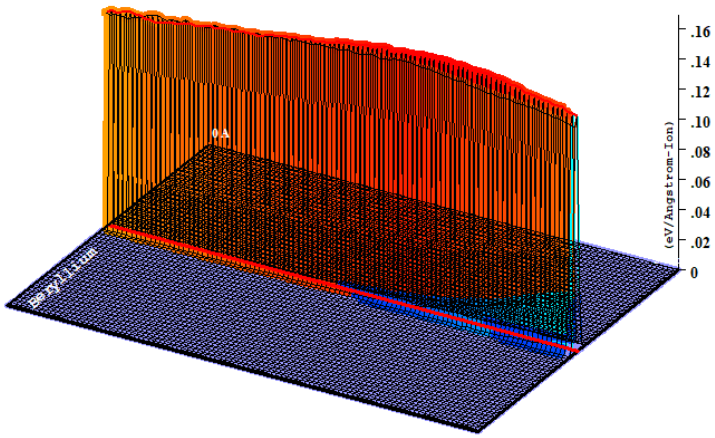


Figure 5.34: Ionization given in energy per proton inside beryllium target. Obtained with SRIM.

CHAPTER 6

CONCLUSION

This thesis studied the feasibility of cyclotron based proton-beryllium reaction for neutron production purposes. By deploying Monte-Carlo simulation tool kits and various other software methods, a comprehensive study has been conducted to prepare a manual for both IVMER and those who wish to construct a solid beryllium based neutron source.

By optimizing irradiation parameters such as target orientation and volume, geometrical setup, proton beam energy and heat flux, this thesis aimed to increase the overall neutron yield while keeping the residual nuclei activity minimal to ensure regular IVMER operations can continue to take place short after beryllium irradiation.

Results indicate that proton accelerator based beryllium target systems can act as a viable source of neutrons, reaching neutron fluxes of up to $\sim 3 \times 10^{10}$ n/cm^2/s (integrated over solid angle) at the surface of the proposed setup for METU-DBL operating at high currents ($150\mu A$). At these currents, beryllium reaches a maximum temperature of 560 °C, which is well below its melting point of 1287°C. Low gamma energy of $^{7}\mathrm{Be}$ decreases the thickness of the lead shielding needed to keep the irradiation room radiation dose under safe limits. Using attenuation formula, HVL and TVL were found to be 3.8 mm and 1.25 cm respectively. The dose rate at 1.0 meter away at the end of 1-hour irradiation period was found to be 3.7 μSv/h.

The resulting energy spectrum of the neutron field spans a large area, starting from epithermal neutrons up to the fast and relativistic band. Using low density neutron moderators such as polyethylene, the low energy end point can further be reduced down to the thermal energy band.

High thermal conductivity of beryllium, the low gamma-ray energy characteristic of its produced, long-lived residual nucleus $^{7}\mathrm{Be}$, modifiable nature of cyclotron energy and proton current, and hence the produced neutron spectrum, are all prevailing reasons to utilize beryllium as a neutron source as opposed to other proposed neutron producing channels, which were also mentioned in the literature review. Their advantages and disadvantages were also given, the choice was ultimately dependent on the existing setup.

Using this work as a ground-basis, METU-DBL can be upgraded to provide neutron irradiation test services. The thesis presents thorough work to provide a guide on the effects of irradiation parameters on the produced neutron energy spectrum, its fluence, its resulting ionizing dose and the activity of the residual nuclei. By proposing to make the whole irradiation setup modifiable, the user or the client may adjust the neutron energy and fluence by adding various blocks of neutron moderating materials at the exiting wall of the proposed station. By doing so, several neutronic research fields and applications will be an open possibility within IVMER.

REFERENCES

[1]M. Al-Abyad et al. “Experimental yield and evaluation of proton induced reactions for neutron production and synthesis of beryllium-7 using lithium compounds as target material”. In: *Applied Radiation and Isotopes* 155 (2020), p. 108947. ISSN: 0969-8043. DOI: https://doi.org/10.1016/j.apradiso.2019.108947. URL: https://www.sciencedirect.com/science/article/pii/S0969804319300661.

[2]S. Agostinelli et al. “Geant4—a simulation toolkit”. In: *Nuclear Instruments and Methods in Physics Research Section A: Accelerators, Spectrometers, Detectors and Associated Equipment* 506.3 (2003), pp. 250–303. ISSN: 0168-9002. DOI: https://doi.org/10.1016/S0168-9002(03)01368-8. URL: https://www.sciencedirect.com/science/article/pii/S0168900203013688.

[3]C. Ahdida et al. “New Capabilities of the FLUKA Multi-Purpose Code”. In: *Front. Phys.* 9 (2022), p. 788253. DOI: 10.3389/fphy.2021.788253. URL: https://cds.cern.ch/record/2806210.

[4]A. Alhussain and A. Abuhoza. “Comparison Study of Reflected and Transmitted Thermal Neutron Flux in Water And Other Moderators.” In: (Jan. 2009).

[5]J. Allison et al. “Geant4 developments and applications”. In: *IEEE Transactions on Nuclear Science* 53.1 (2006), pp. 270–278. DOI: 10.1109/TNS.2006.869826.

[6]S. S. Alrwashdeh et al. “Neutron radiographic in operando investigation of water transport in polymer electrolyte membrane fuel cells with channel barriers”. In: *Energy Conversion and Management* 148 (2017), pp. 604–610.

[7]V. Astrelin et al. “Blistering of the selected materials irradiated by intense 200 keV proton beam”. In: *Journal of Nuclear Materials* 396.1 (2010), pp. 43–48.

[8]F. Ballarini et al. “The FLUKA code: Overview and new developments”. In: *EPJ Nuclear Sciences & Technologies* 10 (2024), p. 16.

[9]R. C. Baumann. “Radiation-induced soft errors in advanced semiconductor technologies”. In: *IEEE Transactions on Device and materials reliability* 5.3 (2005), pp. 305–316.

[10]K. H. Beckurts. *Neutron Physics, By KH Beckurts and K. Wirtz. Translated by L. Dresner*. Springer-Verlag, 1964.

[11]H. Bethe and J. Ashkin. “Experimental Nuclear Physics”. In: *Experimental Nuclear Physics*. Ed. by E. Segrè. New York: J. Wiley, 1953, p. 253.

[12]C. M. Bishop. *Pattern Recognition and Machine Learning*. Section 11.4: Slice sampling. Springer, 2006. ISBN: 978-0-387-31073-2.

[13]W. Bothe and H. Becker. “Künstliche Erregung von Kern-?-Strahlen”. In: *Zeitschrift für Physik* 66.5–6 (May 1930), pp. 289–306. ISSN: 1434-601X. DOI: 10.1007/bf01390908. URL: http://dx.doi.org/10.1007/BF01390908.

[14]L. L. Carter and E. D. Cashwell. *Particle-Transport Simulation with the Monte Carlo Method*. Los Alamos Scientific Laboratory: Technical Information Center, Energy Research and Development Administration, 1975, pp. 1–25.

[15]G. Casella, C. P. Robert, and Martin T. Wells. “Generalized Accept-Reject Sampling Schemes”. In: *Institute of Mathematical Statistics Collections*. 2004, pp. 342–347. ISBN: 9780940600614. DOI: 10.1214/lnms/1196285403.

[16]M. Chaussidon, François R., and Kevin D McKeegan. “Li and B isotopic variations in an Allende CAI: Evidence for the in situ decay of short-lived 10Be and for the possible presence of the short-lived nuclide 7Be in the early solar system”. In: *Geochimica et Cosmochimica Acta* 70.1 (2006), pp. 224–245.

[17]D. L. Chichester. “Production and applications of neutrons using particle accelerators”. In: *Industrial Accelerators and Their Applications*. World Scientific, 2012, pp. 243–305.

[18]L. Ciani and M. Catelani. “A fault tolerant architecture to avoid the effects of Single Event Upset (SEU) in avionics applications”. In: *Measurement* 54 (2014), pp. 256–263.

[19]S. Cierjacks. “Neutron sources for basic physics and applications”. In: *OECD/NEA Rep.* 81 (1983).

[20]L. Coyle. “Beryllium: Properties and Applications”. In: *University of Arizona. November* 292010 (2010).

[21]*Current Status of Neutron Capture Therapy*. TECDOC Series 1223. Vienna: INTERNATIONAL ATOMIC ENERGY AGENCY, 2001. URL: https://www.iaea.org/publications/6168/current-status-of-neutron-capture-therapy.

[22]I. A. D'Souza and C. S. Kalman. *Preons: Models of Leptons, Quarks and Gauge Bosons as Composite Objects*. World Scientific, 1992. ISBN: 978-981-02-1019-9.

[23]C. Domingo et al. "Usage of a corrected Bethe–Bloch formula for charge identification of fast ions with Z>30 recorded in polycarbonate track detectors". In: *Nuclear Instruments and Methods in Physics Research Section B: Beam Interactions with Materials and Atoms* 146.1 (1998), pp. 114–119. ISSN: 0168-583X. DOI: https://doi.org/10.1016/S0168-583X(98)00489-3. URL: https://www.sciencedirect.com/science/article/pii/S0168583X98004893.

[24]Encyclopædia Britannica. *James Chadwick*. Image, accessed 7 July 2025. 2025.

[25]B.M. Fisher et al. "Detecting the radiative decay mode of the neutron". In: *Journal of Research of the National Institute of Standards and Technology* 110.4 (2005), p. 421.

[26]S. Fretwell et al. "Direct Measurement of the $^{7}\mathrm{Be}$ L/K Capture Ratio in Ta-Based Superconducting Tunnel Junctions". In: *Phys. Rev. Lett.* 125 (3 July 2020), p. 032701. DOI: 10.1103/PhysRevLett.125.032701. URL: https://link.aps.org/doi/10.1103/PhysRevLett.125.032701.

[27]Frontier Technology Corporation. *Complete Guide to Californium*. https://frontier-cf252.com/blog/complete-guide-californium/. Accessed: 2025-07-12. 2023. URL: https://frontier-cf252.com/blog/complete-guide-californium/.

[28]G. Gamow. "Mass defect curve and nuclear constitution". In: *Proceedings of the Royal Society of London. Series A, Containing Papers of a Mathematical and Physical Character* 126.803 (1930), pp. 632–644.

[29]S. L. Glashow. "Partial-symmetries of weak interactions". In: *Nuclear physics* 22.4 (1961), pp. 579–588.

[30]P. Goldhagen. "Cosmic-ray neutrons on the ground and in the atmosphere". In: *MRS bulletin* 28.2 (2003), pp. 131–135.

[31]M.S. Gordon et al. “Measurement of the flux and energy spectrum of cosmic-ray induced neutrons on the ground”. In: *IEEE Transactions on Nuclear Science* 51.6 (2004), pp. 3427–3434.

[32]O. Hahn and F. Strassmann. “Uber den Nachweis und das Verhalten der bei der Bestrahlung des Urans mittels Neutronen entstehenden Erdalkalimetalle”. In: *Die Naturwissenschaften* 27.1 (Jan. 1939), pp. 11–15. ISSN: 1432-1904. DOI: 10.1007/bf01488241. URL: http://dx.doi.org/10.1007/BF01488241.

[33]F. Halzen and A. D. Martin. *Quarks and Leptons: An Introductory Course in Modern Particle Physics*. New York: John Wiley & Sons, 1984.

[34]M. R. Hawkesworth. *Neutron radiography. Equipment and methods*. Jan. 1977.

[35]A. Hermanne, F. Tarkanyi, and Sandor T. “Activation cross sections for production of 7Be by proton and deuteron induced reactions on 9Be: Protons up to 65 MeV and deuterons up to 50 MeV”. In: *Applied Radiation and Isotopes* 90 (2014), pp. 203–207.

[36]WB Howard et al. “Measurement of the thick-target 9Be (p, n) neutron energy spectra”. In: *Nuclear science and engineering* 138.2 (2001), pp. 145–160.

[37]E. Hussein, P. Eng, and E. Hussein. “Monte carlo particle transport with the mcnp code”. In: *URL https://canteach. candu. org/Content% 20Library/20043514. pdf* (1997).

[38]International Atomic Energy Agency. *Cyclotron Produced Radionuclides: Guidance on Facility Design and Production of [18F]Fluorodeoxyglucose (FDG)*. Accessed: 2024-08-23. International Atomic Energy Agency. 2019. URL: https://www-pub.iaea.org/MTCD/Publications/PDF/P1743_web.pdf.

[39]F. James. “Monte Carlo theory and practice”. In: *Reports on Progress in Physics* 43.9 (Sept. 1980), p. 1145. DOI: 10.1088/0034-4885/43/9/002. URL: https://dx.doi.org/10.1088/0034-4885/43/9/002.

[40]B. Jeon et al. “Target-Moderator-Reflector system for 10–30áMeV proton accelerator-driven compact thermal neutron source: Conceptual design and neutronic characterization”. In: *Nuclear Engineering and Technology* 52.3 (2020), pp. 633–646.

[41]I. Joliot-Curie and F. Joliot. “Émission de protons de grande vitesse par les substances hydrogénées sous l’influence des rayons gamma très pénétrants”. French. In: *Comptes Rendus des Séances de l’Académie des Sciences* 194 (1932), p. 273.

[42]E. Karadöller et al. “METU-DBL: a cost effective proton irradiation facility”. In: *Journal of Instrumentation* 18.06 (2023), T06010.

[43]A. Kennedy et al. “Safety of selective internal radiation therapy (SIRT) with yttrium-90 microspheres combined with systemic anticancer agents: expert consensus”. In: *Journal of Gastrointestinal Oncology* 8.6 (Dec. 2017), pp. 1079–1099. DOI: 10.21037/jgo.2017.09.10.

[44]A. Koning, S. Hilaire, and S. Goriely. “TALYS: modeling of nuclear reactions”. In: *The European Physical Journal A* 59.6 (June 2023). ISSN: 1434-601X. DOI: 10.1140/epja/s10050-023-01034-3. URL: http://dx.doi.org/10.1140/epja/s10050-023-01034-3.

[45]K. S. Krane. *Introductory nuclear physics*. New York, NY: Wiley, 1988, p. 394.

[46]T. Kulikowska. “An introduction to the neutron transport Phenomena”. In: (2000).

[47]Kurzon. *The geometry of Rutherford’s scattering formula*. Online image. Own work, licensed under CC BY 4.0. 2023.

[48]W. R. Leo. *Techniques for Nuclear and Particle Physics Experiments: A How-to Approach*. 2nd. Springer, 1994. ISBN: 978-3-642-57920-2. DOI: 10.1007/978-3-642-57920-2.

[49]M. Lone et al. “Thick target neutron yields and spectral distributions from the 7Li (pd, n) and 9Be (pd, n) reactions”. In: *Nuclear instruments and methods* 143.2 (1977), pp. 331–344.

[50]L. L. Lucas and M. P. Unterweger. “Comprehensive review and critical evaluation of the half-life of tritium”. In: *Journal of research of the National Institute of Standards and Technology* 105.4 (2000), p. 541.

[51]S. S. Malik and I. Mazumdar. “Role of quantum phase transition in spontaneous fission”. In: *Nuclear Physics A* 990 (2019), pp. 220–243.

[52]R.C. Martin, JB Knauer, and PA Balo. “Production, distribution and applications of californium-252 neutron sources”. In: *Applied Radiation and Isotopes* 53.4-5 (2000), pp. 785–792.

[53]A. J. McNeil, Rüdiger Frey, and Paul Embrechts. *Quantitative Risk Management*. Princeton Series in Finance. Princeton, NJ: Princeton University Press, 2005, p. 186. ISBN: 0-691-12255-5.

[54]N. Metropolis and S. Ulam. "The Monte Carlo Method". In: *Journal of the American Statistical Association* 44.247 (1949), pp. 335–341. DOI: 10.2307/2280232.

[55]T. Mitsumoto et al. "Cyclotron-based neutron source for BNCT". In: *AIP Conference Proceedings*. Vol. 1525. 1. American Institute of Physics. 2013, pp. 319–322.

[56]B. Muçogllava, S. U. Duran, and M. B. Demirköz and. "An Anisotropic Neutron Collimating System for Proton Accelerator-Generated Secondary Particles". In: *Nuclear Technology* 0.0 (2025), pp. 1–10. DOI: 10.1080/00295450.2025.2461428. eprint: https://doi.org/10.1080/00295450.2025.2461428. URL: https://doi.org/10.1080/00295450.2025.2461428.

[57]R. M. Neal. "Slice Sampling". In: *Annals of Statistics* 31.3 (2003), pp. 705–767. DOI: 10.1214/aos/1056562461.

[58]D. D. Nolte. "The tangled tale of phase space". In: *Physics Today* 63.4 (Apr. 2010), pp. 33–38. ISSN: 1945-0699. DOI: 10.1063/1.3397041. URL: http://dx.doi.org/10.1063/1.3397041.

[59]North Carolina Health Physics Society. *3H Nuclide Safety Data Sheet: Hydrogen-3 [Tritium]*. http://www.nchps.org. Accessed from www.nchps.org. 2025.

[60]M. Ragheb. *Mathematical Formulation of Particle Transport in Monte Carlo Theory*. https://mragheb.com. Lecture notes, Chapter 19, University of Illinois at Urbana-Champaign. Oct. 2013.

[61]B.B. Venkatapathi Raju and S Jnanananda. "Fast neutron spectrum of Ra-Be source". In: *Nuclear Instruments and Methods* 31.1 (1964), pp. 87–89.

[62]J. Ranft. "Estimation of radiation problems around high-energy accelerators using calculations of the hadronic cascade in matter". In: *Particle Accelerators* 3 (1972), pp. 129–161.

[63]E. Ressouche. “Reminder: Magnetic structures description and determination by neutron diffraction”. In: *École thématique de la Société Française de la Neutronique* 13 (2014), p. 02001.

[64]S. Seltzer. *Tables of X-Ray Mass Attenuation Coefficients and Mass Energy-Absorption Coefficients, NIST Standard Reference Database 126*. en. 1995. DOI: 10.18434/T4D01F. URL: http://www.nist.gov/pml/data/xraycoef/index.cfm.

[65]M. Sisti. “Neutron activation analysis”. In: *Università and INFN Milano Bicocca. Low radioactivity techniques 2019 workshop*. 2019, pp. 20–23.

[66]G. L. Squires. *Practical Physics*. Cambridge University Press, Aug. 2001. ISBN: 9781139164498. DOI: 10.1017/cbo9781139164498. URL: http://dx.doi.org/10.1017/CBO9781139164498.

[67]M. Stefanik et al. “Neutron field of accelerator-driven p (35 MeV)+ Be fast neutron source at NPI Rez”. In: *EPJ Web of Conferences*. Vol. 146. EDP Sciences. 2017, p. 03011.

[68]M. Stefanik et al. “Neutron spectrum determination of p+ Be reaction for 30 MeV protons using the multi-foil activation technique”. In: *EPJ web of conferences*. Vol. 239. EDP Sciences. 2020, p. 17015.

[69]M. Strassler. *Protons and Neutrons*. https://profmattstrassler.com/articles-and-posts/particle-physics-basics/the-structure-of-matter/protons-and-neutrons/. Figure on page, Accessed: 2024-08-29. 2024.

[70]L. M. Unger and DK Trubey. *Specific gamma-ray dose constants for nuclides important to dosimetry and radiological assessment*. Tech. rep. Oak Ridge National Lab.(ORNL), Oak Ridge, TN (United States), 1982.

[71]C. Vega, O. Martinez, et al. “Neutron spectra and dosimetric features of isotopic neutron sources: a review”. In: (2015).

[72]V. Vlachoudis. “FLAIR: A Powerful But User Friendly Graphical Interface For FLUKA”. In: *Proc. Int. Conf. on Mathematics, Computational Methods & Reactor Physics (M&C 2009)*. Saratoga Springs, New York, 2009.

[73]H. Von Halban. “Preuve expérimentale de la diffraction des neutrons”. In: *Acad. Sci. Paris* 203 (1936), pp. 73–75.

[74]S. Weinberg. “A model of leptons”. In: *Physical review letters* 19.21 (1967), p. 1264.

[75]R. L. Workman and Particle Data Group. “Review of Particle Physics”. In: *Progress of Theoretical and Experimental Physics* 2022.8 (2022), p. 083C01. DOI: 10.1093/ptep/ptac097.

[76]Y. Yamagata et al. “Development of a neutron generating target for compact neutron sources using low energy proton beams”. In: *Journal of Radioanalytical and Nuclear Chemistry* 305 (2015), pp. 787–794.

[77]Z. Yamani, Z Tun, and DH Ryan. “Neutron scattering study of the classical antiferromagnet MnF2: a perfect hands-on neutron scattering teaching course”. In: *Canadian Journal of Physics* 88.10 (2010), pp. 771–797.

[78]M. Yiğitoğlu. “Radiation Environment Predictions for the IMECE satellite and G4BEAMLINE Simulations for the METU-DBL Project”. MA thesis. Middle East Technical University (Turkey), 2017.

[79]L. Zhang et al. “Differential die-away technology applied to detect special nuclear materials”. In: *Nuclear Engineering and Technology* 55.7 (2023), pp. 2483–2488.

[80]J. F. Ziegler, M.D. Ziegler, and J.P. Biersack. “SRIM – The stopping and range of ions in matter (2010)”. In: *Nuclear Instruments and Methods in Physics Research Section B: Beam Interactions with Materials and Atoms* 268.11 (2010). 19th International Conference on Ion Beam Analysis, pp. 1818–1823. ISSN: 0168-583X. DOI: https://doi.org/10.1016/j.nimb.2010.02.091. URL: https://www.sciencedirect.com/science/article/pii/S0168583X10001862.

Appendix A

APPENDIX

Thermal analysis for various proton currents are given below.

A.1 30 MeV Energy, 100μA Proton Current.

Table A.1: Result Summary of Temperature, Heat Flux, and Thermal Gradient. $100\mu A$. Obtained with Fusion360.

Name	**Minimum**	**Maximum**
Temperature	67 °C	367 °C
Heat Flux		
Total	8×10^{-5} W/mm^2	5 W/mm^2
X	-2 W/mm^2	3 W/mm^2
Y	-2 W/mm^2	3 W/mm^2
Z	-4 W/mm^2	0 W/mm^2
Thermal Gradient		
Total	3×10^{-4} °C/mm	23 °C/mm
X	-12 °C/mm	11 °C/mm
Y	-13 °C/mm	11 °C/mm
Z	-1 °C/mm	22 °C/mm

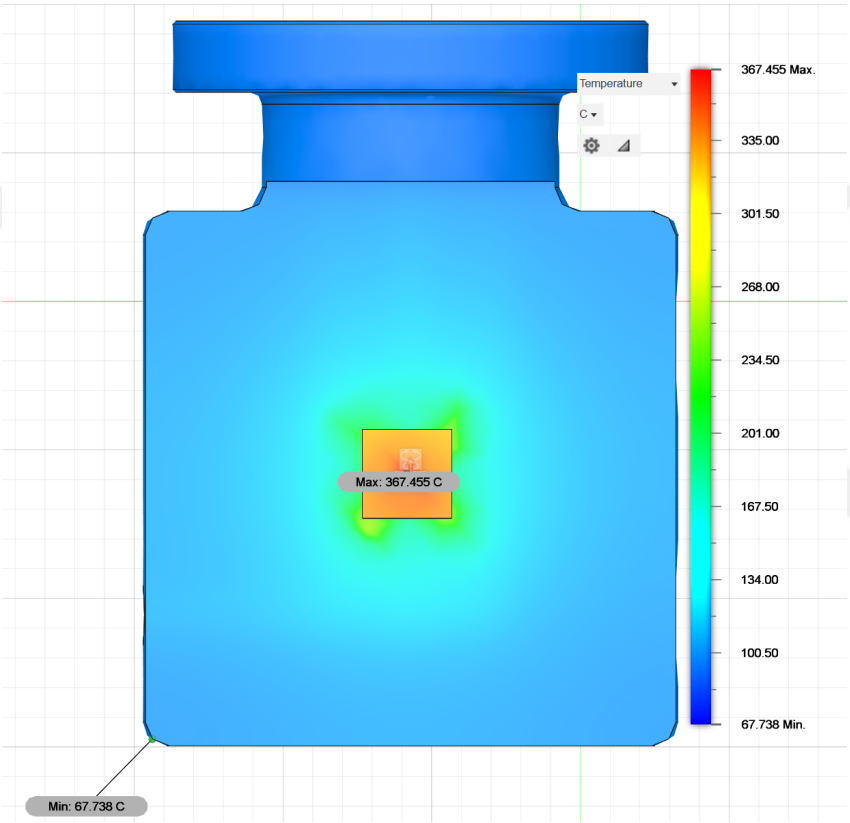


Figure A.1: $100\mu A$ proton current with 30 MeV kinetic energy.

A.2 30 MeV Energy, 50μA Proton Current.

Table A.2: Result Summary of Temperature, Heat Flux, and Thermal Gradient. 50μA. Obtained with Fusion360.

Name	**Minimum**	**Maximum**
Temperature	41 °C	197 °C
Heat Flux		
Total	3.9×10^{-5} W/mm^2	2 W/mm^2
X	-1.3 W/mm^2	2 W/mm^2
Y	-1.3 W/mm^2	2 W/mm^2
Z	-2.3 W/mm^2	0 W/mm^2
Thermal Gradient		
Total	1.7×10^{-4} °C/mm	12 °C/mm
X	-6.3 °C/mm	5 °C/mm
Y	-6.8 °C/mm	6 °C/mm
Z	-1.0 °C/mm	12 °C/mm

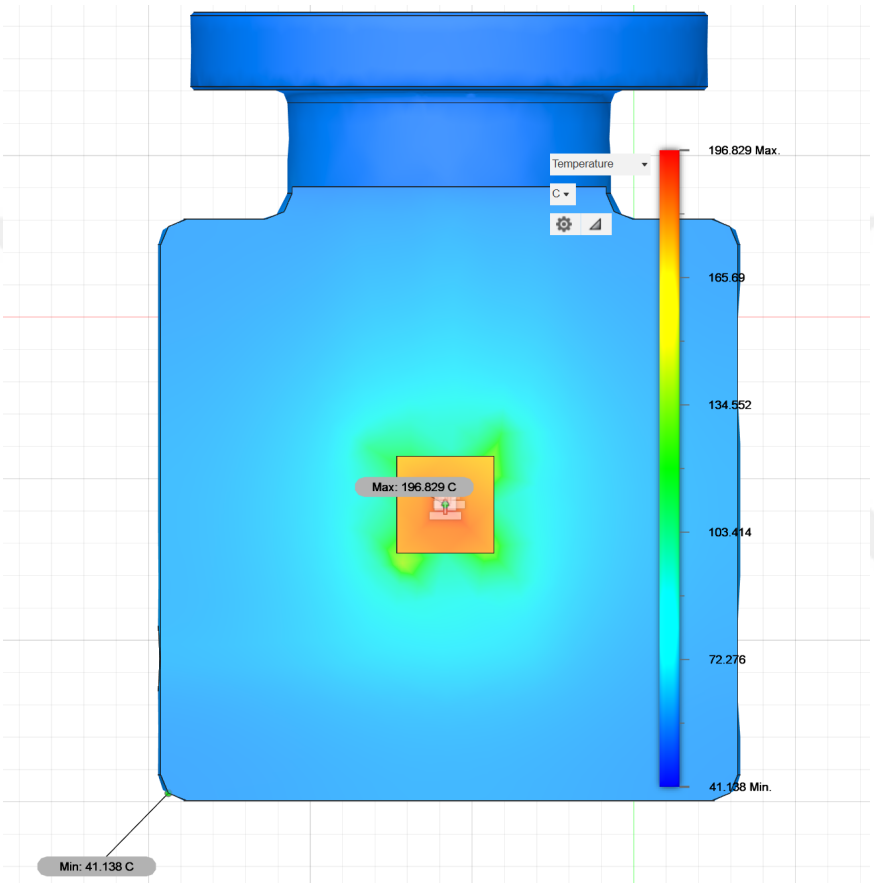


Figure A.2: $50\mu A$ proton current with 30 MeV kinetic energy.

A.3 30 MeV Energy, 1μA Proton Current.

Table A.3: Result Summary of Temperature, Heat Flux, and Thermal Gradient $1\mu A$. Obtained with Fusion360.

Name	**Minimum**	**Maximum**
Temperature	15 °C	19 °C
Heat Flux		
Total	4×10^{-7} W/mm^2	0 W/mm^2
X	0 W/mm^2	0 W/mm^2
Y	0 W/mm^2	0 W/mm^2
Z	0 W/mm^2	0 W/mm^2
Thermal Gradient		
Total	2×10^{-6} °C/mm	0.2 °C/mm
X	0 °C/mm	0 °C/mm
Y	0 °C/mm	0 °C/mm
Z	0 °C/mm	0 °C/mm

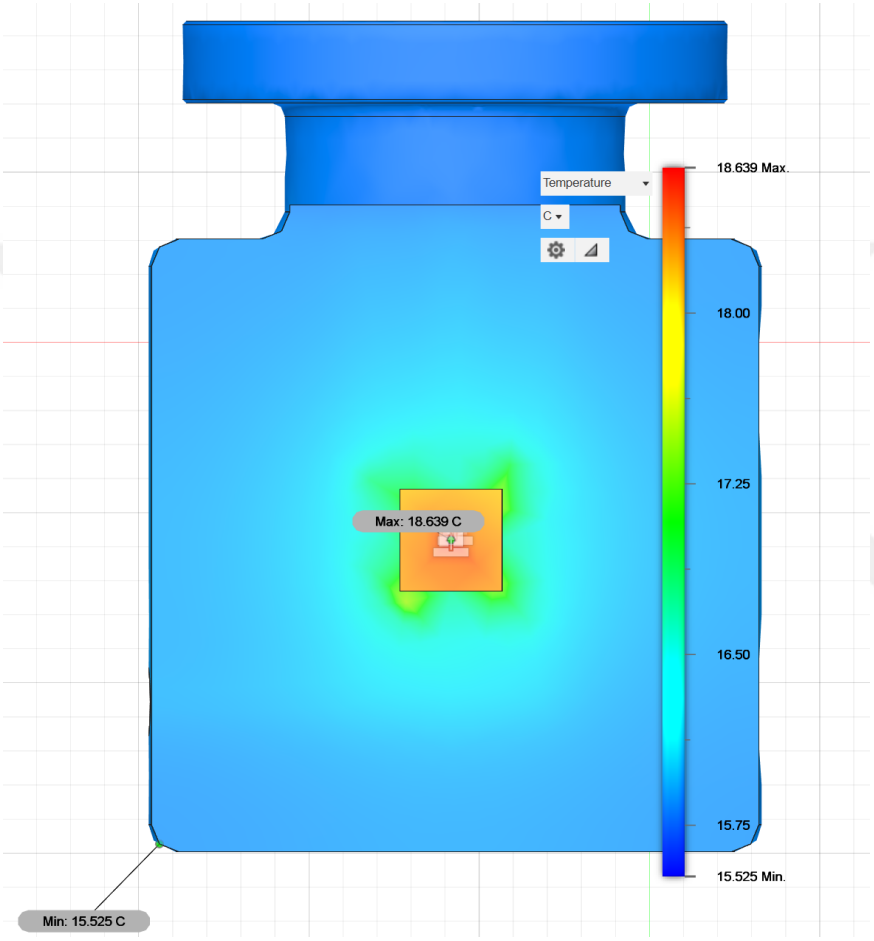


Figure A.3: $1\mu A$ proton current with 30 MeV kinetic energy.